

UNIVERSITY OF BREMEN

Department of Physics

Institute for Environmental Physics

Characterisation of a mobile MAX-DOAS system

MASTERTHESIS

to achieve the degree

Master of Science

submitted by

Lisa Marie Zeiß

born at February 13, 1990 in Frankfurt a.M.

marie.zeiss@iup.physik.uni-bremen.de

matriculation number: 2962222

at

December 01, 2015

Supervisor: Dr. Folkard Wittrock

First referee: Prof. Dr. John P. Burrows

Second referee: Dr. Anette Ladstätter-Weißmayer

Contents

1	Motivation and Outline	1
2	Atmospheric Physics and Chemistry	5
2.1	Composition and Structure of the Earth's Atmosphere	5
2.1.1	Vertical Profile	5
2.1.2	Chemical Composition	11
2.2	Tropospheric Chemistry	14
2.2.1	Nitrogen Oxides ($\text{NO}_x = \text{NO} + \text{NO}_2$)	14
2.2.2	NO_x Lifecycles in the Troposphere	14
3	Radiation in the Atmosphere	19
3.1	Optical Properties of the Earth's Atmosphere	19
3.2	The Solar Spectrum	21
3.2.1	Blackbody Radiation	21
3.2.2	The Emission Spectrum of the Sun	21
3.3	Atmospheric Interaction with Radiation	24
3.3.1	Molecular Absorption Processes	24
3.3.2	Absorption Cross Sections	26
3.3.3	Scattering Effects	27
4	Differential Optical Absorption Spectroscopy	31
4.1	Classical Absorption Spectroscopy	31
4.2	The DOAS-Method	33
4.3	Measurement Geometry	36
4.4	Concept of Air Mass Factors and Vertical Columns	39
4.5	Conversion to Volume Mixing Ratios	40
5	Instrumentation	43
5.1	Experimental Set-Up of a MAX-DOAS System	43

5.2	Telescope Unit for MAX-DOAS Measurements	46
5.2.1	Telescope Box	46
5.2.2	Pan-Tilt-Head and Set-Up	48
5.3	Spectrometers	48
5.3.1	Reflection Gratings	51
5.3.2	Further Specifications of the Spectrometer	53
5.4	Charge Coupled Device Detectors	53
5.4.1	General Function of a CCD Detector	54
5.4.2	Characteristic Data of CCD Devices	56
5.5	Software for Evaluation and Modelling	61
5.5.1	Software for Data Evaluation	61
5.5.2	SCIATRAN	62
6	Calibration of the DOAS-System	63
6.1	Characterisation of the CCD-Detectors	63
6.1.1	Dark Current Measurements	64
6.1.2	Linearity Measurements	67
6.2	Slit Function Measurements	73
7	Intercomparison of MAX-DOAS measurements of NO₂	79
7.1	General Settings and Measurement Site	79
7.2	Intercomparison of NO ₂ SCDs	84
8	Mobile MAX-DOAS Measurements of NO₂	93
8.1	Set-up and Measurement Conditions	94
8.1.1	Settings for Spectrometer's Gratings and the DOAS-Fit	96
8.2	Filtering Individual Measurements by Intensity	96
8.3	Converting Slant Columns to Vertical Columns	98
8.4	Converting Slant Columns to Volume Mixing Ratios	103
8.4.1	Estimation of the Error of NO ₂ Number Density	108
9	Summary, Conclusions and Outlook	111
10	Bibliography	115

List of Figures

2.1	Typical mid-latitude vertical temperature and pressure profile of the atmosphere	10
3.1	Photograph of moon- and sunrise by NASA astronaut Karen Nyberg	20
3.2	Spectral distribution of solar radiation	23
3.3	Possible transitions in a two atom molecule and the Franck-Condon-Principle	27
3.4	Examples of absorption cross-sections in the UV-visible range	28
3.5	Illustration of the different scattering regimes	29
4.1	Absorption spectroscopy for one absorber	32
4.2	Absorption spectroscopy in the atmosphere	33
4.3	Viewing geometry of MAX-DOAS measurements	37
5.1	Sketch of the set-up of a MAX-DOAS system. The incoming scattered sunlight is collected by a telescope unit that is mounted on a pan-tilt-head. The light is transmitted to the spectrometers operating in the UV and visible range via a y-shaped light fibre. The CCD detector converts the wavelength separated spectra into an electric signal that is transmitted to a computer with the measurement software AMAX-OMA.	45
5.2	Telescope box mounted on a pan-tilt-head	47
5.3	Optical path in the telescope	47
5.4	Set-up and optical path for the spectrometers used in the UV and the visible region.	50
5.5	Illustration of the grating equation (a) and the blaze angle (b).	52
5.6	Transmission of charge between neighbouring MOS capacitances	54
5.7	Charge transport in the shift register	55
5.8	Quantum efficiency curves	58

5.9	Back- and a Front-illuminated CCD chip unit	59
6.1	Mean counts of the dark spectrum measured for different exposure times and detector temperatures	65
6.2	Standard deviation of the mean counts of the dark spectrum measured for different exposure times and detector temperatures	66
6.3	Linearity plots for the UV detector for both available detector modes	71
6.4	Linearity plots for the visible detector for both available detector modes	72
6.5	Profile of the FWHM for 10 equal spaced vertical positions and different center wavelengths UV and visible.	74
6.6	FWHM for all available gratings in UV and visible spectrometer . . .	78
7.1	Azimuthal viewing direction of the MAX-DOAS systems on the roof of the IUP at University of Bremen	82
7.3	Comparison of raw and 30 min averaged SCDs of NO ₂ measured by the Bremen and the new instrument	84
7.4	Correlation coefficients of NO ₂ SCDs measured with the new and the Bremen MAX-DOAS system	87
7.5	Scatter plots of NO ₂ for UV and visible	91
7.6	Slopes of linear fit (without intercept) of NO ₂ SCDs scatter plots . .	92
8.1	IUP-Bremen measurement car in the field performing MAX-DOAS measurements close to highway, industrial harbour and steel plants. .	93
8.2	Azimuthal viewing direction during mobile measurements	95
8.3	NO ₂ VCD measured at 3° elevation using SCIATRAN AMFs	101
8.4	NO ₂ VCD measured at 30° elevation using SCIATRAN AMFs	102
8.5	VMR at 3° elevation using O ₄ as tracer for the effective path length .	106
8.6	VMR of NO ₂ at 30° elevation using the geometric approach	107

List of Tables

2.1	Abundance units in the atmosphere	11
2.2	Major gaseous constituents of the Earth's atmosphere	13
2.3	Total sources of NO_x in TgNyr^{-1} for the 1990s	15
4.1	Separation into narrow band and brought band structures.	35
5.1	Characteristics of the spectrometer in use for the visible (SP 2150) and the UV range (Isoplane SCT 320).	49
5.2	Characteristics of the CCD detectors	57
6.1	Detector settings and exposure times chosen for the white lamp mea- surements in UV and visible.	68
6.2	Detector settings and exposure times chosen for the line lamp mea- surements in the UV.	68
6.3	Characteristics of the spectrometer used in the UV range for different gratings	76
6.4	Characteristics of the spectrometer used in the visible range for dif- ferent gratings	76
7.1	Settings chosen for MAX-DOAS-Fits in UV and visible	81
8.1	Measurement conditions for mobile measurements	94
8.2	Settings for mobile measurements: Gratings for the UV and visible spectrometer and spectral range for the DOAS-Fit.	96
8.3	Limit for the intensity filter for mobile measurements	97
8.4	AMF for all applied elevation angles α modelled by SCIATRAN and calculated using the geometric approach	100
8.5	Mean absolute and relative deviation of VCD_{geo} to $\text{VCD}_{\text{SCIATRAN}}$. . .	100
8.6	Preliminary results for the error estimation of n_{NO_2}	109

1 Motivation and Outline

Today air pollution is the major single environmental risk to health. A recent study of the World Health Organization (2014) estimates that air pollution is responsible for about 7 million premature deaths worldwide in 2012. That makes one out of eight of total global deaths. 3.7 million premature deaths were related to ambient air pollution (AAP) (air pollution that people are exposed to outside) in both cities and rural areas. Thereof are about 280 000 deaths in high-income countries of Europe. This value corresponds to 44 deaths per 100 000 capita (worldwide its 53 deaths per 100 000 capita). This mortality is due to exposure to small particulate matter (PM) of 10 microns or less in diameter, which cause cardiovascular and respiratory disease, and cancers.

By reducing air pollution levels, countries could save millions of lives and reduce the burden of disease from stroke, heart disease, lung cancer, as well as chronic and acute respiratory diseases, including asthma (World Health Organization, 2014). A study published in 2015 by the WHO states that air pollution costs European economies US\$ 1.6 trillion a year in diseases and deaths (World Health Organization, 2015).

The 2005 'WHO Air quality guidelines' offer global guidance on thresholds and limits for key air pollutants that present risks for human health. These guidelines apply worldwide for particulate matter (PM), ozone (O_3), nitrogen dioxide (NO_2) and sulphur dioxide (SO_2). For NO_2 these limits are $40 \frac{\mu g}{m^3} \approx 21$ ppb for the annual mean and $200 \frac{\mu g}{m^3} \approx 105$ ppb for 1-hour mean.

As an air pollutant NO_2 shows several correlated activities:

- NO_2 has found to be an indicator for traffic related pollutants such as organic and elemental carbon or freshly emitted ultra-fine particles (World Health Organization, 2003).

- NO_2 is a major source of nitrate aerosols (via HNO_3) which form an important fraction of PM and are also responsible for acid rain.
- In presence of UV radiation NO_2 is a major source of tropospheric ozone and therefore acts indirectly on climate.
- NO_2 acts locally as a greenhouse gas. (Solomon and Portmann, 1999)
- In short-term concentrations $> 200 \frac{\mu\text{g}}{\text{m}^3} \approx 105\text{ppb}$ NO_2 is a toxic gas which causes significant inflammation of the airways (World Health Organization, 2003).
- Long-term exposure to NO_2 concentrations currently measured in European cities is linked to a general increase of reduced lung function and symptoms of bronchitis in asthmatic children (World Health Organization, 2003).

The major sources of anthropogenic emissions of NO_x (nitrogen oxide and nitrogen dioxide) are combustion processes. In the EU-25 in 2000 the main contributor to NO_x emissions was in the mobile sector (60%) (Schöpp et al., 2005).

In September 2015 NO_x emissions by diesel engines were intensely discussed, after it was found that the automaker Volkswagen had intentionally programmed their turbocharged direct injection (TDI) diesel engines to activate certain emissions controls for NO_x only during laboratory emissions testing. In real world driving these engines produced up to 40 times higher NO_x output (NPR, 2015).

For development and monitoring of strategies for a reduction of air pollution, climate change and other environmental problems a sound scientific understanding of fundamental physical and chemical processes that control the atmosphere as well as an accurate quantification of the relevant species are necessary. Among many spectroscopic measurement techniques that developed in the past century, differential optical absorption spectroscopy (DOAS) has proved to be a powerful method to measure a wide variety of trace gases including NO_2 .

A more recent technique of DOAS is the use of multiple viewing geometries. This multi-axis DOAS (MAX-DOAS) enables sensitive measurements of the lower troposphere by using the fact that at low viewing elevations the length of the light path in the lower troposphere is considerably elongated (Wittrock and Oetjen, 2004) (Hönninger, 2004). By using a wide range of different viewing elevations it is also

possible to derive vertical profiles.

Mobile MAX-DOAS measurements are one potential way to complement existing air quality measurements, e.g. the in-situ network *BUISSY*¹ in Bremen. They could not only provide information about NO₂ concentrations at one single spot but covering a large area and even measure height resolved profiles.

In the scope of this thesis a mobile MAX-DOAS system has been characterised for mobile measurements of NO₂ emissions in an anthropogenic polluted environment. The main objectives are:

- Set-up and calibration of a new MAX-DOAS system
- Intercomparison of the new system to the MAX-DOAS system operating continuously on the roof of the IUP Bremen
- Installation of the new MAX-DOAS system into the measurement car of the IUP Bremen
- Evaluation of mobile MAX-DOAS measurements around Bremen using two off-axis elevations (3°, 30°) including:
 - Development of a routine to filter out individual spectra that were affected by objects in the light path
 - Intercomparison of different methods to estimate the air mass factor for calculation of the vertical column density of NO₂
 - Application of two different methods to derive the volume mixing ratio of NO₂ using MAX-DOAS measurements at 3° and at 30° elevation

Outline of this thesis

The relevant aspects of atmospheric chemistry and physics are introduced in chapter 2. The physical fundamentals of interaction of light with the atmosphere are given in chapter 3. In chapter 4 the DOAS method is introduced. The set-up of the MAX-DOAS system including a detailed description of its single compounds and the necessary software is given in chapter 5. The results of the calibration of the new

¹Bremer Umweltinformationssystem (<http://www.bauumwelt.bremen.de>)

MAX-DOAS system are presented in chapter 6. The intercomparison study with the MAX-DOAS instrument continuously measuring on the roof of the IUP Bremen can be found in chapter 7. Chapter 8 presents the results of the mobile NO₂ retrieval around Bremen. Finally, with chapter 9 this thesis closes with a brief summary of the main results, the conclusions and recommendations for future work.

2 Atmospheric Physics and Chemistry

The following chapter shall give a brief survey of the structure and the chemical composition of the Earth's atmosphere. The tropospheric chemistry related to nitrogen oxides will be described. Chapter 3 will present the optical properties of the atmosphere and the physical processes relevant for the interaction with light.

2.1 Composition and Structure of the Earth's Atmosphere

The atmosphere is the gaseous layer that separates the Earth's surface from space. Compared to the Earth's equatorial radius of approximately 6380 km the atmosphere is a very thin layer (approximately 100 km) that is attracted by the Earth's gravitational field.

2.1.1 Vertical Profile

For the vertical structure of the atmosphere several classifications can be made. The most common is a classification by the vertical temperature profile, which divides the atmosphere into four layers. Figure 2.1 shows a typical mid-latitude temperature profile as represented by the U.S. Standard atmosphere. The boundaries between these four layers (troposphere, stratosphere, mesosphere and thermosphere) are denoted by the suffix pause.

The pressure p decreases nearly exponentially with altitude z following the barometric equation:

$$p(z) \approx p_0 \cdot \exp\left(-\frac{z}{H}\right) \quad (2.1)$$

p_0 is the pressure at a reference level, usually at sea level $z = 0$. H is the height where the pressure decreased by a factor of $1/e$. It is referred to as scale height and given by $H = \frac{RT}{mg}$. In the lowest 100 km of the atmosphere the scale height reaches roughly from 7 to 8 km (Wallace and Hobbs, 2006). The pressure scale in figure 2.1 is plotted logarithmic.

To understand the temperature profile and the formation of the different layers several thermodynamic considerations are necessary. They shall be described briefly in the following.

Adiabatic processes and dry adiabatic lapse rate

The first law of thermodynamics states that the change of inner energy dU of a system results from applying mechanical work δW and heat δQ :

$$dU = \delta W + \delta Q \quad (2.2)$$

In an adiabatic process no heat is exchanged ($\delta Q = 0$). The applied work is resulting from a compression of volume: $\delta W = -pdV$. Using in addition the definition of the specific heat capacity at constant volume $C_V = \left(\frac{dU}{dT}\right)_V$ one obtains:

$$dU = -pdV = C_V dT \quad (2.3)$$

With the derivative with respect to z of the barometric equation 2.1, the total differential of the ideal gas law and the definition of the gas constant $R = C_p - C_V$ yields a formula for the dry adiabatic temperature gradient, also referred to as dry adiabatic lapse rate:

$$\Gamma = \frac{dT}{dz} = \frac{M \cdot g}{C_p} \quad (2.4)$$

where M is the molar mass and C_p the specific heat capacity at constant pressure. In the presence of water vapour the change of heat can no longer be neglected: $\delta Q \neq 0$. The resulting lapse rate is called pseudo adiabatic lapse rate and is always smaller than the dry adiabatic lapse rate.

Potential Temperature

Based on Poisson's equation for adiabatic processes $\frac{T^\kappa}{p^{\kappa-1}} = \text{const}$ one can define the potential temperature Θ which is the temperature an air parcel with pressure p would have if it was dry adiabatically brought to ground pressure level p_0 . Hence the potential temperature is given by

$$\Theta = T \left(\frac{p_0}{p} \right)^{\frac{\kappa-1}{\kappa}} \quad (2.5)$$

where $\kappa = \frac{C_p}{C_v}$.

Static stability

Using the potential temperature one can distinguish between three stability cases when an air parcel is slightly moved from its equilibrium position:

- stable: $\frac{\partial\Theta}{\partial z} > 0$

The actual lapse rate γ is smaller than the dry adiabatic lapse rate Γ . An air parcel that is brought out of its equilibrium due to an upwards motion will be cooled down faster than the surrounding air leading to a downwards motion. Finally the air parcel will settle down to its stable position. In the atmosphere this situation is the case when warm air lays about colder air and therefore vertical exchange is inhibited. This situation is also referred to as inversion.

- unstable: $\frac{\partial\Theta}{\partial z} < 0$

$\gamma > \Gamma$: An air parcel that is moved upwards will be cooled down slower than the surrounding air and the air parcel will continue its upward motion.

- neutral: $\frac{\partial\Theta}{\partial z} = 0$

$\gamma = \Gamma$: An air parcel that is moved out of its equilibrium position will change its temperature equal to its surrounding. No buoyancy forces will happen.

Considering the adiabatic processes explained above the formation of the layers in the atmosphere can be explained:

Troposphere

- The troposphere is the lowest layer of the atmosphere, extending from the Earth's surface up to the tropopause.
- The height of the tropopause depends on latitude and season and varies between 18 km in the tropics, up to 12 km in the mid-latitudes and 6-8 km at the poles (Wallace and Hobbs, 2006).
- It contains about 80% of the atmosphere's mass and almost all water vapour and aerosols (Wallace and Hobbs, 2006).
- The generally decreasing temperatures with height allow warmer air parcels to rise leading to subsequent convection processes. Therefore the troposphere is a vertically well mixed layer.

- Vertical transport happens with an average lapse rate of $\Gamma = \frac{\partial T}{\partial z} \approx 6.5 \text{ K km}^{-1}$ which is smaller than the dry adiabatic lapse rate which is 9.8 K km^{-1} (Wallace and Hobbs, 2006).
- Under certain conditions in the troposphere thin layers with a positive temperature gradient can be found. Within those temperature inversions vertical mixing is strongly inhibited.
- Almost all weather phenomena take place in the troposphere.

Boundary layer

- The lowest part of the troposphere is called boundary layer (BL).
- The BL is the part of the atmosphere where interactions with the surface become relevant.
- The extend of the BL depends on daytime and meteorological conditions. A typical value is about 1 km.

Stratosphere

- Here the temperature increases with height, due to the ozone layer which absorbs solar UV radiation and subsequently warms up.
- The peak of the ozone volume mixing ratio is at an altitude of $\approx 25\text{-}30 \text{ km}$.
- This positive temperature gradient allows no convection. The tropopause acts as a barrier for tropospheric rising air parcels.
- The exchange between troposphere and stratosphere is limited to convection in the tropics, folded structures of the tropopause near upper-level frontal zones (tropopause folds) and down-welling in the polar regions.

Mesosphere

- At the stratopause the heating due to ozone UV absorption decreases and in the adjacent mesosphere the temperature gradient turns negative again.
- The mesosphere ends with the mesopause at a height of approximately 80 km, where the temperature gradient again reverses.

Thermosphere

- The thermosphere is strongly influenced by charged particles emitted from the sun (solar winds).
- Very high energetic solar radiation ionizes molecular and atomic nitrogen and oxygen leading to a plasma with very fast particles.
- This high kinetic energy of the particles is responsible for the strong increase of temperature (> 1000 K).
- Due to the low density and the resulting long free path length in order of several kilometres collisions are much to rare for heat exchange. Therefore a thermometer would measure temperatures close to the absolute zero point.

Exosphere

- The topmost layer of the atmosphere is the exosphere at > 500 km altitude.
- Here gas molecules with sufficient energy can escape from the Earth's gravitational attraction.

(Seinfeld and Pandis, 2012)

The transition between exosphere and space is continuous. Two common definitions for the boundary between atmosphere and space are the Kármán line at 100 km and the NASA's definition of the borderline with the height of the mesopause at 80 km.

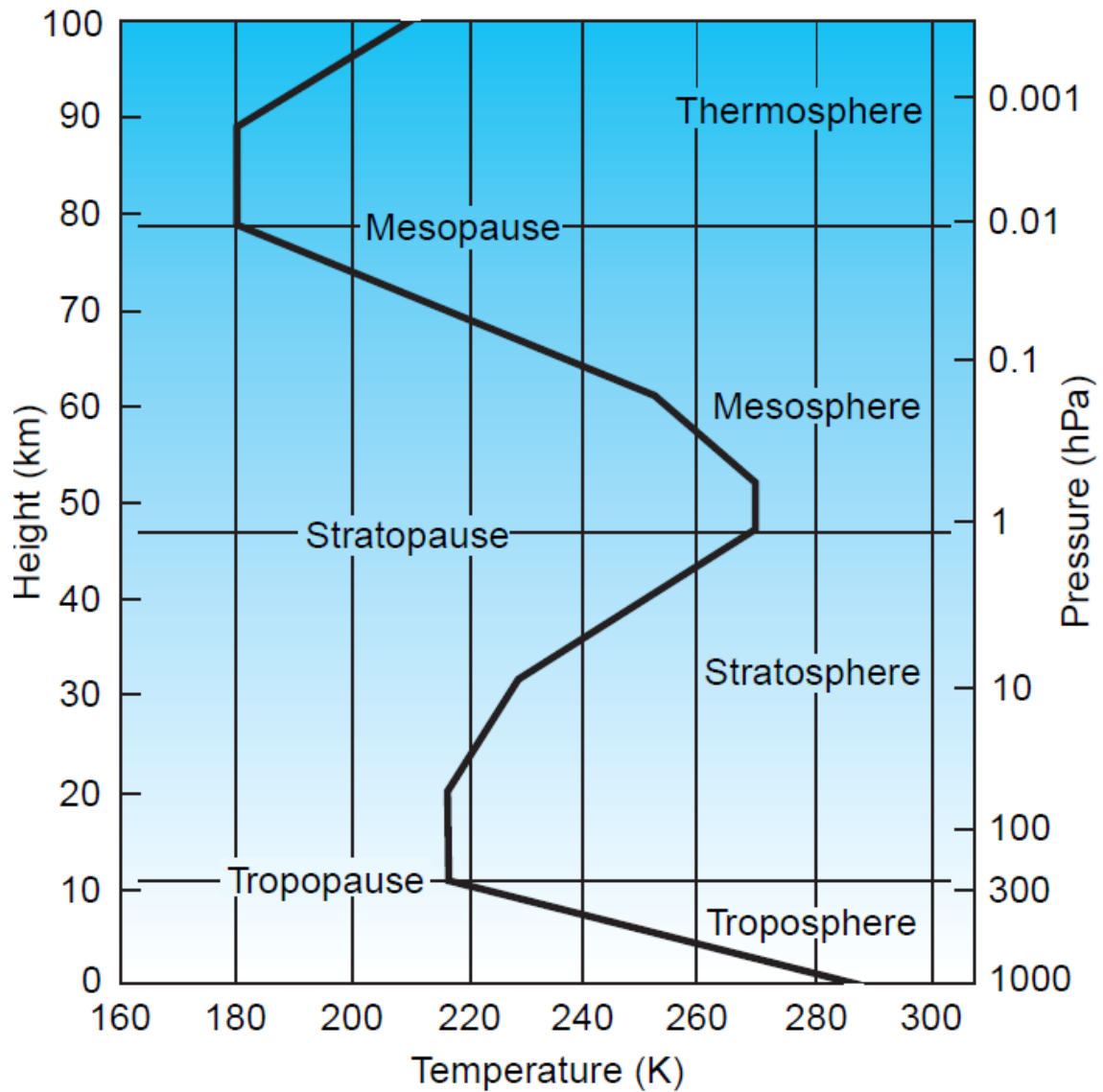


Figure 2.1: Typical mid-latitude vertical temperature and pressure profile of the atmosphere as represented by the U.S. Standard atmosphere (figure by Wallace and Hobbs (2006)). The vertical temperature profile divides the Earth's atmosphere into four different layers with alternating positive and negative temperature gradients: Troposphere, Stratosphere, Mesosphere, Thermosphere. The boundaries between these layers are denoted with the suffix -pause.

2.1.2 Chemical Composition

The atmosphere is composed of a mixture of gases. To express the amount of a certain species in the atmosphere several quantities can be used. They are presented in table 2.1. The *mixing ratio* of a gas is defined as the number of moles of a gas per mole of air. Since the volume occupied by an ideal gas is proportional to the number of molecules this is equivalent to the *volume mixing ratio* (VMR) that is the volume of a gas per volume of air. Within the atmosphere pressures are sufficiently low that the ideal gas law is always obeyed within 1%. Using the VMR as a abundance unit has the advantage that it remains constant although the air density changes (e.g. by a change of pressure or temperature). This makes it a robust measure of the atmospheric composition. (Jacob, 1999) The volume mixing ratios of the main

quantity	symbol	Units
number of molecules	N	mol=6.022·10 ²³
number density	n	particles/m ³
mass density	ρ	kg/m ³
volume mixing ration	VMR	dimensionless ($\frac{n_{species}}{n_{air}}$) ppmV=10 ⁻⁶ ppbV=10 ⁻⁹ pptV=10 ⁻¹²
mass mixing ratio	MMR	dimensionless ($\frac{\rho_{species}}{\rho_{air}}$) ppmm=10 ⁻⁶ ppbm=10 ⁻⁹ pptm=10 ⁻¹²
column abundance		molec/cm ²

Table 2.1: Abundance units in the atmosphere

constituents in the atmosphere are listed in table 2.2. The main constituents are thus diatomic nitrogen (N₂) 78.08% and oxygen (O₂) 20.95% followed by the noble gas argon (Ar) with 0.93%. Water vapour accounts for approximately 0.25% of the mass of the atmosphere. Its volume mixing ratios are highly variable. VMRs can

change between around 10ppmV in the coldest regions of the Earth's atmosphere up to 5% by volume in hot, humid air masses. Therefore it is common to list volume mixing ratios in relation to dry air, excluding water vapour (Wallace and Hobbs, 2006). The inert gases N_2 , argon and the other noble gases are very stable. Hence their concentration in the atmosphere remains constant. Most chemical reactions in the atmosphere involve O_2 but most of the time they are not spontaneous since they require high activation energies like they are for example given in combustion processes. N_2 , O_2 and the noble gases are permanent constituents of the atmosphere with nearly constant spacial and temporal distribution. Beside these permanent constituents and the highly fluctuating water vapour the atmosphere includes a multitude of *trace gases*. These trace gases show more or less fluctuations in concentration, are in general not homogeneously distributed in the atmosphere and show lifetimes in the order of minutes to years. Although trace gases only show in low concentrations they can be of critical importance for climate warming, the ozone layer, smog and other environmental issues. Those trace gases that influence the radiative budget of the atmosphere and hence play a crucial role in our climate system are called *greenhouse gases* and are indicated by bold-faced type in table 2.2.

The variability of trace gases and water vapour are the result of the dynamic system of the atmosphere: The continuous exchange of gases and aerosols with vegetation, oceans and biological organisms. The atmospheric cycles of atmospheric gases involve a number of physical and chemical processes. This thesis concentrates on the retrieval of NO_2 in an urban region. Therefore the cycles of tropospheric $NO_x=NO_2+NO$ shall be discussed in the following section (2.2).

Species	VMR
Nitrogen (N ₂)	78.08%
Oxygen (O ₂)	20.95%
Argon (A)	0.93%
Water vapor (H₂O)	0-5%
Carbon dioxide (CO₂)	380 ppm
Neon (Ne)	18 ppm
Helium (He)	5 ppm
Methane (CH₄)	1.75 ppm
Krypton (Kr)	1 ppm
Hydrogen (H ₂)	0.5 ppm
Nitrous Oxide (N₂O)	0.3 ppm
Ozone (O₃)	0-0.1 ppm
Nitrogen Oxides (NO _x =NO+NO ₂) ^(a)	0.03-5 ppb

Table 2.2: Fractional concentrations by volume of the major gaseous constituents of the Earth's atmosphere up to an altitude of 105 km, with respect to dry air. *Greenhouse gases* are indicated by bold-faced type (Wallace and Hobbs, 2006). ^(a) The VMR for nitrogen oxides NO_x=NO+NO₂ is taken from Platt and Stutz (2008).

2.2 Tropospheric Chemistry

The focus of this thesis lies on the retrieval of tropospheric nitrogen in an anthropogenically polluted environment. Therefore this section will concentrate on the trace gas NO_2 and the associated processes that lead to air pollution in urban environments.

2.2.1 Nitrogen Oxides ($\text{NO}_x = \text{NO} + \text{NO}_2$)

The oxides of nitrogen, NO and NO_2 are among the most important molecules in atmospheric chemistry. NO_x is produced in a large number of natural and anthropogenic processes. Of particular importance are those processes where air is heated to high temperatures. This is for example the case in combustion processes, forest fires or lightning strikes. Table 2.3 gives an overview of the estimated global NO_x emissions given by the IPCC Assessment Reports 3 (2001) and 4 (2007). The yearly average NO_2 concentration in 2014 for measurement stations in Bremen was between $17\text{--}44 \frac{\mu\text{g}}{\text{m}^3}$ (9–23 ppb) (Umweltbundesamt, 2015).

2.2.2 NO_x Lifecycles in the Troposphere

Tropospheric NO_x radicals are key species determining the concentration of tropospheric ozone. The high temperatures in combustion processes or lightning allow reactions of the most abundant atmospheric trace gases N_2 and O_2 producing nitrogen monoxide (NO):



This NO reacts subsequently with ozone and forms nitrogen dioxide (NO_2):



During daytime photolysis of NO_2 returns NO and an (excited) oxygen atom:



The oxygen atom reacts with O_2 and forms ozone:



Source	TAR	AR4
Anthropogenic sources		
Fossil fuel combustion and industrial processes	33	25.6
Biomass burning (and biofuels)	7.1	5.9
Agriculture	2.3	1.6
Aircraft	0.7	included in anthropogenic total
Anthropogenic total	43.1	33.4
Natural sources		
Soils under natural vegetation	3.3	7.3
Lightning	5	1.1 - 6.4
Atmospheric Chemistry	<0.5	-
Natural total	8.8	8.4 - 13.7
Total sources	51.9	41.8 - 47.1

Table 2.3: Total sources of NO_x in TgNyr^{-1} for the 1990s estimated by the IPCC Assessment Reports 3 in 2001 (TAR) and 4 in 2007 (AR4) (IPCC: Working Group I, 2007).

Reaction 2.7 is a three-body-collision reaction meaning that an additional component M (usually N₂ or O₂) is absorbing the excess energy.

(Seinfeld and Pandis, 2012)

The reactions described above would lead to an equilibrium between ozone, NO and NO₂ depending on the sunlight when all other species would be neglected. They dominate the NO_x cycle during daytime.

In urban areas anthropogenic emissions predominantly release NO that destroys ozone following reaction 2.7 leading to lower ozone concentrations in polluted areas. Nevertheless large amounts of NO_x emitted by cars, heating and industry can lead to formation of ozone. This is the case in the presence of perhydroxyl radical (HO₂) that is formed in the troposphere by the oxidation of hydrocarbons. The most important atmospheric reaction that the HO₂ radical undergoes is with NO (Seinfeld and Pandis, 2012):



Because NO is converted into NO₂ without destroying ozone and photolysis of NO₂ produces NO and ozone, the ozone concentration will increase. This phenomenon is called *summer smog*. It can be found in summertime in urban areas with high traffic volume. The resulting high concentrations of NO_x and the increased photolysis of NO₂ due to higher light intensities in summertime lead to high ozone concentrations.

The reaction, that mainly removes OH and NO₂ from the system is the formation of nitric acid (HNO₃):



This reaction depends indirectly on sunlight because OH is predominantly formed by H₂O and O resulting from the photolysis of ozone. Therefore the NO₂ concentration reaches its minimum at noon time, when the OH concentration is highest. Nitric acid is readily soluble and is subsequently removed from the atmosphere by aerosols and wet deposition.

During night time the photolysis of NO₂ stops and NO and O₃ levels decline be-

cause of reaction 2.7 (in the absence of new emissions). NO_2 and O_3 react to nitrate (NO_3):



During daytime the NO_2 stored in the reaction above is recovered when NO_3 reacts with NO :



Nitrate can also be removed from the system when it reacts with NO_2 to dinitrogen pentoxide N_2O_5 .

(Seinfeld and Pandis, 2012)

3 Radiation in the Atmosphere

3.1 Optical Properties of the Earth's Atmosphere

The atmosphere is relatively transparent to incoming solar radiation and opaque to radiation emitted by the Earth's surface. This blocking of the outgoing radiation is called *greenhouse effect* and keeps the Earth's surface warmer than it would be without any atmosphere. Most of the absorption and re-emission of outgoing radiation are due to air molecules, but cloud droplets and aerosols also play an important role (Wallace and Hobbs, 2006).

Figure 3.1 shows a photograph of moon- and sunrise over the Earth's limb from the International Space Station (ISS). Due to scattering effects, the different layers of the atmosphere can be recognized very well. The white layer is mainly light that was scattered in the troposphere by atmospheric aerosols and cloud droplets (Mie scattering). The blue layer above is mainly light scattered by air molecules predominantly N_2 and O_2 (Rayleigh scattering). The physical background of these scattering effects will be explained in section 3.3.3. At this point only be advised that Rayleigh scattering is proportional to the wavelength with λ^{-4} . Therefore the light scattered by air molecules is blue, while the direct sunlight is the part of the solar spectrum that was not scattered, the longer wavelengths in the visible spectrum: yellow, orange and red.



Figure 3.1: Photograph of moon- and sunrise by NASA astronaut Karen Nyberg over Earth's limb on August 4, 2013 from International Space Station. [<http://Earthobservatory.nasa.gov/blogs/Earthmatters/2013/08/05/sun-moon-and-two-planets-rising-over-Earths-limb/>] The white layer is mainly light scattered from atmospheric aerosols and cloud droplets. The overlaying blue layer is mainly light scattered by air molecules (N_2 , O_2). The orange-red light is the part of the solar spectrum that was not scattered.

3.2 The Solar Spectrum

The Sun is a nearly perfect spherical ball of incandescent plasma. It has a radius of approximately $6.96 \cdot 10^5$ km and a mass of approximately $1.99 \cdot 10^{30}$ kg. It basically consists of three parts hydrogen and one part helium. Energy is produced in the core by nuclear fusion of four hydrogen atoms into one helium atom. The energy is transported from the core to the outer 500 km of the Sun, the *photosphere*. From there most energy received by the Earth is emitted. The emission spectrum of the Sun is close to that of a blackbody with a temperature of 5777°K . The maximum of the solar radiation is in the visible at a wavelength of $\lambda \approx 500$ nm. (Seinfeld and Pandis, 2012)

3.2.1 Blackbody Radiation

The monochromatic emissive power $F_B(\lambda, T)$ [$\text{W m}^{-2} \text{m}^{-1}$] of a blackbody in dependence of wavelength λ and temperature T is given by Planck's law:

$$F_B(\lambda, T) = \frac{2\pi hc^2 \lambda^{-5}}{\exp(ch/k_B T \lambda) - 1} \quad (3.1)$$

where k_B is the Boltzmann constant. Differentiating equation 3.1 with respect to λ , setting the result equal to zero and solving for λ delivers the wavelength for the maximum peak of the blackbody spectrum in dependence of temperature T :

$$\lambda_{max} = \frac{2.897 \cdot 10^6}{T} \quad (3.2)$$

This equation is also referred to as Wien's displacement law. Integrating equation 3.1 over all wavelengths delivers the total emissive power P [W m^{-2}] of a blackbody:

$$P = \int_0^\infty F_B(\lambda) d\lambda = \sigma T^4 \quad (3.3)$$

This equation is referred to as Stefan-Boltzmann's law. $\sigma = 5.671 \cdot 10^{-8}$ [$\text{W m}^{-2} \text{K}^{-4}$] is the Stefan-Boltzmann constant (Seinfeld and Pandis, 2012).

3.2.2 The Emission Spectrum of the Sun

Figure 3.2 shows the solar spectrum before it enters the Earth's atmosphere (yellow) and the spectral distribution of solar radiation at the Earth's surface at sea level (red). The solar spectrum is close to that of a blackbody (black line). The absorption

lines in the solar spectrum without absorptions in the Earth's atmosphere, are called *Fraunhofer lines*. They can be traced back to absorptions in the Sun's photosphere. The major Fraunhofer lines come from absorptions by the following elements O₂, Na, H, He, Hg, Fe, Mg, Ca and Ni.

In the Earth's atmosphere the major absorption bands belong to H₂O, CO₂ and O₂ in the infra red and O₃ in the UV.

The lines in an emission spectrum are never exactly monochromatic but show a finite width. This broadening effects result from three different processes:

- **Natural line width:** Following Heisenberg's uncertainty principle for energy and time :

$$\Delta E \cdot \Delta t \geq \frac{h}{4\pi} \quad (3.4)$$

with increasing Δt the energy uncertainty decreases. Therefore the broadening of the absorption/emission line will increase with decreasing life time of the excited states. The resulting broadened line has a Lorentzian shape.

- **Pressure broadening:** Collusions between the emitting/absorbing gas particles can lead to interruptions in the emission/absorption process and therefore increasing the energy uncertainty of the process. The resulting line broadening has a Lorentzian shape and depends on the temperature and the density of the emitting gas.
- **Doppler broadening:** The emitting/absorbing gas particles will move following the thermal velocity distribution in the gas. The resulting wavelength shift can be positive or negative depending on the movement of the particle towards the observer. Doppler broadening depends on temperature and inertia of the emitting/absorbing gas particles. The broadened line shows a Gaussian shape.

Of these three broadening mechanisms the natural line width, i.e. natural lifetime of the excited state, leads to very small broadening in the order of 0.01 pm, while the effect of pressure broadening and Doppler broadening are roughly equal in the order of typically 1 pm in the UV-visible spectral region (Platt and Stutz, 2008).

Spectrum of Solar Radiation (Earth)

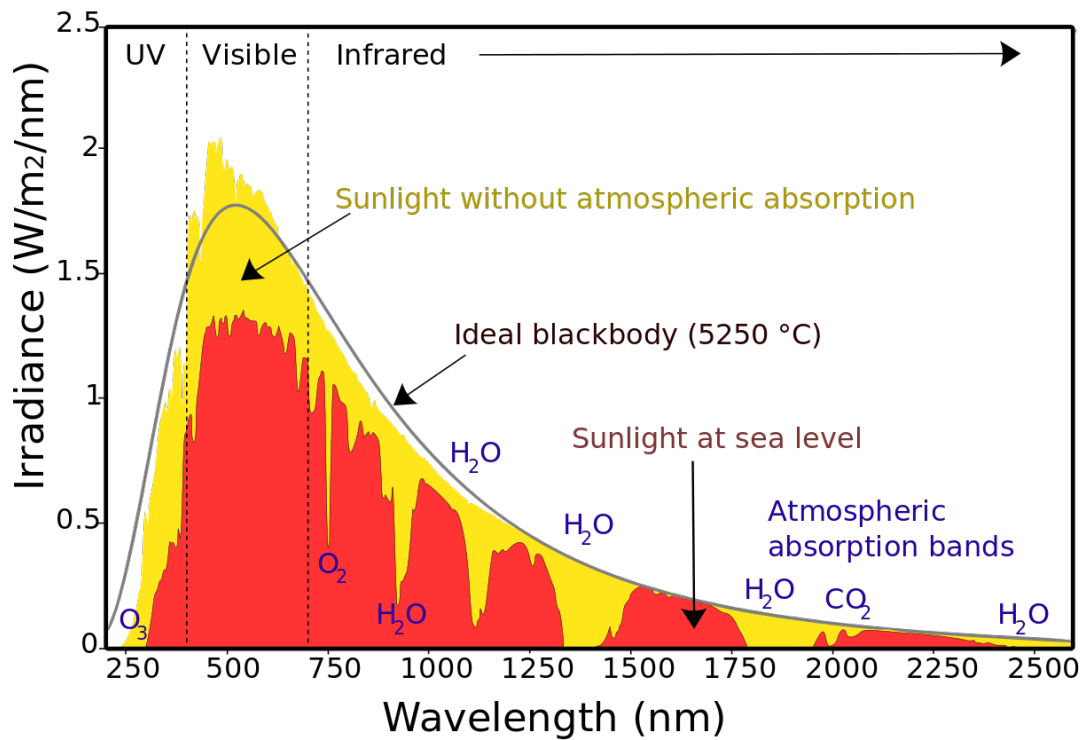


Figure 3.2: Spectral distribution of solar radiation without atmospheric absorption (yellow) and at the Earth's surface at sea level (red). The solar spectrum is close to that of a blackbody with a temperature of 5250°C (black line). The most important atmospheric absorption bands of H₂O, CO₂ and O₂ in the infrared and O₃ in the UV are marked in blue.

[http://commons.wikimedia.org/wiki/File:Solar_spectrum_ita.svg]

3.3 Atmospheric Interaction with Radiation

When sunlight enters the Earth's atmosphere three different physical processes are relevant for the interaction with the surrounding atmosphere: Absorption, scattering and geometric optics. In the following those processes shall be described briefly.

3.3.1 Molecular Absorption Processes

Beside aerosols and water droplets the Earth's atmosphere mainly consists of molecules. When a molecule absorbs or emits a photon with energy $h\nu$ it changes its inner energy. Hence a transition between energy level E_1 to E_2 takes place. Following the law of conservation of energy the difference between these energy levels is equivalent to the photons energy:

$$h\nu = E_1 - E_2 \quad (3.5)$$

If these energy levels are discrete bounded states they have a relatively sharp defined energy so that the transition will take place at the corresponding frequency ν . In the spectrum this results in a sharp absorption or emission line at wavelength $\lambda = \frac{c}{\nu}$. For transitions that include unstable states which lead to a possible dissociation of the molecule and for transitions that include energy states above the ionisation border a continuum is observed.

Molecular spectra are much more complex than the ones of atoms. For atoms the possible energy transitions are basically defined by the structure of the atomic shell and every line in the spectrum corresponds to one electronic transition. Molecules have much more energy levels that no longer only depend on the atomic shell but also on the geometric arrangement of the atomic nuclei and their movement with respect to each other. This results in three different types of energy levels:

- The whole molecule can rotate around its centre of mass: **rotational energy levels**
- The atomic nuclei in a molecule can vibrate: **vibrational energy levels**
- The molecule can change its electronic state: **electronic energy levels**

Hence a molecule can change its rotational energy, its vibrational energy and its electronic energy:

$$E_{molecule} = E_{rot} + E_{vib} + E_{el} \quad (3.6)$$

where $E_{rot} \ll E_{vib} \ll E_{el}$.

Figure 3.3 shows the possible energy transitions for a two-atomic molecule in a schematic diagram. The spectra resulting from these energy transitions of a molecule can be separated into the following categories:

- Rotational spectra:** Transitions between adjacent rotational energy levels in the same vibrational and electronic energy level lead to rotational spectra in the microwave spectral range ($\lambda \approx 1 \text{ mm} - 1 \text{ m}$). These transitions can only take place, when the electronic state of the molecule shows a permanent dipole moment. Rotational spectra consist of very closely spaced, nearly equidistant lines with a characteristic intensity distribution.
- Vibrational-rotational spectra:** Transitions between rotational energy levels in different vibrational levels lead to vibrational-rotational spectra. Vibrational transitions can happen between different vibrational levels of one electronic state. In vibrational transitions the molecule undergoes a change of its dipole strength or direction due to a vibration of the atomic nuclei. Using the Born-Oppenheimer approximation (movement of nuclei small in comparison to movement of the electrons so that both movements can be separated) vibrational energies and wave functions can be calculated by calculating the electronic energy $E_{el}(\mathbf{R})$ as a function of all nuclear coordinates \mathbf{R} . $E_{el}(\mathbf{R})$ can therefore be interpreted as a potential for the movement of the nuclei. Because vibrational and rotational transitions are coupled no pure vibrational spectra exist. Vibrational-rotational spectra show a strong line at frequency ν and several overtones at $2\nu, 3\nu$, etcetera. With a sufficiently high resolution one can recognise that each of these lines are band structures that show very close, nearly equidistant rotational lines. These vibrational-rotational spectra are found in the middle infra-red ($\lambda \approx 2\mu\text{m} - 20\mu\text{m}$).
- Electronic spectra:** Transitions between two electronic energy levels appear in the spectral range from UV to near intra-red ($\lambda \approx 0.1\mu\text{m} - 2\mu\text{m}$). The excitation of an electron goes along with simultaneous rotational-vibrational

transitions. Therefore electronic spectra can show a huge number of lines that correspond to the resulting vibrational and rotational transitions. The vibrational-rotational structures can only be distinguished using very high resolution. Because of the resulting band structures electronic spectra are referred to as band-spectra. The intensity distribution of electronic transitions can be explained by the **Franck-Condon principle**. Following the Paul-Oppenheimer approximation in general the nuclear coordinates will not change in electronic transitions. The Franck-Condon principle states that electronic transitions happen most probable between vibrational states that show an amplitude in their vibrational wave functions. In figure 3.3 this is illustrated. An electronic transition from electronic ground state E_1^{el} to the excited state E_2^{el} is most probable between the vibrational levels $\nu'' = 0$ and $\nu' = 2$ for absorptions. For the fluorescence case a transition from $\nu' = 0$ to $\nu'' = 2$ is preferred (Demtröder, 2013)(Haken and Wolf, 2013).

3.3.2 Absorption Cross Sections

As outlined above absorption spectra in the UV and visible show rotational and vibrational structures. Frequently, the rotational structure consists of so many lines with a spacing smaller than their line-width or so small that they can not be resolved by the spectrometer in use. This leads to a quasi-continuous absorption within a vibrational band. The absorption cross section is a characteristic of any species. It is a measure for the probability of an absorption process in dependence of the wavelength λ of the incident light and the temperature. The unit is [cm^2/molec]. Figure 3.4 shows the cross-section spectra of some species.

Oxygen Collision Complex (O_2)₂

The oxygen collision complex (O_2)₂, also written as O_4 is a O_2 - O_2 van der Waals complex of two oxygen molecules (Camy-Peyret and Vigasin, 2003). The nature of the molecular interactions in the O_2O_2 collisional complex is still debated. In contrast to an isolated oxygen molecule it shows several prominent absorption bands in the UV and visible parts of the spectrum (e.g. $\lambda \approx 343, 360, 380, 477, 532, 577, 630$ nm (Wagner and Friedeburg, 2002)). Therefore the oxygen collision complex has to be considered in the trace gas retrieval (Spinei et al., 2015).

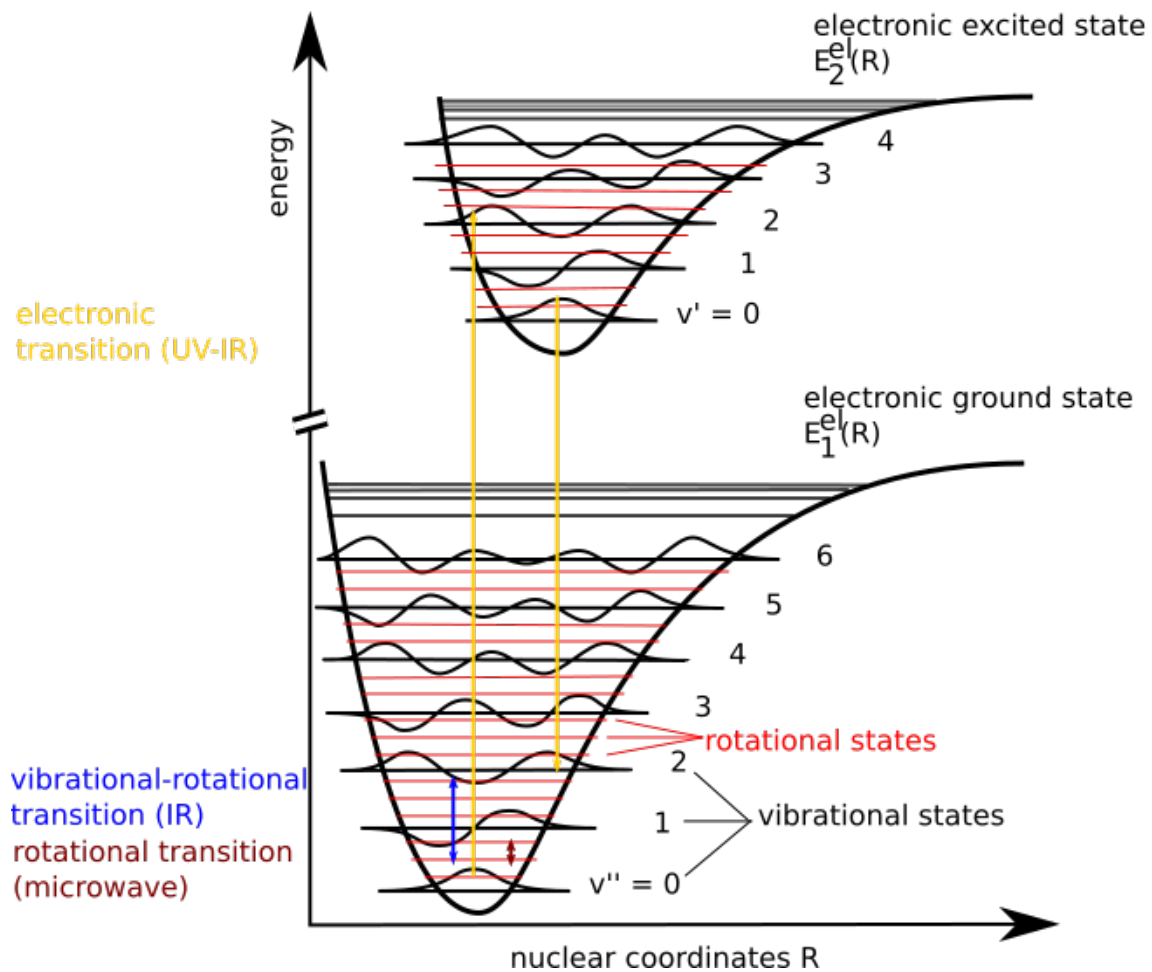


Figure 3.3: Schematic diagram of possible transitions in a two atom molecule and the related spectral regions. Electronic transitions follow the Franck-Condon-Principle.

3.3.3 Scattering Effects

Incoming photons are scattered on air molecules and particles like aerosols and water droplets in the atmosphere. Depending on size and form of the scattering particles and wavelength of the incident light λ different types of scattering are prominent. A classification can be done by defining the dimensionless size parameter x as function of λ and particle radius r of a assumed spherical particle:

$$x = \frac{2\pi r}{\lambda} \quad (3.7)$$

Figure 3.5 shows an overview of the different scattering regimes:

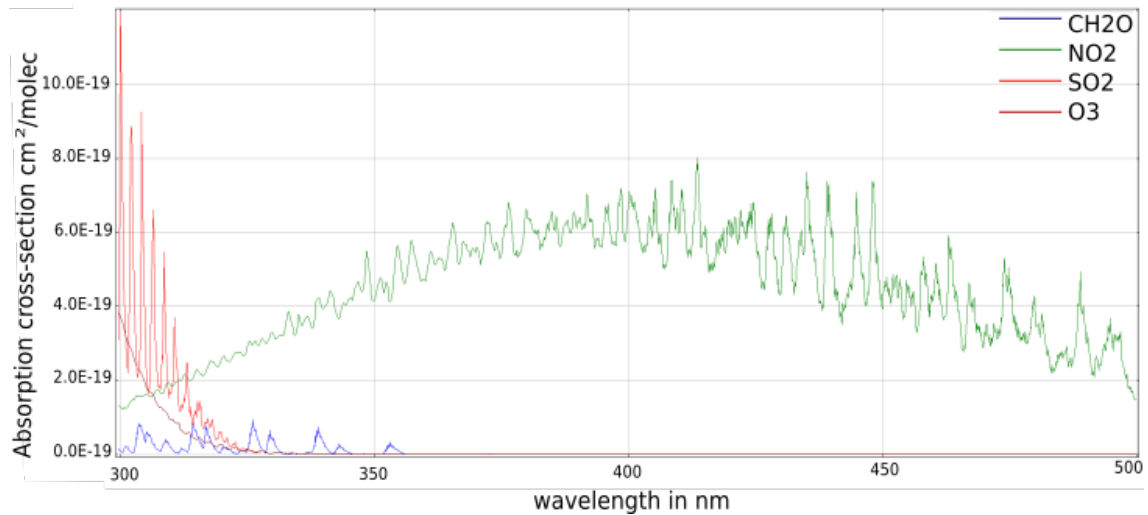


Figure 3.4: Examples of absorption cross-sections in the UV-visible range: formaldehyde (CH_2O) at 297 K (Meller and Moortgat, 2000), nitrogen dioxide (NO_2) at 298 K (Vandaele and Hermans, 1996), sulphur dioxide (SO_2) at 293 K (Bogumil et al., 2003) and tropospheric ozone (O_3) at 243 K (Gorshelev et al., 2014). NO_2 shows absorption bands over a wide range of wavelengths in the visible and UV spectrum. O_3 , CH_2O and SO_2 only absorb in the UV. The absorption cross-sections of the different species show differences in their band-width. For example SO_2 shows very narrow-band absorption structures.

- $x \ll 1$: **Rayleigh scattering** on air molecules with an efficiency $\propto \lambda^{-4}$. Un-polarized incoming light is mainly scattered in back and front direction. The polarization of the scattered light depends on the scattering direction. The scattered light is un-polarized in back and front direction and maximally polarized in the directions orthogonal to the incident light.
- $x \approx 1$: **Mie scattering** on spherical objects like cloud droplets and aerosols cannot be described analytically. Depending on the geometry the scattering efficiency is proportional to the wavelength of the incoming light by $\propto \lambda^{-a}$ with the Angstrom exponent $-1 < a < 4$ (typically between 0.5 and 2.5). The scattered light is non-polarized. While Rayleigh scattering shows no preferred scattering direction, Mie scattering shows a preference of scattering in the front direction.
- $x \gg 1$: **Geometric optics** on large particles like raindrops or ice particles.

(Wallace and Hobbs, 2006) This interaction can be elastic when the incoming light

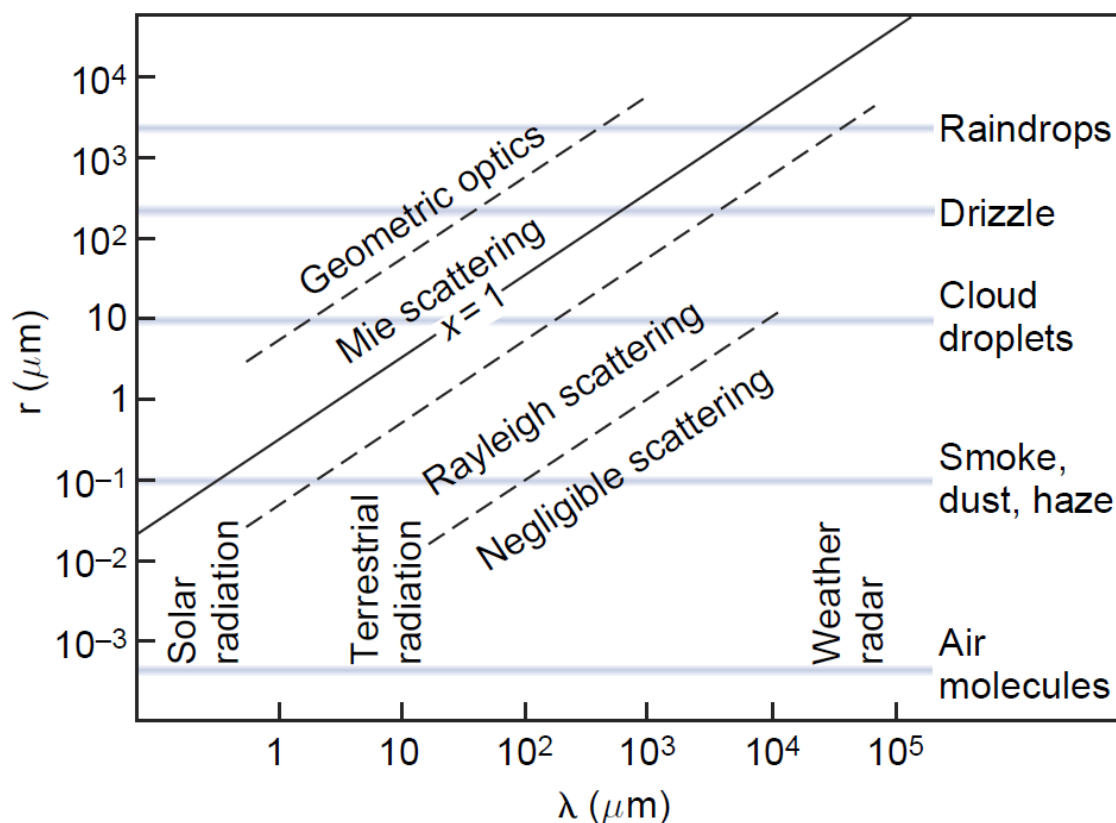


Figure 3.5: Illustration of the different scattering regimes depending on particle size. Size parameter x as a function of wavelength λ of the incident radiation and particle radius r (Wallace and Hobbs, 2006)

has the same wavelength as the outgoing light (Rayleigh, Mie scattering and geometric optics). Scattering can also be inelastic when the photon changes its energy during the scattering process. The dominant inelastic scattering process on air molecules in the atmosphere is called Raman scattering.

Raman Scattering and Ring Effect

Raman scattering is an inelastic scattering process resulting from interactions of the photon with rotational and vibrational transitions in the scattering molecule. This inelastic scattering can occur in both directions. The scattering molecule can receive energy from the incoming photon and the incoming wavelength will be longer than the scattered wavelength. The scattering molecule can also transfer energy to

the incoming photon and the incoming wavelength will be shorter than the one of the scattered light. These two processes correspond to two branches of the Raman scattering. The Stokes branch corresponds to an increase of the wavelength after scattering. This case is much more probable than the anti-Stokes case, where the wavelength of the incoming photon is decreased. The caused shift can be of the order of several nm. If the change of wavelength due to Raman scattering $\Delta\lambda$ is at least in the same order as the width of an absorption line it can even change the appearance of these lines. This effect is called the Ring effect. It was first observed by Grainger and Ring (1962) who found out that the Fraunhofer lines they measured in blue sky were a few percent less deep as the one they measured in direct sunlight. This filling-in of the Fraunhofer lines can be explained due to inelastic scattering processes. Today most authors agree that the main contribution to this filling-in comes from rotational Raman scattering with small contributions from vibrational Raman scattering. Since the contribution of the Ring-effect can be one magnitude larger than the trace gas absorptions it has to be included in the trace gas retrieval. This can be done by using so called Ring spectra that can be retrieved empirically or they can be simulated (Richter, 1997). In this thesis, the Ring spectra for NO_2 retrieval were simulated.

4 Differential Optical Absorption Spectroscopy

To observe the condition of the Earth's atmosphere, several measurement techniques have been developed. An important distinction between these techniques is their ability to perform in-situ or remote sensing.

While in-situ measurements measure trace gas concentration at a single spot very close to the instrument, remote sensing techniques allow measurements from great distance.

Since absorption spectroscopy is a widely used tool for investigating the chemical composition of gases it is not surprising that it has become a powerful tool for remote sensing of the atmosphere. Today DOAS spectroscopy is one of the most established methods for remote sensing of the atmosphere. During the last decades it has been adapted for a growing number of trace gases. At the IUP of the University of Bremen DOAS measurements were established and adopted since the mid 1990s (see (Richter, 1997)).

4.1 Classical Absorption Spectroscopy

The basis of all spectroscopic methods for trace gas absorptions is Lambert Beer's law, often also referred to as Bouguer-Lambert law, that describes the extinction of a light beam after passing a medium. It was first formulated by Pierre Bouguer in 1729 (Bouguer, 1729): 'In a medium of uniform transparency the light remaining in a collimated beam is an exponential function of the length of the path in the medium'. Later it was presented in different forms by Lambert (1760) and Beer (1852). Here the law shall be referred to as Lambert Beer's law. In a form suitable to describe the absorption properties of a gaseous medium the law describes the wavelength dependant extinction of a collimated light beam passing an isotropic medium of

length L with number density n and absorption cross section $\sigma(\lambda)$, which follows an exponential law:

$$I(\lambda) = I_0(\lambda) \cdot \exp(-\sigma(\lambda) \cdot n \cdot L) \quad (4.1)$$

$I_0(\lambda)$ is the intensity of the light beam emitted by a suitable light source and $I(\lambda)$ is the intensity of that light beam after passing the medium. Often the exponent of the function is referred to as optical thickness $\tau = \sigma(\lambda) \cdot n \cdot L$. Figure 4.1 shows the principle of absorption spectroscopy experiments that make use of the absorption of electromagnetic radiation of matter, e.g. for trace gas detection or to get deeper knowledge of the wavelength dependent absorption properties of a substance.

(Platt and Stutz, 2008)

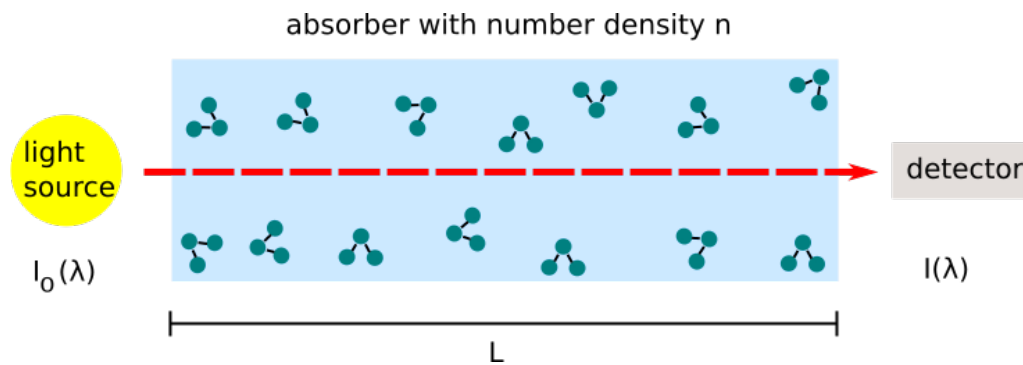


Figure 4.1: Sketch of the typical set up of trace gas absorption spectroscopy. A light source sends a light beam with initial intensity I_0 through a Volume of length L that contains the trace gas of interest with number density n . The intensity of the light beam after passing the medium is measured by a suitable detector.

In the atmosphere the application of Lambert Beer's law is more challenging. For example the determination of the intensity I_0 of the light source before it passes the medium proves to be difficult because the solar spectrum as reference spectrum can only be measured outside the Earth's atmosphere.

In the 1920s Dobson and Harrison (1926) developed a *differential* optical absorption spectrometer to measure atmospheric ozone. The absorption cross section of ozone was already known by laboratory measurements by that time. In their experiment Dobson and Harrison used the Sun as a light source and measured absorption spectra at two different wavelengths in the UV, one where ozone shows strong absorption,

one where ozone shows almost no absorption as a reference spectrum. They found out that the ratio of the measured intensities depends on the difference of the absorption cross sections at both wavelengths and the concentration of the absorber integrated along the light path.

4.2 The DOAS-Method

Based on the first atmospheric trace gas measurements using differential absorption spectroscopy by Dobson and Harrison in the 1920s further development resulted in the Differential Optical Absorption Spectroscopy (DOAS) method.

Figure 4.2 shows a sketch of the different absorption and scattering sources in the open atmosphere.

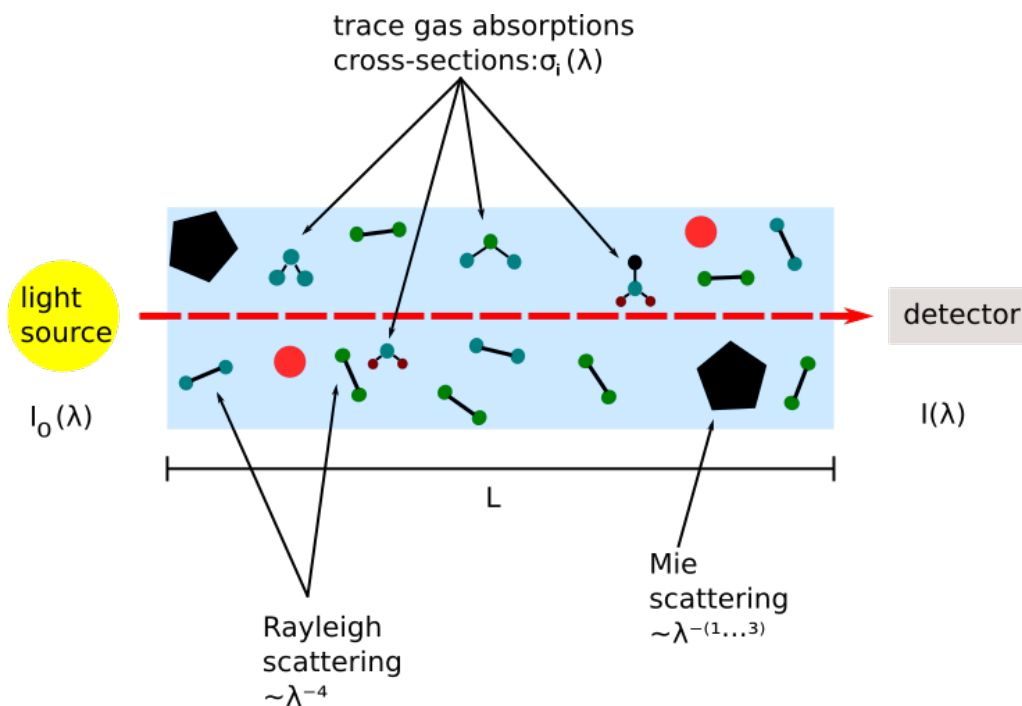


Figure 4.2: Sketch of the absorbers and scattering sources in the open atmosphere. In contrast to the situation assumed by Lambert Beer's law several absorbers with absorption cross section $\sigma_i(\lambda)$ are present. In addition light will be Rayleigh scattered at air molecules (mostly N_2 and O_2) and Mie scattered at spherical particles (aerosols or droplets).

Contrary to the assumptions made for Lambert Beer's law not only the absorption of the species of interest has an influence on the intensity decay while passing the medium. In the free atmosphere the sunlight will be absorbed by several trace gas absorbers with absorption cross section $\sigma_i(\lambda)$ and number density n_i . Unlike under laboratory conditions in the atmosphere number density and absorption cross section depend on the light path s since they vary with altitude. In addition elastic Rayleigh- and Mie scattering processes (on small air molecules) as well as inelastic Raman scattering (Ring-Effect) will occur. To account for all these intensity sinks Lambert Beer's law has to be expanded accounting for N absorbers and the three different scattering processes by using *pseudo absorptions* with cross sections $\sigma_j(\lambda, s)$ and number density $n_j(s)$:

$$I(\lambda) = I_0(\lambda) \cdot \exp \left(- \int \left(\underbrace{\sum_{i=1}^N n_i(s) \sigma_i(\lambda, s)}_{\text{absorption}} + \underbrace{n_j(s) \sigma_j(\lambda, s) |_{j=\text{Rayleigh, Mie, Ring}}}_{\text{scattering}} \right) ds \right) \quad (4.2)$$

(Platt and Stutz, 2008)

To simplify equation 4.2 it is assumed that the absorption cross sections are independent of the light path s . This is of course an approximation, since the absorption cross sections are slightly varying with temperature. Due to the temperature profile of the atmosphere the cross sections thus also depend on the position in the light path. Regarding that most trace gases are concentrated in certain layers of the atmosphere, one can assume the cross section for the typical temperature of the assumed trace gas height. For some trace gases like ozone it is useful to use different temperatures simultaneously to account for UV absorptions by the ozone layer in the stratosphere as well as absorptions by ozone in the boundary layer. Using this approximation leads to a simplification of the integral in equation 4.2 to the so called slant column density (SCD):

$$\text{SCD}_i = \int n_i(s) ds \quad (4.3)$$

The SCD is thus the integrated number density of a trace gas along the light path with the unit $\frac{\text{molec}}{\text{cm}^2}$.

For atmospheric measurements it's impossible to quantify all the contributors to equation 4.2. The principle of the DOAS method is therefore to separate all these contributors into those varying fast with wavelength (narrow band structures) and those that vary slowly with wavelength (brought band structures). This *differentiation* of cross sections into a slow σ_{i0} and a fast varying part σ'_i is responsible for the D in DOAS: $\sigma = \sigma_{i0} + \sigma'_i$. The separation of the different contributors is shown in table 4.1. The brought band structures are then summarised into a low order

brought band structures	narrow band structures
<ul style="list-style-type: none"> • elastic scattering: Rayleigh- and Mie-scattering • brought band structured absorption cross section σ_{i0} • effects of clouds, turbulences and instrumentation 	<ul style="list-style-type: none"> • inelastic scattering: Ring effect • narrow band structured absorption cross section σ'_i

Table 4.1: Separation of the different processes contributing to the measured solar spectrum into narrow band and brought band structures.

polynomial $\alpha = \sum_p a_p \lambda^p$. The Ring effect is treated as a separate absorber with cross section σ'_i . Equation 4.2 simplifies to:

$$I(\lambda) = I_0(\lambda) \cdot \exp \left(- \sum_{i=1}^N \sigma'_i \cdot \text{SCD}_i + \sum_p a_p \lambda^p \right) \quad (4.4)$$

Taking the natural logarithm and rearranging leads to the optical depth τ :

$$\tau = \ln \left(\frac{I_0}{I} \right) = \sum_{i=1}^N \sigma'_i \cdot \text{SCD}_i + \sum_p a_p^* \lambda^p \quad (4.5)$$

where $\ln \alpha$ has been included into the low order polynomial as varying smoothly with wavelength. (Peters, 2013)

Equation 4.5 is called the DOAS equation. In order to retrieve trace gas slant column densities a least squares fit is performed to fit the unknown parameters SCD_i and the coefficients of the polynomial a_p^* . The σ'_i are known from laboratory measurements. The fitted optical depth τ_{fit} matches the measured optical depth τ except for a residual spectrum $r(\lambda)$:

$$\tau = \tau_{\text{fit}} + r(\lambda) \quad (4.6)$$

The least square fit minimizes the residual $\sum_i r(\lambda)_i^2$. A measure for the quality of the fit is the root mean square (RMS) of this residual:

$$\text{RMS} = \sqrt{\frac{1}{N} \sum_{i=1}^N r(\lambda)_i^2} \quad (4.7)$$

(Richter, 1997)

When choosing the wavelength region for the fit (also referred to as fitting window) several criteria have to be considered. The most important are:

- The strongest differential absorption lines of the species of interest should be in the fitting window
- Minimise other absorbing compounds in the wavelength region
- Only small correlation between different cross-sections
- Avoiding strong Fraunhofer lines in the fitting window

(Wittrock, 2006)

4.3 Measurement Geometry

In space-borne DOAS measurements a record of the reference spectrum I_0 is possible by simply recording a solar spectrum before it passes the atmosphere. The only absorption lines in this spectrum are the Fraunhofer lines. For ground-based DOAS measurements it is obviously not possible to remove atmospheric absorption from the light path. One possibility would be to use the solar spectrum recorded by a

space-borne instrument as a reference spectrum for the ground based measurements. Nevertheless this approach is not recommendable, since instrumental effects would not cancel out by taking $\frac{I}{I_0}$, leading to structures that could mask the absorption signals (Peters, 2013).

An approach for a reference spectrum taken with the same instrument is to choose zenith sky measurements as a reference. Depending on the observed species' position in the atmosphere different measurement methods have been developed. For the observation of tropospheric trace gases off-axis measurements are useful, with viewing directions deviating from the zenith direction. This method is called *multi-axis* DOAS, in the following referred to as MAX-DOAS (Wittrock and Oetjen, 2004)(Hönninger, 2004). Figure 4.3 shows the viewing geometry of ground based MAX-DOAS measurements. For small elevation angles close to the horizon the light

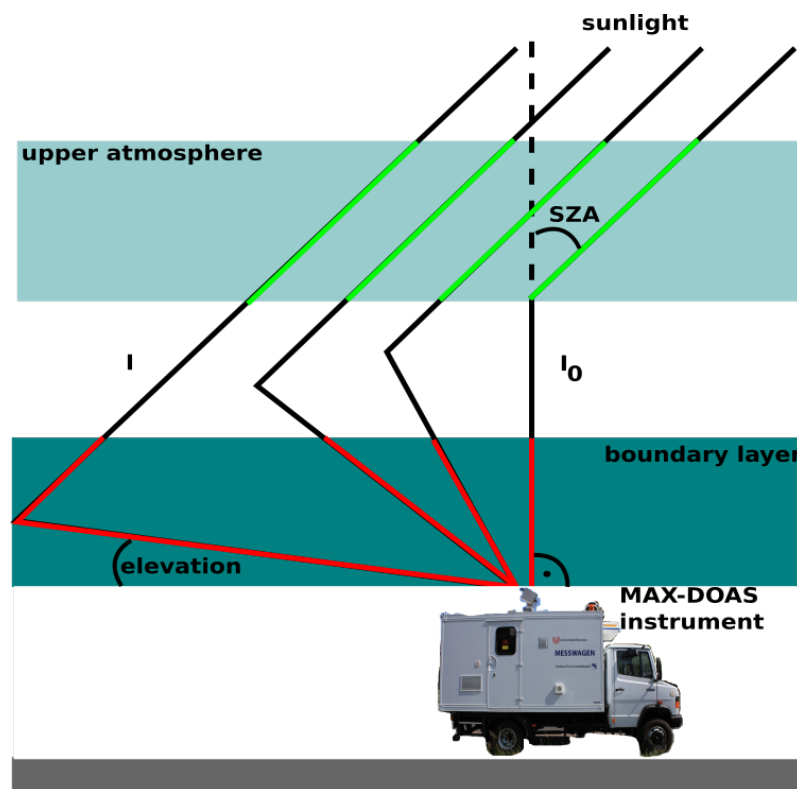


Figure 4.3: Viewing geometry of MAX-DOAS measurements: While the path length in the upper atmosphere is constant (approximately) for all elevations (green line), the light path in the boundary layer increases with decreasing elevation angle (red line).

path in the troposphere is elongated, while the light path in the stratosphere stays almost constant. This has the effect that the sensitivity of the measurements for trace gases in the surface layer can be enhanced (Wittrock and Oetjen, 2004).

The light path is strongly influenced by viewing conditions, e.g. aerosol load and cloud cover that increase the scattering probability. In addition Rayleigh scattering ($\propto \lambda^{-4}$) increases the scattering probability of UV photons and therefore shortens the mean free path. Therefore the last scattering point of a UV photon is in average closer to the instrument than the one for a visible photon. This effectively reduces the light path of UV radiation. For low elevation angles (the lowest in figure 4.3) the last scatter point lies within the boundary layer. For higher elevation angles the last scatter point of the sunlight lies above the boundary layer. In general the scattering probability decreases with decreasing air density and therefore exponentially with height (barometric formula).

The prolongation of the light path in the surface layer is mostly depending on the applied elevation angle (the viewing angle above the horizon) and not so much on the solar zenith angle (SZA) (the angle between zenith and position of the Sun). Therefore high sensitivity for absorbers in the atmospheric boundary layer can be achieved throughout the day.

(Wittrock and Oetjen, 2004)(Hönninger, 2004)

As a reference spectrum a zenith spectrum measured shortly before or after the off-axis measurement is chosen. This has the advantage that instrumental and weather-effects (turbulences, clouds) cancel out best by dividing I by I_0 since they vary with time.

In contrast to a reference spectrum recorded in space the zenith sky reference spectrum I_0 will contain structures from atmospheric trace gas absorptions. Therefore the retrieved slant column densities will not be *absolute* like this is the case for space-borne retrievals, but the *difference* of the slant columns obtained from I and I_0 . They are referred to as *differential* slant column densities (SCD) (Peters, 2013):

$$\text{SCD} = \text{SCD}_{\text{off-axis}} - \text{SCD}_{\text{zenith}} \quad (4.8)$$

4.4 Concept of Air Mass Factors and Vertical Columns

The DOAS-Fit provides differential slant column densities, the concentration of the species of interest integrated along the effective light path in $\frac{\text{molec}}{\text{cm}^2}$. The effective light path is the average of an infinite number of light paths weighted by the intensity of radiation reaching the instrument, hence the most probable light path under given conditions (Richter, 1997). It depends on viewing conditions, elevation angle and position of the Sun, which makes the interpretation of SCDs quite difficult. Hence a measure independent of the light path and thus the measurement conditions is desirable. Therefore the SCDs are converted into vertical column densities (VCDs), which are the trace gas concentrations integrated over altitude z (Peters, 2013):

$$\text{VCD} = \int n(z)dz \quad (4.9)$$

The factor between VCD and SCD is called Air Mass Factor (AMF) and depends on the Sun's zenith angle ϑ , elevation angle α , relative azimuth angle between the Sun and the line of sight φ and wavelength λ (Richter, 1997):

$$\text{AMF}(\vartheta, \alpha, \varphi, \lambda) = \frac{\text{SCD}(\vartheta, \alpha, \varphi, \lambda)}{\text{VCD}} = \frac{\text{SCD}_{\text{off-axis}} - \text{SCD}_{\text{zenith}}}{\text{VCD}} \quad (4.10)$$

Using $\text{SCD}_{\text{zenith}} = \text{VCD} \cdot \text{AMF}_{\text{zenith}}$ leads to the conversion formula for VCDs belonging to SCDs derived by ground based measurements:

$$\text{VCD} = \frac{\text{SCD}}{\text{AMF}_{\alpha} - \text{AMF}_{\text{zenith}}} \quad (4.11)$$

For accurate calculations of AMFs advanced radiation transport models are necessary. At the University of Bremen the common model is SCIATRAN. It calculates the radiance at the end of the light path for given ϑ , α , φ and λ using the absorbers vertical profile and absorption cross section (V.V.Rozanov and A.V.Rozanov, 2013).

Under certain conditions these calculations can be avoided by using approximations for the AMF.

Geometric Approach for AMF

To derive the AMF of tropospheric trace gases a simple geometric approach can be used (e.g. (Hönninger, 2004)). In this approximation the AMF only depends on the elevation angle α .

$$\text{AMF}_{\text{trop,geo}} = \frac{1}{\sin \alpha} \quad (4.12)$$

The corresponding tropospheric vertical column density is given by:

$$\text{VCD}_{\text{trop,geo}} = \frac{\text{SCD}_{\alpha} - \text{SCD}_{90^{\circ}}}{\text{AMF}(\alpha) - \text{AMF}(90^{\circ})} = \frac{\text{SCD}}{\frac{1}{\sin \alpha} - 1} \quad (4.13)$$

This approximation is only valid when the scattering point lies above the layer of the trace gas of interest. Since it also neglects change of the light path due to multiple scattering (e.g. due to aerosols) and dependency of the solar zenith angle ϑ , it is in general only useful under clear sky conditions for $\vartheta < 80^{\circ}$ and $\alpha \geq 10^{\circ}$. (Wagner et al., 2010)(Pinardi and Hendrick, 2008)

4.5 Conversion to Volume Mixing Ratios

In-situ devices do not measure column densities, but the concentration of a trace species as a volume mixing ratio (VMR), hence the atmospheric fraction of a trace gas. The VMR is defined as the ratio between the number density of a trace species to the number density of the surrounding air. Using the ideal gas law $pV = nRT$ and Avogadro's constant $N_A = \frac{N}{n}$ yields

$$\text{VMR} = \frac{n_{\text{species}}}{n_{\text{air}}} = n_{\text{species}} \cdot \frac{N_{\text{air}}}{V_{\text{air}}} = n_{\text{species}} \cdot \frac{R \cdot T_{\text{air}}}{p_{\text{air}} \cdot N_A} \quad (4.14)$$

To estimate n_{species} two different approaches have been used:

Geometric Approach

The geometric approach uses the tropospheric vertical column density calculated using the geometric AMF approximation and the mixing layer height (MLH) to calculate the number density of the observed trace gas $n_{\text{species}} = \frac{\text{VCD}_{\text{trop}}}{\text{MLH}}$. The MLH can either be measured using for example a LIDAR, or typical values have to be assumed. The resulting VMR is given by:

$$\text{VMR}_{\text{geom}} = \frac{\text{VCD}_{\text{trop}}}{\text{MLH}} \cdot \frac{R \cdot T_{\text{air}}}{p_{\text{air}} \cdot N_A} \quad (4.15)$$

Using O_4 as Tracer

For horizontal viewing directions a new method using the oxygen collision complex O_4 as a tracer for the effective path length has been introduced by Gomez et al. (2013). It is valid under the assumption, that for all used viewing geometries (elevation 0° and 90° as reference) the scattering altitude is the same and close to the station level. Using the well known number density of O_4 and the SCD of O_4 , measured at the same time as the trace species of interest, one can calculate the effective path length L by:

$$L_{O_4} = \frac{SCD_{O_4,\alpha} - SCD_{O_4,90^\circ}}{n_{O_4}} \quad (4.16)$$

The number density of the species of interest can be calculated using L_{O_4} and the fitted SCDs of the species:

$$n_{\text{species}} = \frac{SCD_{\text{species},\alpha} - SCD_{\text{species},90^\circ}}{L_{O_4}} \quad (4.17)$$

5 Instrumentation

In the following chapter the technical set up of a MAX-DOAS system, that allows absorption spectroscopy in the UV and visible range will be presented.

5.1 Experimental Set-Up of a MAX-DOAS System

The key components of a DOAS system are shown in figure 5.1:

- **Receiving optics:** The incoming scattered sunlight is collected by a telescope unit that is mounted on a pan-tilt-head. A detailed description of the telescope unit, its functions and components is given in section 5.2.
- **Connective optics:** To transmit the light signal from the telescope unit to the spectrometers a y-shaped light fibre is used. In the telescope unit it starts with one bundle of 76 cylindrical single quartz fibres. After 20 m the bundle splits into two bundles consisting of 38 quartz fibres. The fibres end in a connecting piece, where all fibres are vertically aligned to a slit of approximately 150 μm width that form the entrance slit for the two spectrometers.

Using quartz fibres as connective optics has two advantages:

- 1) It depolarises the scattered sunlight that has been polarised by Rayleigh scattering before it enters the spectrometer. Polarisation effects inside the spectrometer are overcome this way.
 - 2) It allows flexibility for the measurement's set-up. For example the telescope unit can be placed outside, while the spectrometers are inside a building or the measurement car, shielded from environmental influences.
- **Spectrometers:** The MAX-DOAS system uses two spectrometers. One is operating in the visible range, the other in the UV. Because the system uses two spectrometers operating in different spectral ranges it is called a two-channel-system. To avoid temperature dependent drifts in the spectra the

spectrometers are thermally stabilised. Therefore they are stored in thermally insulated boxes and kept at a constant temperature of 35° C by using heat foils connected with an electronic control loop. Set-up, functionality and manufacturer's specifications of the spectrometers in use for this thesis are presented in section 5.3.

- **CCD detectors:** The wavelength separated spectra leaving the spectrometers are focussed on the charge coupled device (CCD) chip. In section 5.4 the principle functionality of a CCD detector is described and the manufacturer's specifications of the CCDs in use are summarised.
- **Computer:** The CCD detectors already include an ADC (analogue to digital converter) and an amplifier. The signal is transmitted via a USB cable to the controlling computer on that the measurement software AMAX_ OMA is running.
- **Measurement software:** The measurement software AMAX_ OMA (Richter, 1997) does not only record the measured spectra. It is also the central tool to control the spectrometer and CCD settings. Via a connection between computer and telescope box AMAX_ OMA also controls the elevation angle and azimuthal viewing directions by operating the pan-tilt-head, receives the signal of the video camera in the telescope box and controls the power supply for the line lamp.
- **Software for evaluation, database for absorption cross-sections and modelling software:** Section 5.5 presents the software used to evaluate the spectra recorded by the MAX-DOAS system. Beside the software a data base of the absorption cross sections is necessary for the DOAS fit. The absorption cross sections are taken from publications of experimental measurements for the trace gas of interest. The modelling software SCIATRAN is used to calculate Ring-cross sections used for the DOAS fit and air mass factors that are necessary to transform slant column densities into vertical column densities. A short overview of SCIATRAN is also given in section 5.5.

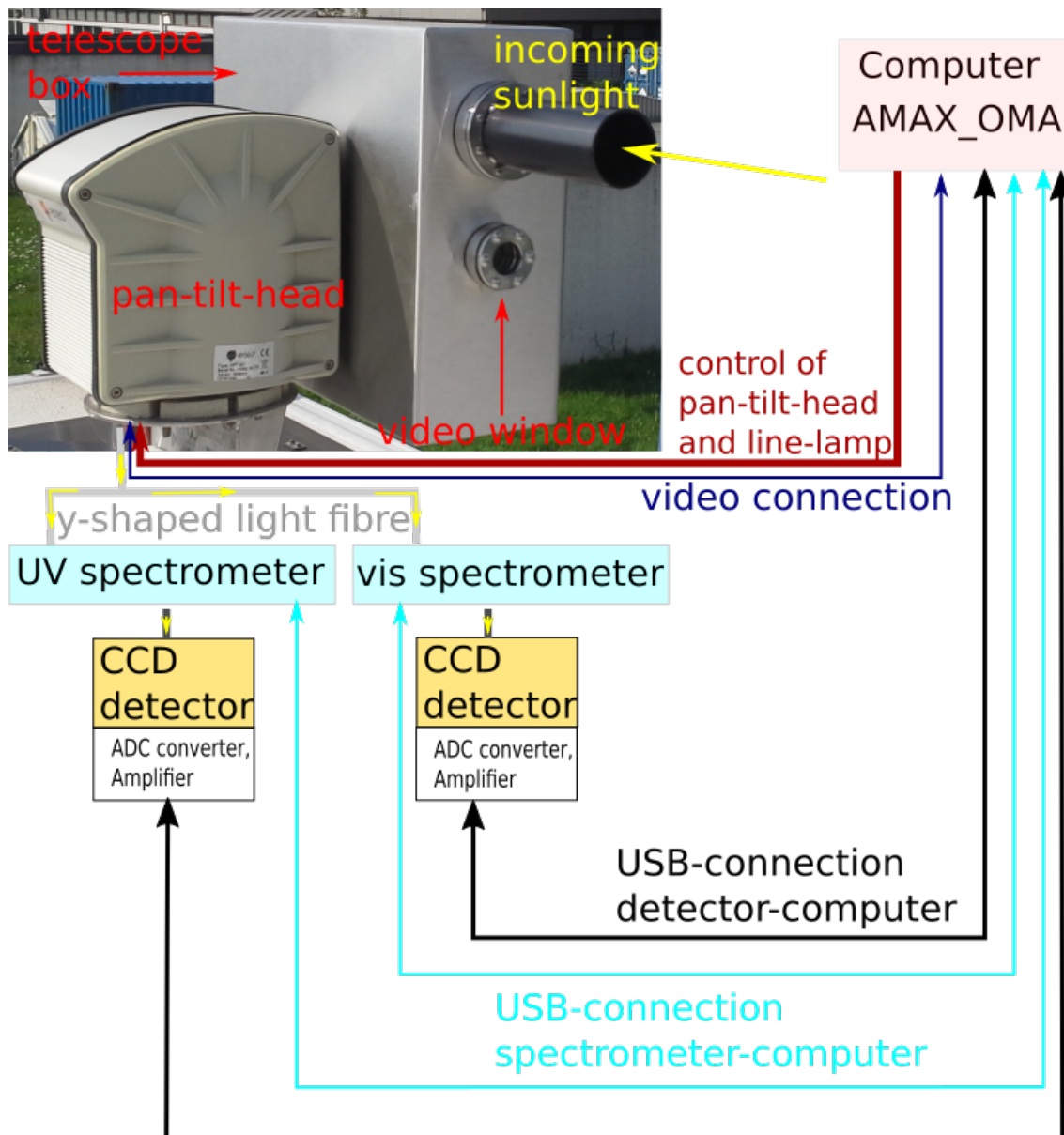


Figure 5.1: Sketch of the set-up of a MAX-DOAS system. The incoming scattered sunlight is collected by a telescope unit that is mounted on a pan-tilt-head. The light is transmitted to the spectrometers operating in the UV and visible range via a y-shaped light fibre. The CCD detector converts the wavelength separated spectra into an electric signal that is transmitted to a computer with the measurement software AMAX_OMA.

5.2 Telescope Unit for MAX-DOAS Measurements

5.2.1 Telescope Box

The receiving optics of the DOAS set-up are inside a telescope box which is mounted on a pan tilt head which allows to change between different azimuthal viewing directions and elevation angles. The incoming sunlight enters the telescope via a quartz glass window that is shielded by the lens hood. The lens hood is necessary to reduce stray light inside the telescope box. The quartz glass window is used because in contrast to normal glass it does not absorb in the UV region. The incoming light is focussed on the end of a quartz fibre light cable via a converging lens. The light cable is connected with both spectrometers. The field of view of the telescope unit is the full opening angle of this optical set-up. It is predominately limited by the finite size d of the entrance of the optical fibre bundle. Ideally the converging lens would focus the incoming light on a single spot. In reality this single spot is the light fibre bundle of diameter d . The optical path in this situation is illustrated in figure 5.3. The half opening angle α is given by:

$$\tan \alpha = \frac{d}{2f} \quad (5.1)$$

Using $d \approx 2$ mm and the focal distance of the lens of $f = 100$ mm one obtains $\alpha \approx 0.573^\circ$. This results in a field of view of $2 \cdot \alpha \approx 1.145^\circ$. This theoretical value for the field of view has been confirmed experimentally for telescopes of same type by Peters (2013). In addition to the entrance optics the telescope box contains a video camera that has a separate viewing window under the quartz glass window. The usage of a video camera assists during manual alignment of the viewing directions and measurement condition surveillance. The gravity driven shutter is used for dark and line lamp measurements. When the elevation angle is set to -90° so that the telescope is looking straight downwards, the shutter closes and shields the entrance optics from incoming sunlight. Automatic line lamp measurements are useful for the regular calibration of the system. Therefore a HgCd line lamp is installed in the telescope box allowing automated line lamp measurements for example at night. To avoid humidity in the telescope box a drying agent is installed. The out- and input cables for power and communication are leaving the telescope box via waterproofed ports.

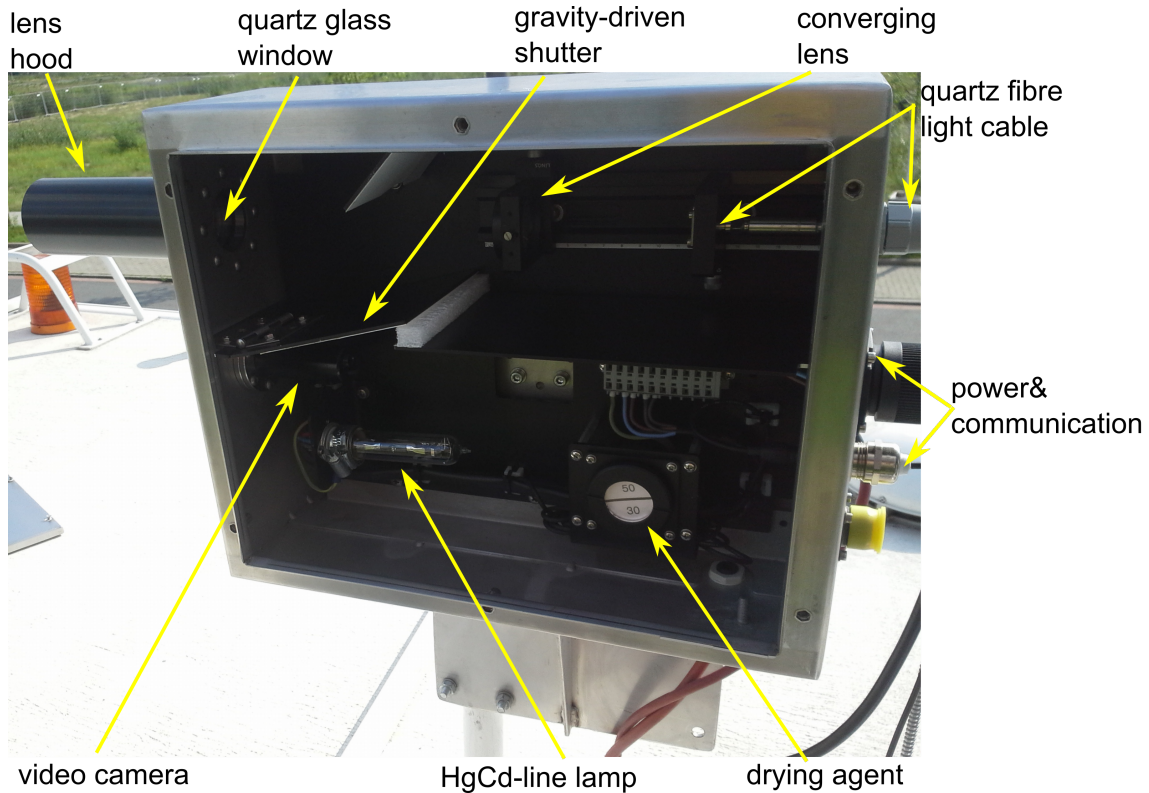


Figure 5.2: Photograph of the MAX-DOAS telescope box mounted on a pan-tilt-head. The yellow arrows label the different elements in the telescope box.

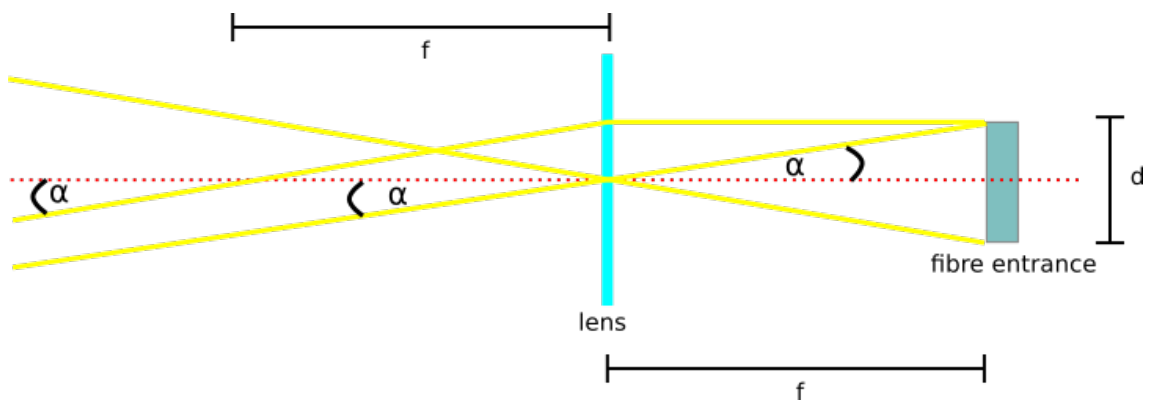


Figure 5.3: Sketch of the optical path in the telescope. The incoming light is focused via a lens with a focal distance f on the entrance of the optical fibre of diameter d . The full opening angle of the entrance optics is given by $2 \cdot \alpha$.

5.2.2 Pan-Tilt-Head and Set-Up

The telescope box is mounted on a pan-tilt-head that allows to choose between different elevation angles and azimuthal viewing directions with a pointing accuracy of 0.2° (Peters, 2013). The pan tilt-head can be mounted on a tripod for land campaigns or on a fixed mounting plate. For the mobile use the telescope box has been mounted on a fixed mounting on the roof of the IUP measurement car.

5.3 Spectrometers

For the instrumental set-up in the scope of this thesis two grating spectrometers, one optimized for the visible and one for the UV range have been used. The manufacturer's specifications for both spectrometers are given in table 5.1. The set-up of the spectrometers and the optical path in each spectrometer is shown in figure 5.4. The light enters the spectrometer via an entrance slit A with a width of approximately $150 \mu\text{m}$ that is formed by the vertically aligned quartz fibres of the connecting light cable. The entrance slit is in the focal plane of the high reflective collimating mirror (or mirror system) B. The incoming light is reflected by the collimating mirrors. The collimated parallel light is falling onto a reflective grating mounted on a motorised table. Each grating consists of a different number of many straight grooves parallel to the entrance slit. The grooves have been ruled onto an optically smooth glass substrate or have been produced by holographic techniques. The whole grating surface is coated with a high reflective layer, that can be metal or a dielectric film. The motorised table allows a change of the grating's position and hence change of the center wavelength. It also allows a change between the different gratings. The light reflected by the grating is separated by wavelength and focussed via a focussing mirror (or mirror system) D onto a CCD chip of a CCD detector E in the focal plane of D.

Spectrometer	SP 2150	Isoplanar SCT 320
Focal length	150 mm	320 mm
Focal plane size	25 mm wide x 10 mm high	27 mm wide x 14 mm high
Astigmatism (at edges of focal plane)	690 μm	Zero (0) at all wavelengths
Aperture ratio	F/4	F/4.6
CCD resolution (20 μm pixels)	0.4 nm	0.08 nm
Wavelength accuracy (mechanical)	± 0.25 nm	± 0.2 nm
Wavelength repeatability (mechanical)	± 0.05 nm	± 0.015 nm

Table 5.1: Characteristics of the spectrometer in use for the visible (SP 2150) and the UV range (Isoplanar SCT 320).

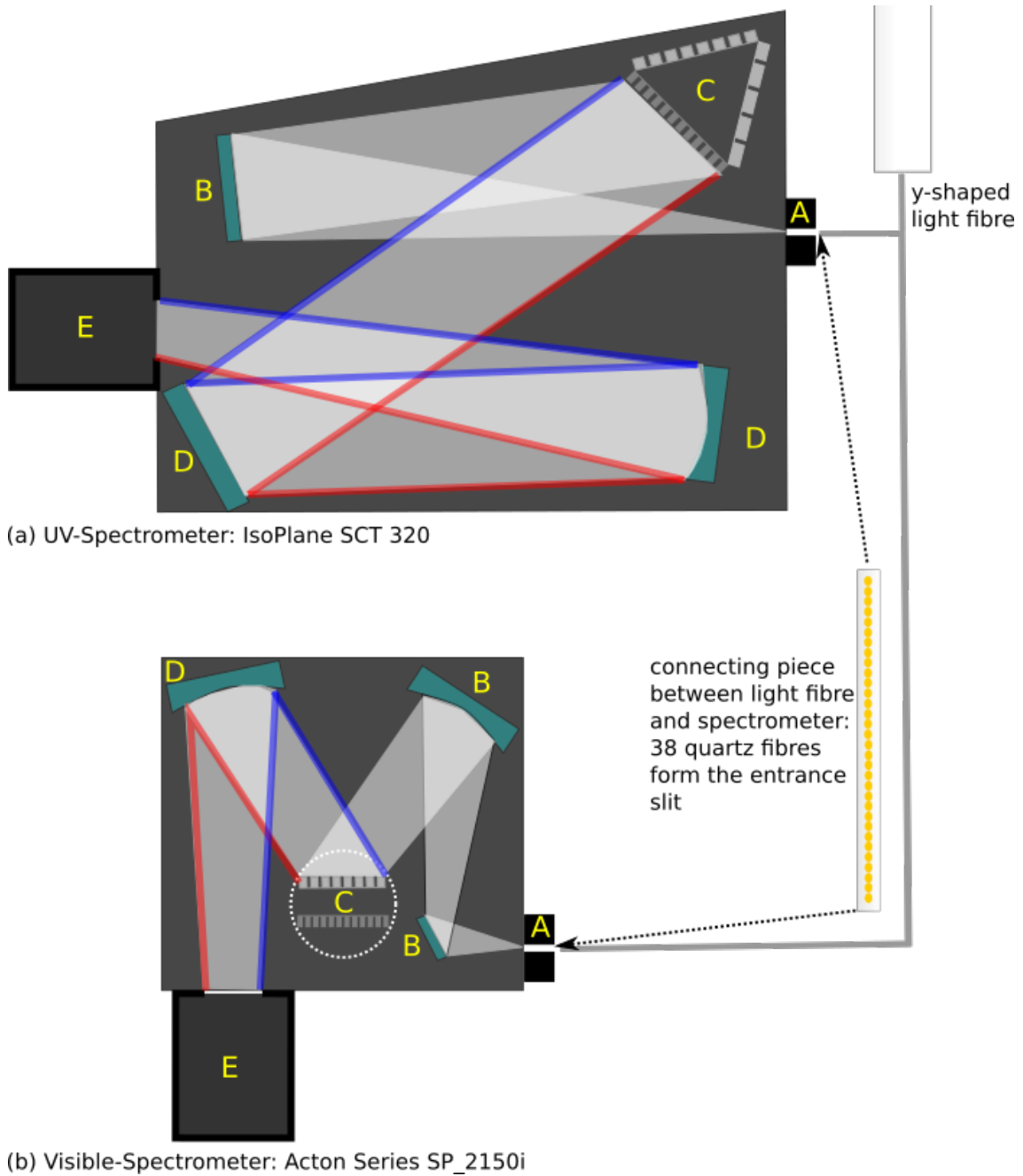


Figure 5.4: Set-up and optical path for the spectrometers used in the UV and the visible region. The sunlight collected by the telescope unit is transmitted via the y-shaped light fibre that ends in two connecting pieces that form the entrance slit ($\approx 150 \mu\text{m}$) of the spectrometers (A). The light is projected via a collimating mirror system (B) on one of the available gratings (C). The gratings are fixed on a motorised table to change the position of the grating and hence the center wavelength. It also allows change between the gratings. The light that has been wavelength separated by the grating is lead via focusing mirrors (D) on the CCD detector (E).

5.3.1 Reflection Gratings

Basic considerations

The many coherent illuminated grooves of a reflective grating can be considered as small radiation sources. Each of these grooves diffracts the incident light that has a wavelength λ of the same magnitude as the groove width d into a large range of angles $\approx \frac{\lambda}{d}$ around the direction of geometrical reflection. The total reflected light consists of a coherent superposition of the partial contributions. The intensity distribution behind the grating is determined by interference of the partial waves emitted from different grooves. Only directions where all partial waves are in phase result in constructive interference leading to large total intensities. For all other directions the contributions are cancelled out due to destructive interference.

Figure 5.5 (a) shows a parallel light beam incident onto two neighbouring grooves with an angle of incidence to the grating normal α . The emergent angle β is determined by the process of interference of partial waves that is described above. Constructive interference happens for a light path difference $\Delta s = \Delta s_1 - \Delta s_2$ that fulfils: $\Delta s = m\lambda$, where m is an integer. Using $\Delta s_1 = d \cdot \sin \alpha$ and $\Delta s_2 = d \cdot \cos \beta$, where d is the groove spacing yields the grating equation:

$$\Delta s = d \cdot (\sin \alpha \pm \cos \beta) = m\lambda \quad (5.2)$$

The plus sign is necessary when α and β are on the same side of the grating normal. Otherwise, like shown in figure 5.5 (a) the minus sign has to be taken. (Demtröder, 2008)

Blaze Angle

The gratings are blazed. This means that their reflectivity is optimised for a certain wavelength. The gratings in use with the visible spectrometer are blazed for a wavelength of 500 nm, the UV gratings are blazed for a wavelength of 300 nm. To blaze a grating the shape of the grooves and the *blaze angle* of the grating are adjusted. Figure 5.5 (b) illustrates the blaze angle. The blaze angle Θ is the angle between the groove normal and the grating normal. Together with the diffraction

angle β it determines the reflectivity of the grating $R(\beta, \Theta)$. The optimum value for the reflectivity is reached for a blaze angle fulfilling:

$$\Theta = \frac{\alpha - \beta}{2} \quad (5.3)$$

Since the diffraction angle β under that constructive interference occurs depends on the wavelength λ the blaze angle has to be specified for the desired optical range (Demtröder, 2008).

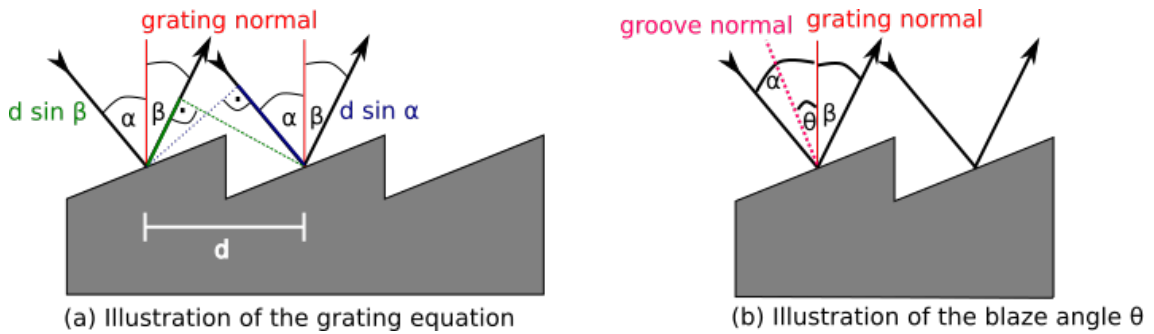


Figure 5.5: Illustration of the grating equation (a) and the blaze angle (b).

Resolving power

The spectral resolution of the spectrometer can be derived using the grating equation 5.2. Differentiating this equation by λ for a given angle α yields the angular dispersion:

$$\frac{d\beta}{d\lambda} = \frac{m}{d \cdot \cos \beta} = \frac{\sin \alpha \pm \sin \beta}{\lambda \cos \beta} \quad (5.4)$$

This wavelength dependent angular dispersion is responsible for the spacial separation of the incident light by wavelength.

The spectral resolving power of a grating spectrometer can be derived using the Rayleigh criterion. It states that two lines λ and $\lambda + \Delta\lambda$ are just resolved when the maximum of $I(\lambda)$ falls to the adjacent minimum of $I(\lambda + \Delta\lambda)$. For the spectral resolution R this leads to the condition:

$$R = \frac{\lambda}{\Delta\lambda} = \frac{Nd(\sin \alpha \pm \sin \beta)}{\lambda} \quad (5.5)$$

where N is the total number of illuminated grooves. Inserting again the grating equation this reduces to:

$$R = \frac{\lambda}{\Delta\lambda} = m \cdot N \quad (5.6)$$

Hence the theoretical resolution is depending on the total number of illuminated grooves N and the diffraction order m . However in reality this resolution is often not reached, because of the finite slit width and diffraction on limiting apertures. In addition the grating has to be optimally illuminated (Demtröder, 2008).

5.3.2 Further Specifications of the Spectrometer

- The **Focal length** of an optical system is a measure how much a system converges and diverges light. It is the distance over that initially collimated light beams are brought to focus.
- **Astigmatism** is an effect that parallel light beams have different focus. So for the visible spectrometer the focus of the light beam at one edge of the focal plane differs by $690 \mu\text{m}$ of the one at the other edge of the plane. The UV spectrometer shows zero astigmatism.
- **Apertures** are openings in optical systems that limit the expansion of a bundle of light beams. Together with the focal length of the optical system it determines the cone of the light bundle that comes to focus in the image plane on the CCD chip. The aperture ratio is given as an f-number and is the ratio of the systems focal length to the diameter of the entrance pupil. It is commonly noted as F/f-number (Smith, 2007).

5.4 Charge Coupled Device Detectors

The detectors in use with the spectrometers are charge coupled device (CCD) detectors. In the following subsection the general function of this type of photo-detectors and the characteristics for the quality of a CCD chip will be explained. In addition the manufacturer's specifications of the CCD detectors in use for the DOAS system presented in this thesis are summarised.

5.4.1 General Function of a CCD Detector

A CCD sensor is formed by multiple single pixels, which consist of an array of metal–oxide–semiconductor (MOS) junctions on a doped silicon substrate. The conversion from incoming light to a digital signal can be divided into three different processes:

- **Charge generation:** The photosensitive region of the CCD array is formed by a layer of a doped semiconductor most commonly p-doped silicon. Incident photons with sufficient energy (higher than the band gap) generate charge carriers (an electron hole pair for p-doped silicon) by exciting one or more electrons from the valence band into the conduction band. This process is based on the inner photoelectric effect.
- **Charge collection and transmission:** The transmission region is formed by an array of MOS capacitances. Each capacitance consists of an insulating silicon dioxide layer and polysilicon gates. A recombination of the electron hole pair is avoided by applying an electric field. The electric charges are collected in the depletion region of the MOS capacitors and lead to a change of charge. This change of charge can be shifted to the next MOS capacitance in the array by applying a sequence of suitable voltage steps. This process is illustrated in figure 5.6.

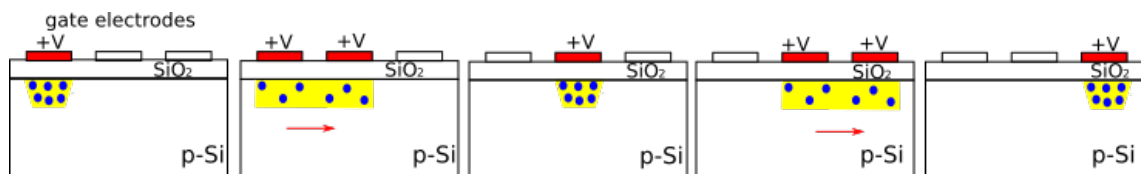


Figure 5.6: Sketch of the transmission of charge between neighbouring MOS capacitances. First the electric charges (blue) are collected in potential wells (yellow) by applying an electric voltage at the gate electrodes (red). Then the charge packets are shifted from one unit to the next by applying a frequency of suitable voltage steps on the gate electrodes.

- **Read out of charges using a shift register:** Charges are shifted from one unit to the next until they reach the last cell in the line of capacitors forming one cell in the CCD array. The last unit in the row dumps its charge to an

output register. The horizontal transport of charges is then stopped and each charge package is transported vertically to an output amplifier, which converts the charge into a voltage proportional to the intensity of the incident light. This cycle is repeated until all charges are read out. The shift register is shown in figure 5.7. The generated output is a sequence of voltages that can be converted to a digital signal by an ADC device (Demtröder, 2008). The digitalised signal is then stored in memory and sent to the computer via a USB cable.

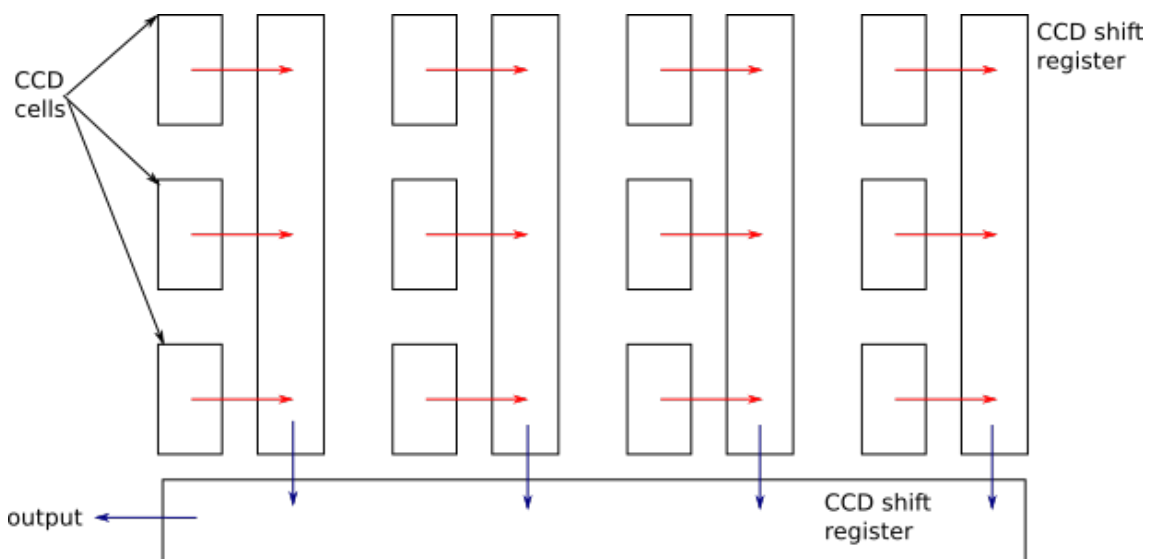


Figure 5.7: Charge transport in the shift register: In each CCD cell the charges are shifted horizontally until they reach the last unit in a line. There, the charges are guided to a output register. The horizontal transport of charges is then stopped and each charge package at the output register is transported vertically to an output amplifier, converted to a voltage and read out one by one. This cycle is repeated until all charges are read out. The time period for one cycle determines the read out time of the CCD and the dead time where no data can be measured.

5.4.2 Characteristic Data of CCD Devices

The characteristics of the CCD detectors in use for the DOAS system characterised in this thesis are listed in table 5.2.

In the following, the main parameters relevant for the characterisation of the quality of a CCD chip are explained.

Quantum efficiency

The quantum efficiency (QE) of a CCD detector is the percentage of photons hitting the detector's photoreactive surface that produce charge carriers:

$$\text{QE} = \frac{\text{converted electrons}}{\text{incident photon}} = \left[\frac{e^-}{h\nu} \right] \quad (5.7)$$

Since QE depends on the energy of the incoming photons $h\nu$ and thus on $\frac{1}{\lambda}$, QE is measured in dependence of the wavelength of the incoming light. The efficiency for photons with energies below the band gap is zero.

Commercial CCD detectors are optimized for different spectral regions using special coatings. For the detectors in use for DOAS spectroscopy, the quantum efficiency peak should be in the UV and visible region. Figure 5.8 shows the wavelength dependent quantum efficiency curves for both CCD detectors in use.

(Demtröder, 2008)

CCD model	PIXIS: 100 B	PIXIS: 2K BUV
Active area [mm ²]	26.8 x 2.0	27.6 x 6.9
Pixel size [μm^2]	20 x 20	13.5 x 13.5
Number of pixels	1340 x 100	2048 x 512
Dynamic range [bits]	16	16
Readoutnoise @ 2MHz [electron charges]	11 (typical), 16 (max)	14 (typical), 20 (max)
Dark charge [elec- trons/pixel/s]	@ -80°C: 0.001	@ -70°C: 0.001(typical), 0.006(max)
Peak Quantum efficiency [%]	95 @ 550 nm	67 @ 250 nm
Nonlinearity [%]	< 1 (@100kHz)	< 1 (@100kHz) < 2 (@2MHz)
Software selectable gains [electron charges]	High Capacity:4,8,16[e ⁻] Low Noise:1,2,4[e ⁻]	High Capacity:3,6,12 $\left[\frac{e^-}{ADU}\right]$ Low Noise:1.5,3,6 $\left[\frac{e^-}{ADU}\right]$
Deepest cooling temper- ature	-80°C	-70°C(typical) -75°C(min)
Thermostat precision	$\pm 0.05^\circ\text{C}$	$\pm 0.05^\circ\text{C}$

Table 5.2: Characteristics of the CCD detectors in use with the visible spectrometer (PIXIS: 100 B) and the UV spectrometer (PIXIS: 2K BUV) taken from the corresponding data sheets. Both CCDs are back illuminated. The selectable gains for the 2K BUV detector are given in the unit $\frac{e^-}{ADU}$, hence electric charges per analogue to digital unit (ADU), by the ADC. The gains for the 100 B are given in electric charges e^- .

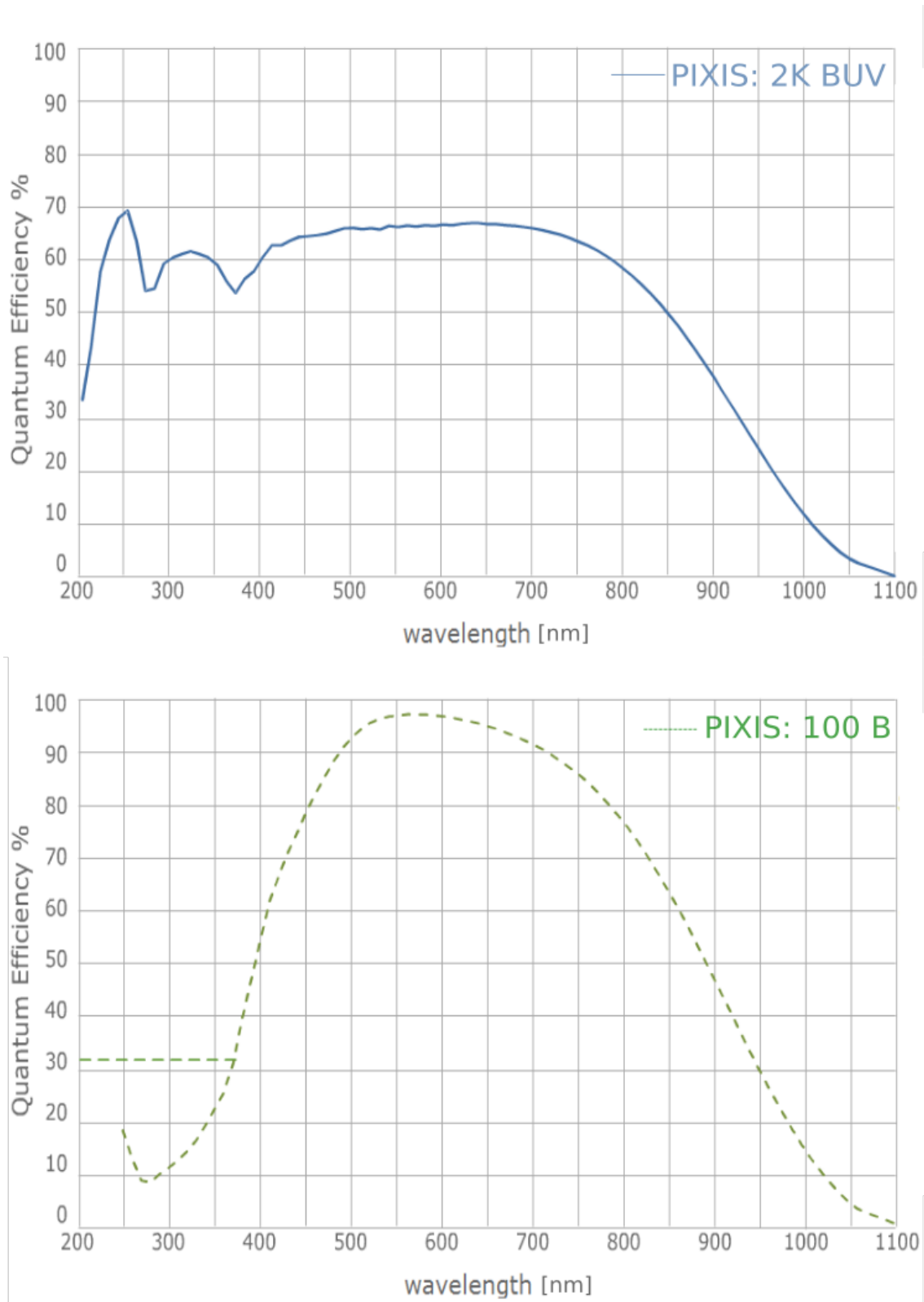


Figure 5.8: Quantum efficiency curves of the UV (2K BUV) and the visible detector (100 B). For the 2K BUV the QE peak is 67% at 250 nm. For the 100 B the QE peak is 95% at 550 nm.

[<http://www.princetoninstruments.com/products/speccam/pixis/dsheet.aspx>]

Front- and back illuminated CCDs

Depending on how the layers of the CCD chips are positioned towards incident light one differentiates between back- and front-illuminated CCDs. Figure 5.9 shows a sketch of the set-up of a front- and a back illuminated CCD unit. In a front illuminated CCD the incident light first hits the upper side of the silicon disc where the semiconductor structures have been doped. On this upper side the non-photosensitive layers of the CCD unit, the insulating silicon dioxide layer and the polysilicon gates are located. Hence some of the incident photons, especially those with short wavelengths will already be absorbed in this layer before they reach the photosensitive part. For applications where high light sensitivity especially for short wavelengths is required, back illuminated CCDs are used. For these, the silicon wafer is turned and the back side is thinned out by grinding and etching. The CCD chip is then positioned with the backside first exposed to the light.

The usage of a back illuminated CCD chip can thus increase the QE of the detector significantly. For example the QE of the back illuminated detector used in the visible region (PIXIS 100 B) has a QE peak of 95%. In comparison the equivalent model using a front illuminated CCD chip (PIXIS 100 F) has only a QE peak of 47%.

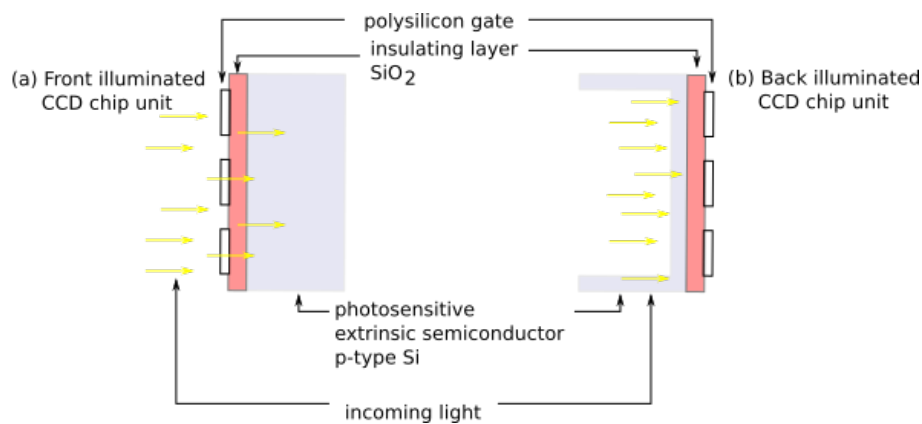


Figure 5.9: Sketch of a Back- and a Front-illuminated CCD chip unit. In (a) the incident photons first pass the not photosensitive polysilicon gate and the insulating layer before they reach the photosensitive layer. Especially short wavelengths can already be absorbed before they reach the photosensitive layer. In a back illuminated CCD chip the silicon wafer is turned so that the thinned photosensitive p-doped Si layer is first exposed to the incident photons.

Dark current

Dark current describes the spontaneous formation of electric charges in the photo-sensitive semiconductor layer of the CCD due to heat.

Following the third law of thermodynamics the molecules and atoms forming the semiconductor move. This thermal movement is increasing with temperature T . Due to thermal movement inelastic shocks can occur. These can lead to release of electric charges in the semiconductor (thermal excitation) without any incident light. The dark current varies following a Poisson distribution. The noise resulting from this variation is called dark noise:

$$\sigma_{\text{dark}} = \sqrt{e_{\text{dark}}} \quad (5.8)$$

where e_{dark} is the number of thermally generated electrons within the exposure time.

The dark current can be different for every single pixel in the CCD. Pixels with an extremely high dark current are called 'hot pixels'. They are recognisable as bright spots in the CCD image and should be excluded from the signal evaluation. (Demtröder, 2008)

To reduce dark current and noise modern CCD detectors are cooled down using thermoelectric cooling devices, typically below -45°C .

Readout noise

Readout noise is the noise produced by the output amplifier and other sources of noise before the signal is digitalised by the ADC. For the spectrometers in use the readout noise is typically 11 to 14 electron charges at 2 MHz.

Shot noise

Shot noise is caused by the fact that the arrival of photons is a stochastic process that is governed by a Poisson distribution. Therefore the shot noise $\sigma_{\text{shot noise}}$ is proportional to the measured signal intensity I_{signal} with:

$$\sigma_{\text{shot noise}} = \sqrt{I_{\text{signal}}}. \quad (5.9)$$

(Demtröder, 2008)

Electronic offset

To ensure that the ADC always receives a positive signal the CCD artificially induces an electronic offset also referred to as *bias level*. If the data values are to be truly representative of the counts recorded per pixel this offset has to be removed from the CCD data.

Detector linearity

Ideally the relation between quantity of light, quantity of charge and output signal is linear. This is especially important for DOAS applications since one assumes in the DOAS fit, that instrumental effects are varying linear and thus cancel out by division with the reference spectrum.

Blooming effects

When a pixel is overexposed and more charges are produced than can be processed it can happen, that charges convert to adjacent pixels. This effect is called blooming. Starting with the central overexposed pixel adjacent pixels also show higher signals. An area of higher signal 'blooms' around the overexposed pixel.

5.5 Software for Evaluation and Modelling

In the following the software used for the evaluation and the modelling software SCIATRAN shall be described shortly.

5.5.1 Software for Data Evaluation

To derive slant column densities from the measured spectra several software tools have to be used. The data processing can be divided into three steps: data record, data preparation and data fit:

- **Data record:** The measured spectra are recorded using the measurement software AMAX_ OMA in counts per pixel.
- **Data preparation:** To convert the pixel number into a wavelength the software NKALIB is used, where a line lamp spectrum is taken into account for

calibration. The program NKALIB works together with the program NPREPARE which rejects spectra that show very low dynamic range (performed under bad light conditions) and spectra that were affected by high energetic cosmic radiation. To calculate the spectral resolution the program RESOLUT is used. Using line lamp measurements it determines the spectrometer's slit function which is later convoluted with the absorption cross section to account for the optical resolution of the instrument.

- **DOAS fit:** The prepared spectra are fitted using the software NLIN_D. It delivers the fitted slant column densities as well as the residuals of the fit.

5.5.2 SCIATRAN

SCIATRAN is a software package incorporating a radiative transfer model and a retrieval algorithm. It has been developed at the IUP of the University of Bremen. It includes several features:

- Scalar or polarized transfer modelling of radiance/intensity, weighting functions, air mass factors (AMF), slant columns, vertically resolved AMFs (block AMFs), fluxes (actinic, upwelling, downwelling, diffuse and total), spherical albedo and vertical/slant optical depth.
- Any observation geometry and position of the instrument can be specified (space, ground, atmosphere).
- Atmospheric modelling of trace gases (O_3 , NO_2 , ClO , $OCIO$, BrO , H_2CO , SO_2 , NO_3 , O_4 , O_2 , H_2O , CO_2 , CO , CH_4 , and N_2O), clouds and aerosols.
- Simulation of inelastic scattering processes (rotational and vibrational Raman scattering)

A detailed description of SCIATRAN is given by V.V.Rozanov and A.V.Rozanov (2013).

6 Calibration of the DOAS-System

Every DOAS system has its own characteristics depending on its particular components. Within the scope of this thesis a new MAX-DOAS system has been installed. The characterisation of the entire system consists of the characterisation of every single component. Therefore the detector and spectrometer used for the DOAS system have to be characterised and - where possible - compared to manufacturer's settings. Knowing the properties of detector and spectrometer the operational settings for the retrieval of the trace gases of interest e.g. NO_2 can be optimized.

In the following chapter the calibration measurements performed for the characterisation of the CCD-detectors and the resolution of the spectrometers are presented.

6.1 Characterisation of the CCD-Detectors

The CCD-detector is an essential element in the DOAS system. For the DOAS technique, two properties of the CCD detector are essential: the dark signal and the linearity of the detector. The dark signal is the signal the CCD produces without any incoming light. It consists of the dark current, the readout noise and the electric offset of the detector. These properties have already been introduced in section 5.4.

For DOAS applications the dark current should be an offset constant over a wide range of exposure times and the noise of the detector should be adequately small. The linearity of the detector is the second property essential for DOAS measurements. A linear detector signal means that ideally the signal increases linearly with integration time, so that a measurement with double exposure time equals double quantity of light. This corresponds to a slope of 1. In the following the calibration measurements for dark current and linearity of the detector are presented.

6.1.1 Dark Current Measurements

An ideal compromise between dark current, noise and linearity of the dark signal over different exposure times is desirable. To analyse these properties for both CCD detectors dark signals for different detector temperatures and typical exposure times have been measured. The detector temperature was increased in 5°C steps starting at -60°C until -5°C. Exposure times were 0.025 s, 0.05 s, 0.1 s, 0.2 s, 0.4 s, 0.8 s, 1.6 s, 3.2 s, 6.4 s, 12.8 s and 25.6 s. For each exposure time and temperature 10 measurements have been averaged.

To analyse the dark signal, the mean number of counts was calculated. The corresponding standard deviation of the mean is proportional to the total noise.

Figure 6.1 shows the mean dark signal for all recorded temperatures and exposure times for the UV (top) and the visible CCD detector (bottom). Below -45°C, for both detectors no significant exposure time dependence of the mean signal is observed. The electronic offset seems to be larger for lower detector temperatures. For temperatures larger than -45°C, the mean signal increases with increasing exposure time. The higher the detector temperature, the faster is the increase of the mean dark signal with exposure time. This is the case for both detectors.

The standard deviation of the mean dark signal is shown in figure 6.2. The standard deviation stays close to zero for all exposure times for detector temperatures $\leq -45^\circ\text{C}$. For higher temperatures, the standard deviation starts to increase with exposure time.

Hence for detector temperatures higher than -45°C the total noise of the system starts to increase and the mean dark signal shows dependency of the exposure time. The detector temperature was therefore set to -45°C , so that dark noise can be neglected and the offset stays constant for different exposure times.

Because of the observed dark-offset of the detector it is necessary to perform dark measurements to subtract the dark counts from the counts of the measured spectrum. Only then the measured values are truly representative for the incoming intensity. In the measurement software AMAX_ OMA nightly automatic dark measurements can be activated.

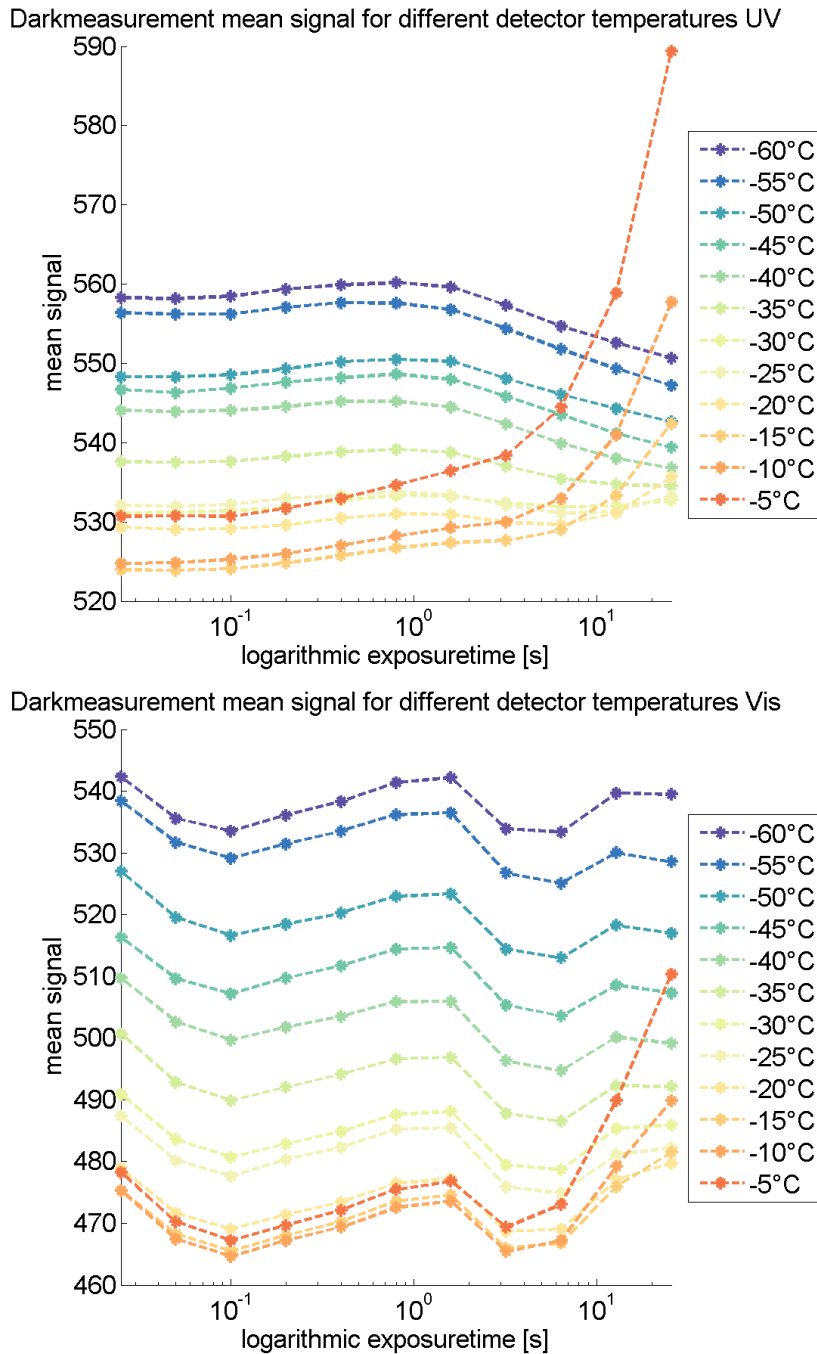


Figure 6.1: Mean counts of the dark spectrum measured for different exposure times and detector temperatures plotted on a logarithmic time scale. Top: Results for the detector used with the UV spectrometer. Bottom: Results for the detector used with the visible spectrometer. For the UV detector the mean dark signal remains constant for detector temperatures $\leq -45^\circ\text{C}$, for the visible detector this is the case for detector temperatures $\leq -40^\circ\text{C}$.

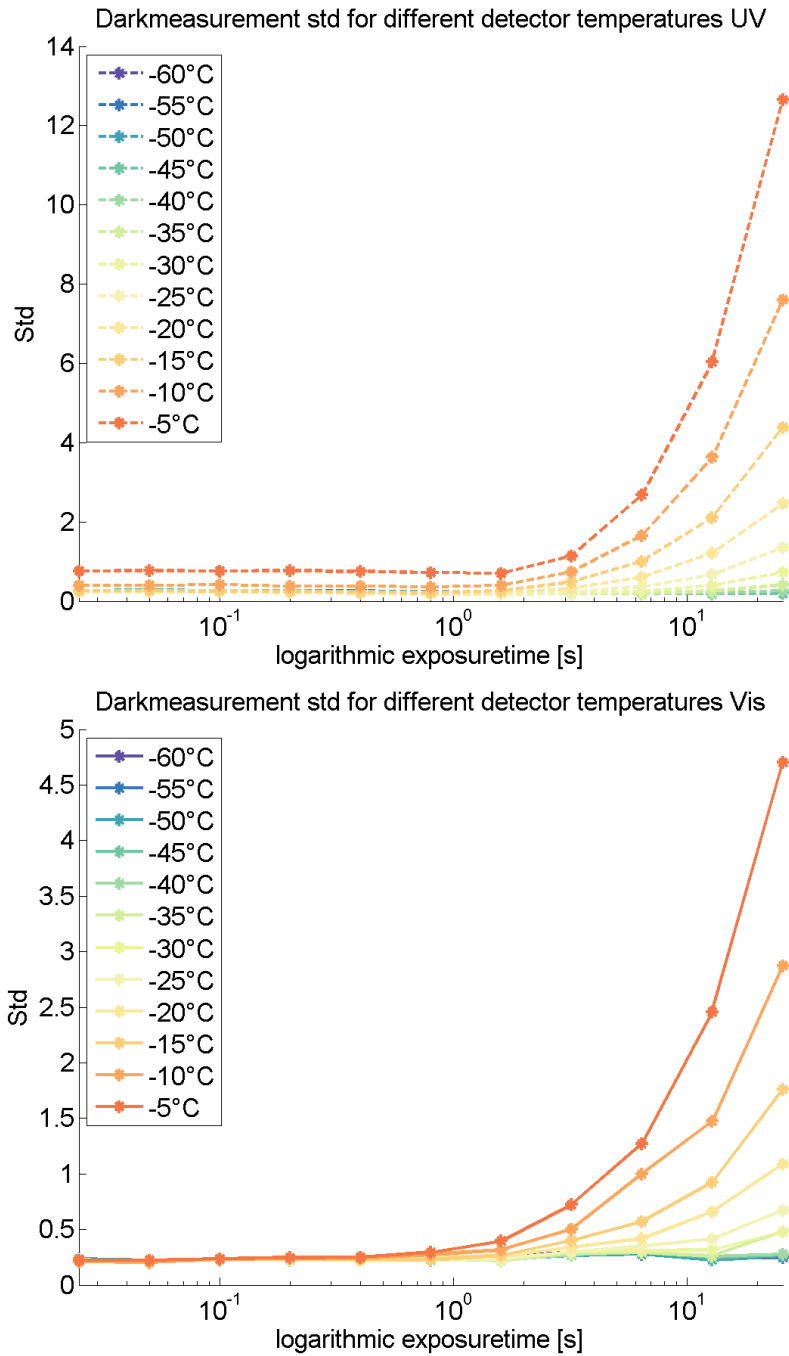


Figure 6.2: Standard deviation of the mean counts of the dark spectrum measured for different exposure times and detector temperatures plotted on a logarithmic time scale. Top: Results for the detector used with the UV spectrometer. Bottom: Results for the detector used with the visible spectrometer. For both detectors the standard deviation remains close to zero for detector temperatures $\leq -45^\circ\text{C}$. For higher temperatures the standard deviation starts to increase with exposure time. This is more pronounced the higher the detection temperature.

6.1.2 Linearity Measurements

For DOAS applications a linearity of the detector is crucial. Only for a linear detector signal, instrumental effects cancel out in the DOAS fit by dividing the recorded spectrum by a reference spectrum.

The linearity measurements in the visible and UV have been performed by recording spectra of a white lamp.

The image of the white lamp spectrum on the CCD makes it possible to identify hot and dead pixels on the CCD:

- Hot pixels show always higher signals than their neighbours. In a dark spectrum they can also be recognised as bright spots.
- Dead pixels are always dark, independent of the incoming light intensity. In a white lamp spectrum they are visible as dark spots.

The identified dead pixels were recorded and excluded in AMAX_ OMA.

The white lamp shows only small intensities in the UV. Therefore for the linearity measurements with the UV detector in addition measurements with a line lamp have been performed. The set-up for these measurements was the following:

- **White lamp measurements:** The light fibre was removed from the spectrometer's entrance slit. A white Teflon paper was fixed in front of the entrance slit for illumination uniformity. After every measurement a reference spectrum with a fixed exposure time of 1 s has been recorded to account for drifts of the light source.
- **Line lamp measurements:** Line lamp measurements were performed using the HgCd line lamp installed in the telescope box. A reference spectrum with an exposure time of 1 s has been performed before and after the measurement to check the drift during the measurement period.

Both detectors provide different gain modes: the High Capacity (HighCap) mode with larger gains for light intensive applications and the Low Noise (LowNoise) mode for applications with only small light signal with smaller gains (see section 5.4). An overview of the measurement settings for both detector modes is given in table 6.1

for the white lamp measurements and in table 6.2 for the line lamp measurements. For each exposure time the spectrum has been averaged using 10 measurements. The highest exposure time was limited by saturation effects. When single pixels were overexposed (recognisable by blooming effects) the exposure time was reduced. Because the white lamp shows only low intensities in the UV, the measurements have been performed with large exposure times starting from 1 s up to 51 s.

Detector-mode	Readout	Amplifier	Vertical binning	Exposure times (step size) [s]
HighCap	2MHz	2	1	UV:1.0-51.0(10.0) visible: 0.1-1.0 (0.1) & 1.0-10.5 (0.5)
LowNoise	2MHz	2	1	UV:1.0-51.0(10.0) visible: 0.1-1.0 (0.1) & 1.0-4.5 (0.5)

Table 6.1: Detector settings and exposure times chosen for the white lamp measurements in UV and visible.

Detector-mode	Readout	Amplifier	Vertical binning	Exposure times (step size) [s]
HighCap	2MHz	2	1	UV:0.5-15.0(0.5)
LowNoise	2MHz	2	1	UV:0.5-25.0(0.5)

Table 6.2: Detector settings and exposure times chosen for the line lamp measurements in the UV.

The dark signal corrected spectra were evaluated by determining the maximum counts of the spectra recorded with different exposure times. For the line lamp measurements the maximum of the 326 nm Cadmium peak was used.

To investigate the linearity of the signal, the ratio of measurements recorded with different exposure times towards the highest exposure time was plotted and a linear

fit was performed. Ideal linearity would correspond to a slope of 1.

In addition, the coefficient of determination of the linear fit R^2 has been calculated:

$$R^2 = 1 - \frac{\left(\sum_{i=1}^N y_i - \hat{y}_i\right)^2}{\left(\sum_{i=1}^N y_i - \bar{y}\right)^2} \quad (6.1)$$

where \hat{y} is the calculated value of y and \bar{y} is the mean value of y . R^2 falls between 0 and 1 and is a measure of how well the linear model fits the data.¹

Figure 6.3 shows the linearity plots for the white lamp and line lamp measurements for both detector modes in the UV.

For the white lamp measurements the fitted nonlinearity is very low:

- For the HighCap mode shown in figure 6.3 (a) the nonlinearity is 0.8%.
- For the LowNoise mode shown in figure 6.3 (b) it is 0.7%.

These values fall significantly below the nonlinearity guaranteed by the manufacturer of $\leq 2\%$ for 2 MHz read out.

The nonlinearity in the linear fits obtained by the line lamp measurements in the UV are higher than the ones obtained by the white lamp measurements, they still fall below the nonlinearity guaranteed by the manufacturer:

- For the HighCap mode shown in figure 6.3 (c) the nonlinearity is 1.6%
- For the LowNoise mode shown in figure 6.3 (d) it is 1.9%.

The coefficient of determination R^2 is ≥ 0.99989 for all performed linear fits in the UV. This excellent value for R^2 underlines the good linearity properties of the detector. The linearity plots resulting from the white lamp measurements with the visible CCD detector are shown in figure 6.4. The observed nonlinearities fall again clearly below the nonlinearity limit guaranteed by the manufacturer of $\leq 2\%$ for 2 MHz read out:

- For the HighCap mode shown in figure 6.4 (a) the nonlinearity is $< 0.5\%$
- For the LowNoise mode shown in figure 6.4 (b) the nonlinearity is 1.3%

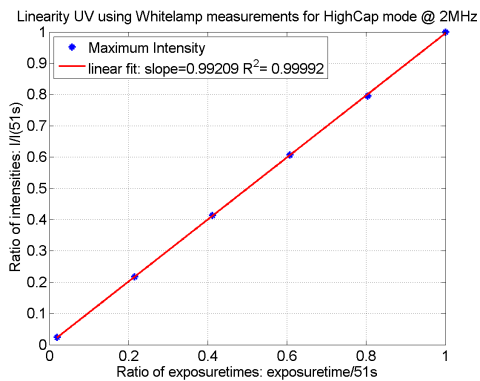
The coefficient of determination R^2 indicates with a value ≤ 0.99994 an excellent linearity of the detector. Considering the results of the linearity measurements the best detection mode of choice for the visible detector is the HighCap mode. The nonlinearity of the detector in this mode is much smaller than the one calculated for the LowNoise mode. In addition single pixels of the CCD show saturation effects for much lower exposure times in the LowNoise mode than for the HighCap mode.

In contrast for the UV detector the LowNoise mode seems to be the right choice. While the HighCap mode is designed for measurements with high intensity and therefore the ideal choice for the visible, the LowNoise mode is the better choice for the UV, since the intensity of UV light on the Earth's surface is much lower than the one in the visible region. For the white lamp measurements in the UV the nonlinearity in the HighCap mode is slightly higher than in the LowNoise mode.

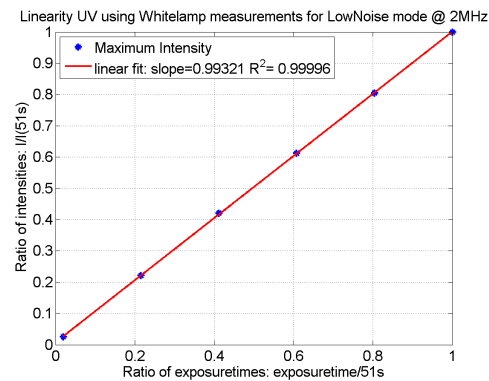
Another parameter that can be set in the detector settings is the vertical binning. This is the number of pixels that is binned before the signal is read out by the detector. For the linearity measurements vertical binning has been set to 1. This is not the ideal setting for DOAS measurements, since single pixels are already saturated at relatively small exposure times, e.g. 4.5 s for the Low Noise mode for the visible detector.

To use most of the highest possible read out capacity (≈ 64000 counts) without saturation of single pixels (i.e. avoiding blooming effects), vertical binning should be set to 4.

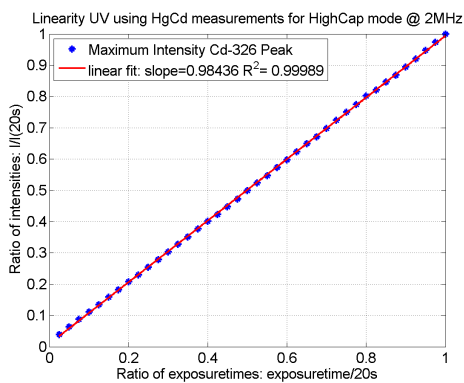
¹[\[http://de.mathworks.com/help/matlab/data_analysis/linear-regression.html\]](http://de.mathworks.com/help/matlab/data_analysis/linear-regression.html)



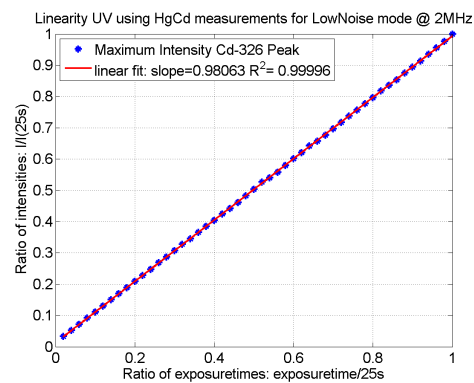
(a) Linearity plot of UV detector in HighCap mode using white lamp measurements. The resulting nonlinearity is smaller than 0.8%.



(b) Linearity plot of UV detector in LowNoise mode using white lamp measurements. The resulting nonlinearity is smaller than 0.7%.

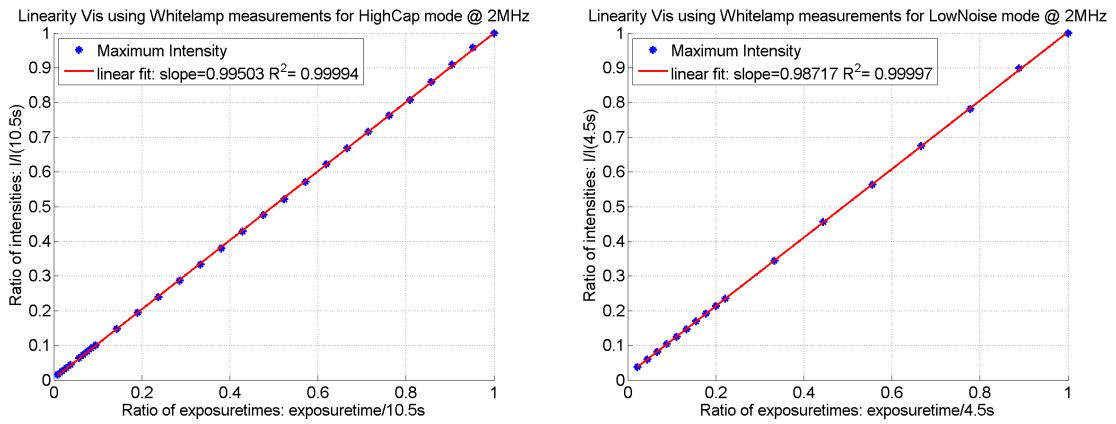


(c) Linearity plot of UV detector in HighCap mode using line lamp measurements. The resulting nonlinearity is 1.6%.



(d) Linearity plot of UV detector in LowNoise mode using line lamp measurements. The resulting nonlinearity is 1.9%.

Figure 6.3: Linearity plots for the UV detector for both available detector modes. The nonlinearity limit of 2% guaranteed by the manufacturer is never crossed.



(a) Linearity plot of visible detector in High-Cap mode using white lamp measurements. The resulting nonlinearity is smaller than 0.5%. (b) Linearity plot of visible detector in LowNoise mode using white lamp measurements. The resulting nonlinearity is 1.3%.

Figure 6.4: Linearity plots for the visible detector for both available detector modes. For both detector settings the nonlinearity falls significantly below the limit of 2% guaranteed by the manufacturer.

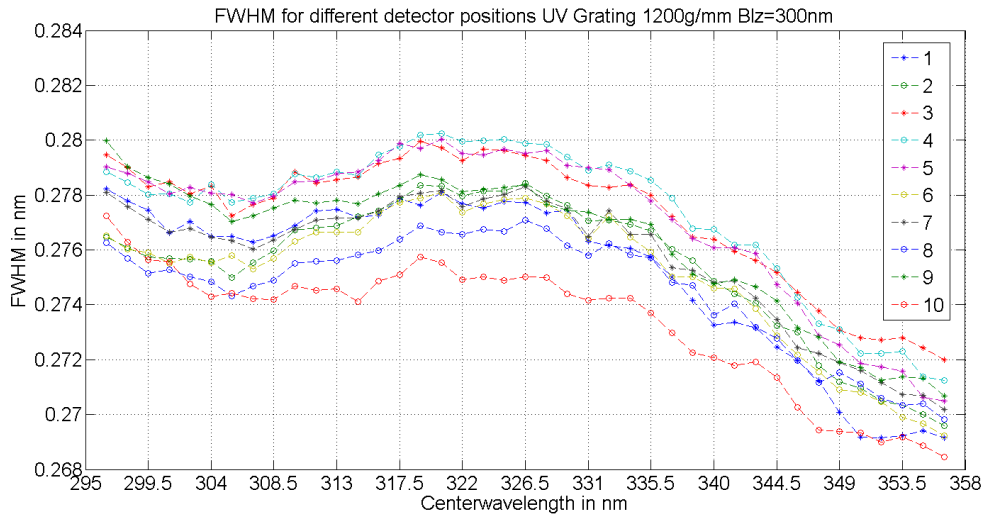
6.2 Slit Function Measurements

The spectral resolution is determined by the dispersion of the spectrometer. It depends on the width of the entrance slit, the focal length and the grating characteristics of the spectrometer (see section 5.3). One way to measure the resolution of the system is to measure the full width at half maximum (FWHM) of the so called slit function. The slit function is the image of the monochromatic illuminated entrance slit on the CCD. The aim of the measurements described in this chapter is to establish the effective slit function of the system as function of wavelength and position on the CCD chip.

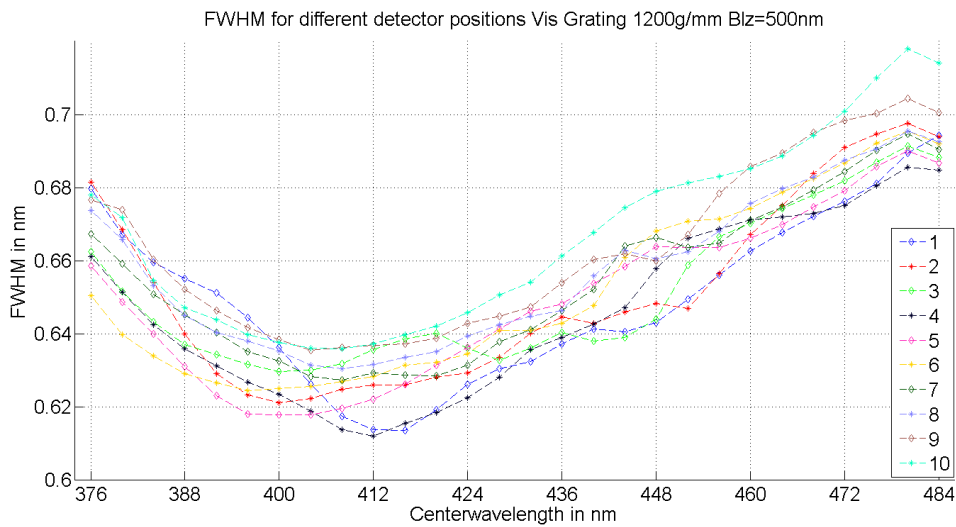
Therefore the entrance slit is illuminated using the HgCd line lamp integrated in the telescope box. For measurements in the UV the slit function of the Cd-340 peak was analysed. For measurements in the visible the Hg-435 peak was used. To observe the slit function at different CCD and grating positions multiple measurements were performed:

- For each measurement the center wavelength of the spectrometer was changed, so that the peak was not passing more than 50 pixels on the CCD.
- Vertical binning was set to 10, in order to observe the FWHM for 10 equal spaced vertical areas on the CCD chip separately.

The FWHM of the corresponding slit function was determined by fitting a Gaussian on the peak and calculating the FWHM using the fit results. The resulting resolutions of the 1200 g/mm gratings for the UV and visible spectrometer are shown in figure 6.5 (a) and (b). The FWHM of the UV grid only varies between 0.02 nm for all observed center wavelengths and vertical positions. This implicates excellent spacial agreement of the resolution which was expected for an imaging spectrometer with zero astigmatism. The FWHM of the visible spectrometer varies more for different positions of grating and on the CCD, approximately about 0.1 nm. This is by far not as good as the performance of the UV spectrometer. This was expected taking into account that it is not an imaging spectrometer and shows astigmatism of $690\mu\text{m}$. This is acceptable for the later usage when the measurements are binned vertically over the whole CCD chip.



(a) Fitted full width half maximum in nm for the UV spectrometer using the Cd-340 peak of the HgCd line lamp measurements. The 10 curves correspond to 10 equal spaced vertical areas on the CCD chip. For the different center wavelengths corresponding to different horizontal positions on the CCD and the observed 10 vertical areas the FWHM of the Cd-340 line does not vary more than 0.02 nm. In average the FWHM is 0.269 ± 0.002 nm.



(b) Fitted full width half maximum in nm for the visible spectrometer using the Hg-435 peak of the HgCd line lamp measurements. The 10 curves correspond to 10 equal spaced vertical areas on the CCD chip. For the different center wavelengths corresponding to different horizontal positions on the CCD and the observed 10 vertical areas the FWHM of the Hg-435 line does vary in a 0.1 nm range. In average the FWHM is 0.65 ± 0.01 nm.

Figure 6.5: Profile of the FWHM for 10 equal spaced vertical positions and different center wavelengths UV and visible.

The resolution of all gratings available for each spectrometer was determined in the same way described for the 1200 g/mm gratings only that vertical binning has been set to one so that the measured spectra were binned vertically over the entire CCD chip.

The UV spectrometer provides three gratings: the 1200 g/mm, the 600 g/mm and the 300 g/mm grating.

For the visible spectrometer a 1200 g/mm and a 600 g/mm grating are available.

Figure 6.6 shows the resulting FWHM for the two different spectrometers and all available gratings as function of center wavelength. The errorbars are determined by the accuracy of the Gaussian fit. Table 6.3 and 6.4 summarise the resolution characteristics for the UV and visible systems for the different gratings.

The resolution is given by the mean FWHM for all observed center wavelengths and detector positions. The associated error is the standard deviation of the mean.

The resolution in dependence of center wavelength of the UV spectrometer is shown in figure 6.6 (a). The mean resolution was observed for all gratings of the UV spectrometer:

- For the 1200 g/mm grating the mean resolution is 0.269 ± 0.002 nm.
- For the 600 g/mm grating the mean resolution is 0.55 ± 0.01 nm. With a maximum deviation of 0.015 nm of FWHM for all observed center wavelengths the 600 g/mm grating shows excellent spacial agreement of the measured FWHM for the different horizontal positions on the CCD.
- The 300 g/mm grating shows the lowest mean resolution of 1.28 ± 0.02 nm and varies by maximal 0.06 nm for the different center wavelengths. This resolution is worse than theoretically expected factor 2 by equation 5.6 towards the 600 g/mm grating. Nevertheless, the spectral resolution is consistent for all observed center wavelengths.

For the visible spectrometer the mean resolution was determined for both available gratings:

- For the 1200 g/mm grating the mean resolution is 0.65 ± 0.01 nm.
- For the 600 g/mm grating the mean resolution is 1.5 ± 0.3 nm. This resolution doesn't reach the theoretically expected factor 2 by equation 5.6 towards the

1200 g/mm grating. The resolution increases by 0.6 nm from the lowest to the highest observed center wavelength. This can result from the change of the grating's position for different center wavelengths. It can also be a result of the different positions of the peak on the CCD, but since the 1200 g/mm grating does not show an increase of this quality for the different horizontal positions on the CCD it is expected that the position change of the grating for the different center wavelengths is responsible for the increase of FWHM.

Grating [g/mm]	Center wavelength range [nm]	Resolution [nm] (FWHM of slit function)
1200	295 - 358	0.269±0.002
600	285 - 402	0.55±0.01
300	215 - 452	1.28±0.02

Table 6.3: Characteristics of the spectrometer used in the UV range for different gratings

Grating [g/mm]	Center wavelength range [nm]	Resolution [nm] (FWHM of slit function)
1200	376 - 484	0.65±0.01
600	310 - 537	1.5±0.3

Table 6.4: Characteristics of the spectrometer used in the visible range for different gratings

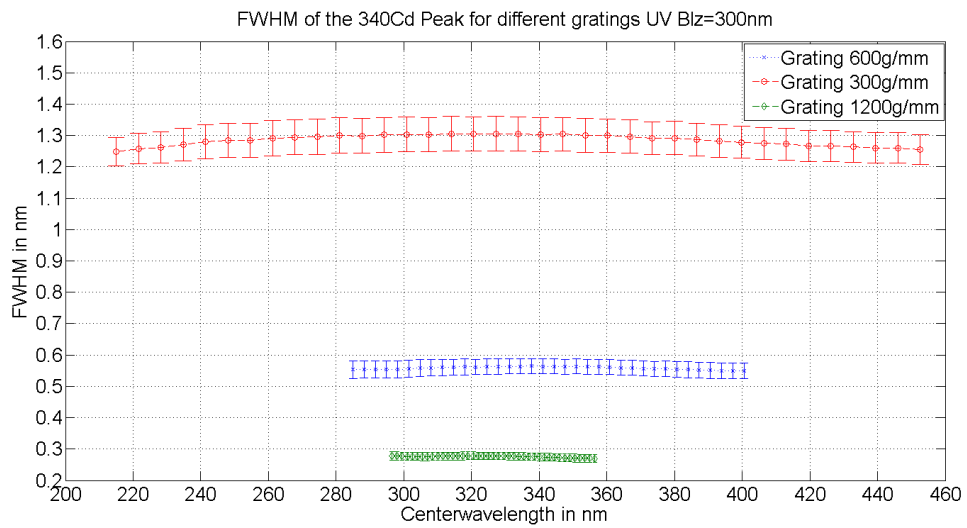
Conclusions for the grating of choice

For the visible spectrometer the 1200 g/mm grating is the most suitable for DOAS applications. With a resolution of 0.65±0.01 nm it is perfectly suited for the retrieval of trace gases like NO₂ that do not show too narrow-band structures.

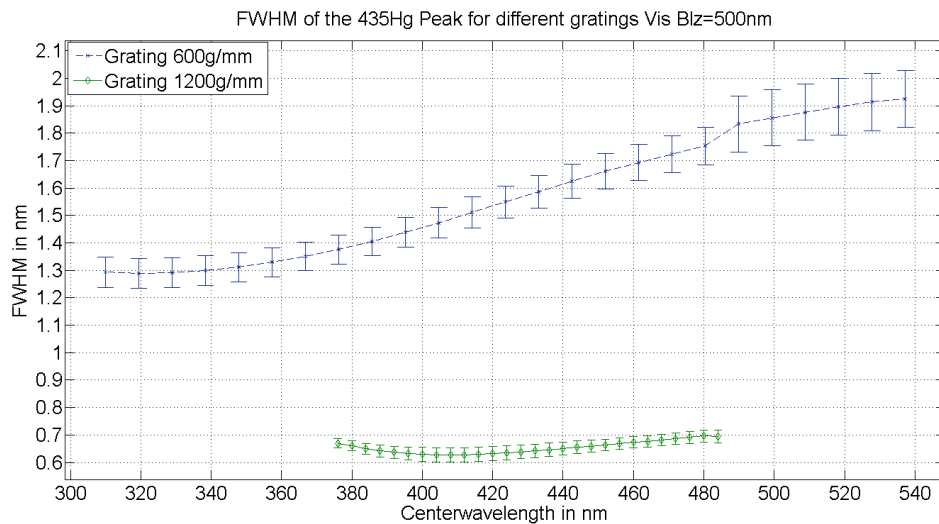
For the UV spectrometer the 1200 g/mm and the 600 g/mm grating can be considered depending on the favoured application. The 1200 g/mm grating is with its

excellent resolution the ideal choice for the retrieval of trace gases with very narrow-band structures like SO_2 that require resolutions in this dimension (see absorption cross-sections in figure 3.4).

For the retrieval of trace gases like NO_2 that do not require this high resolutions the 600 g/mm grating is interesting, since with the decrease of lines per mm by a factor of 2 also the spectral range is twice as high than for the 1200 g/mm spectrometer. This offers more possibilities e.g. for the choice of fitting windows.



(a) Effective slit function of the UV spectrometer for all available gratings.



(b) Effective slit function of the visible spectrometer for both available gratings.

Figure 6.6: FWHM for all available gratings in UV and visible spectrometer. The errorbars are resulting from the fitting errors of the Gaussian fit to determine the FWHM.

7 Intercomparison of MAX-DOAS measurements of NO₂

After the calibration of the system was done and the corresponding operational settings were chosen it is necessary to check the overall performance of the new system in operation. Therefore, an intercomparison study with the Bremen MAX-DOAS system has been performed. The Bremen MAX-DOAS system is installed at the roof of the IUP building at University of Bremen. It is a two channel system, with a UV and a visible spectrometer and performs continuously measurements.

For the intercomparison study, differential slant column densities (SCD) of NO₂ measured by both MAX-DOAS systems in the UV and visible have been compared. From 3-15 April 2015, both systems were measuring in parallel on the roof of the IUP building. The telescope of the new system was installed pointing in one of the scanning directions of the Bremen instrument. In the following chapter the measurement site, the general settings for the intercomparison study and the results for the NO₂ SCD intercomparison are presented.

7.1 General Settings and Measurement Site

Both systems were operating in parallel on the roof of the IUP building of the University of Bremen. The chosen azimuthal viewing direction was pointing in direction of Bremen's waste-to-energy plant, which is located directly next to the highway A 27. The position of the IUP building and the azimuthal viewing direction are shown on a map in figure 7.1 (a). Two photographs from the video camera installed in each telescope box are shown in figure 7.1 (b). The photographs were taken at approximately 08 am UTC at the 13 April 2015. On both photographs, the waste-to-energy plant can be seen in the center.

Precipitation and cloud cover have strong influence on MAX-DOAS measurements

by a) directly influencing the atmospheric chemistry and the trace gas abundances due to washing out and wet deposition and by b) influencing the viewing conditions due to cloud cover.

Both MAX-DOAS systems are not operating perfectly synchronous, meaning that the systems are not looking in the same elevation at the same time. This short time shift can become relevant in the case of rapidly varying NO₂ concentrations and in the presence of clouds: The field of view of one instrument is covered by a cloud but when the second instrument is pointing in the same elevation, the cloud already disappeared from the field of view. This can be one reason why the two systems measure different SCDs of NO₂.

To eliminate this influence, in addition to an intercomparison of all measurements, only those measurements made in hours with no cloud cover have been taken into account. Cloud cover and precipitation measurements during the intercomparison period were taken from the Bremen weather station 690 of the German Weather Service (DWD)¹. Figure 7.2a shows the hourly cloud cover in Okta. The Okta scale is a unit of measurement used to describe the cloud cover. Cloud cover of 0 on the Okta scale corresponds to completely clear sky conditions, while cloud cover of 8 is equivalent to a completely cloudy sky. The meteorological symbol for each Okta is also shown in figure 7.2a. The daily precipitation in mm is shown in figure 7.2b.

The settings for the DOAS-Fit to retrieve the NO₂ SCDs are listed in table 7.1. The background spectrum was set to ZS-File-Sync. This setting selects the timely closest zenith spectrum before and after the measurement and takes their average as I₀ background spectrum for the DOAS-Fit.

¹Data accessible via: http://www.dwd.de/DE/klimaumwelt/cdc/cdc_node.html

Parameter	Settings UV	Remarks	Settings vis	Remarks
Spectral Range	338-350 nm	grating 1 (1200 g/mm)	425-497 nm	grating 1 (1200 g/mm)
Fitted Species	stratospheric O ₃	223 K (Gor-shelev et al., 2014)	stratospheric O ₃	223 K (Gor-shelev et al., 2014)
	tropospheric O ₃	243 K (Gor-shelev et al., 2014)		
	NO ₂	298 K (Van-daele and Hermans, 1996)	NO ₂	298 K (Van-daele and Hermans, 1996)
	O ₄	293 K (Thal-man and Volkamer, 2013)	O ₄	293 K (Thal-man and Volkamer, 2013)
			H ₂ O	293 K (Roth-man et al., 2009)
	H ₂ CO	297 K (Meller and Moort-gat, 2000)		
	Ring	Sciatran An-dreas Hilboll 21.10.2014	Ring	Sciatran An-dreas Hilboll 21.10.2014
Polynomial	5		4	
Reference (I ₀)	ZS-File-Sync			

Table 7.1: Settings chosen for MAX-DOAS-Fits in UV and visible

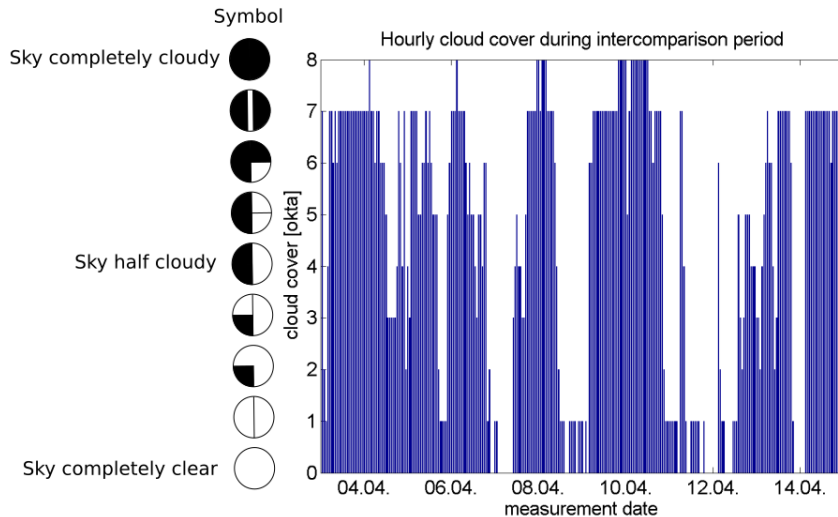


(a) Map of Bremen including the azimuthal viewing direction pointing from the IUP to the waste-to-energy plant Bremen.

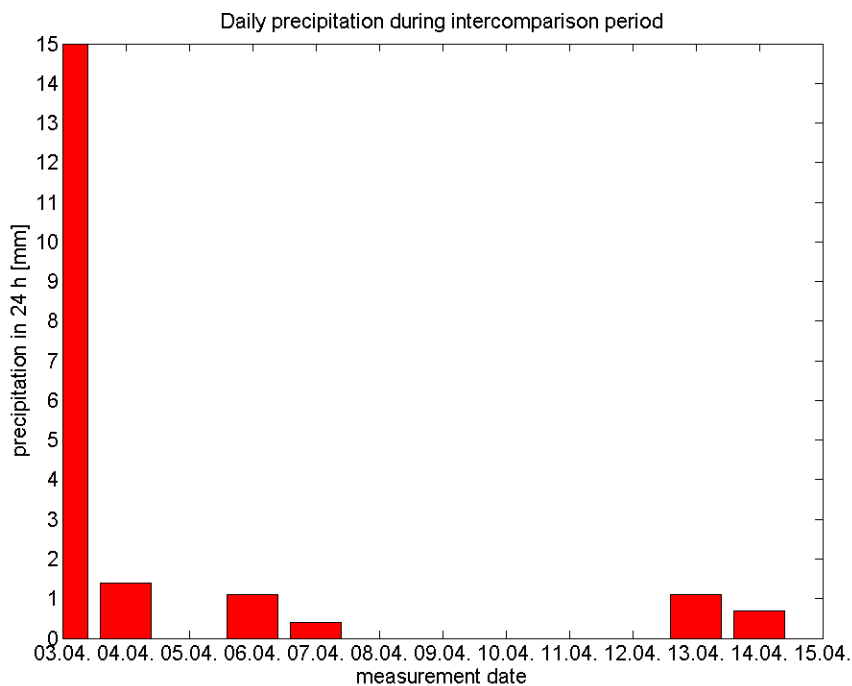


(b) Azimuthal viewing direction photographed by the camera in the telescope box of the new MAX-DOAS system. (c) Azimuthal viewing direction photographed by the camera in the telescope box of the MAX-DOAS Bremen system.

Figure 7.1: Azimuthal viewing direction of the MAX-DOAS systems on the roof of the IUP University of Bremen. Photographs taken at 13 April 2015 around 08 am UTC. Both systems are looking in the same direction, pointing at the waste-to-energy plant in the center of the picture. Both video cameras are of different type. Therefore they show a different image section. In addition the alignment of the video camera inside the telescope box can be slightly different. The field of view of the system is hence not automatically the center of the photograph.



(a) Hourly averaged cloud cover taken from the DWD weather data station 690 for the intercomparison period from 03-15 April 2015. The measure for the cloud cover is the Okta scale, reaching from 0 for completely clear sky to 8 for completely cloudy conditions. The meteorological symbols for the Okta scale are presented on the left hand side of the figure.



(b) 24 h rain fall in mm taken from the DWD weather data station 690 for the intercomparison period from 03-15 April 2015. During this time it rained on 6 days out of 13 days.

7.2 Intercomparison of NO₂ SCDs

Intercomparison of raw MAX-DOAS fit results of two instruments tend to be difficult if the measurements are not simultaneous. This can lead to relevant change of the measured NO₂ SCDs due to clouds and rapid changes of NO₂ concentration on a short time scale as mentioned above. Hence an averaging of the measured NO₂ SCDs in order to compare the results of both instruments seems reasonable. Figure 7.3 shows the NO₂ differential slant column densities (SCD) of the Bremen and the new instrument in comparison to the 30 minutes averaged data on 10 April. In the raw data different peaks for the Bremen and for the new system can be recognised, e.g. around 11:15 UTC. This can be linked to clouds covering the field of view of the new instrument, but not at the same time the one of the Bremen instrument. While the raw data shows two different peaks for the Bremen and the new instrument, the 30 minutes averaged data shows very small differences. Hence using 30 min averaged data is useful to reduce the influence of short events like clouds in the field of view or for low elevation angles rapid variance of NO₂ concentration.

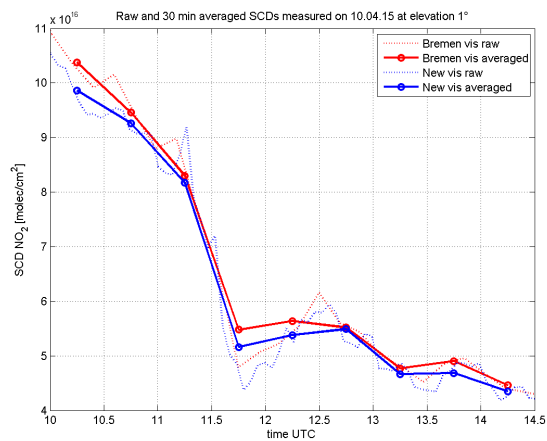


Figure 7.3: Comparison of raw and 30 min averaged SCDs of NO₂ measured by the Bremen and the new instrument at 10 April 2015 at an elevation angle of 1°. The raw data shows good correlation but single peaks differ, e.g. at 11:15 UTC. This peak could be caused by clouds in the field of view. The 30 min averaged data sets are not so sensitive to single peaks which are smoothed out. Therefore, the averaged data shows only small differences.

Correlation Coefficients

For the comparison of measurements from two different MAX-DOAS systems scatter plots are useful. In a scatter plot the measured NO₂ SCDs of the Bremen instrument are plotted on the x-axis, and the SCDs measured by the new instrument are plotted on the y-axis. In these scatter plots a linear relationship is expected. Therefore, the first aspect to check in the datasets is their linear correlation. The correlation coefficient of two variables is a measure of their linear dependence. For two variables A,B with N scalar observations the Pearson correlation coefficient is defined as the covariance of A and B, $\text{cov}(A, B)$, divided by the product of the standard deviations of A and B:

$$\rho(A, B) = \frac{\text{cov}(A, B)}{\sigma_A \cdot \sigma_B} = \frac{1}{N-1} \sum_{i=1}^N \left(\frac{A_i - \bar{A}}{\sigma_A} \right) \left(\frac{B_i - \bar{B}}{\sigma_B} \right). \quad (7.1)$$

\bar{A} and σ_A are the mean and the standard deviation of A and \bar{B} and σ_B are mean and standard deviation of B. The correlation coefficient has a value between 1 for perfect linear correlation and 0 if no linear correlation is found. ²

The correlation coefficients between the SCDs measured by the Bremen system and those measured by the new system were determined for all elevations.

In a first approach all measurements of the intercomparison period were considered. In a second approach only clear sky hours with a cloud cover of 0 okta were considered, the so called 'golden hours'.

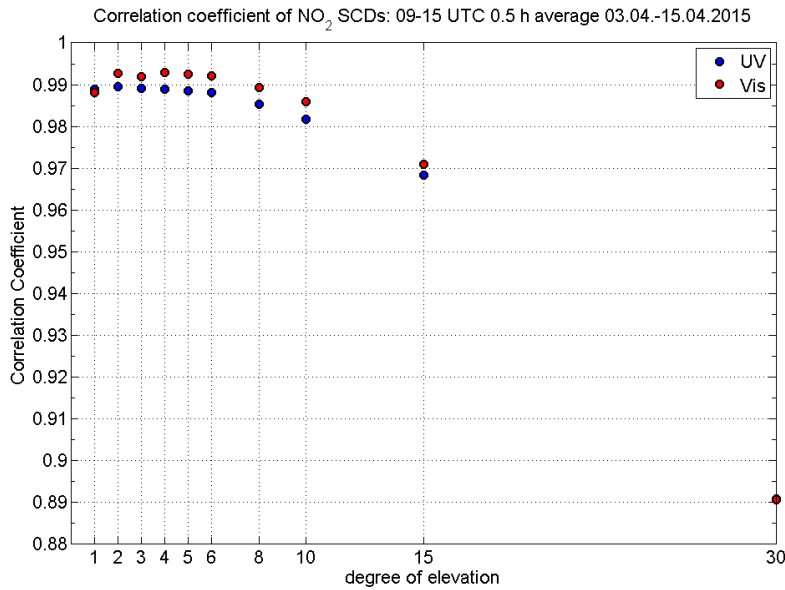
Figure 7.4 shows the correlation coefficients $\rho(\text{SCDs}_{\text{Bremen}}, \text{SCDs}_{\text{new}})$ calculated using equation 7.1 for all elevations and both approaches.

All data sets for UV and visible channel show excellent correlation:

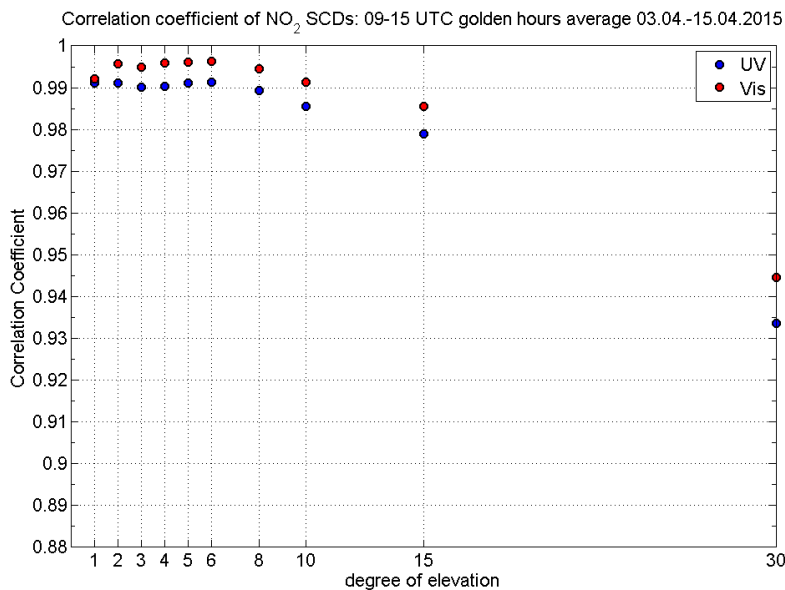
- The evaluation for all measurements in the intercomparison period shows a correlation of more than 0.89 for all elevations. The smallest correlation corresponds to the 30° data set.
- The correlation of the golden hours data showed an even better linear correlation of at least 0.93. The smallest correlation was again found in the 30° elevation.

²[\[http://de.mathworks.com/help/matlab/ref/corrcoef.html\]](http://de.mathworks.com/help/matlab/ref/corrcoef.html)

One explanation why the 30° elevation always shows the lowest correlation could be that the measured SCD of NO₂ decreases with elevation angle. For higher elevation angles, the light path in the lower troposphere gets shorter. Therefore, the measured SCD in 30° elevation is closer to the detection limit and the measurement errors increase. Nevertheless, the correlation is with ≤ 0.89 for all elevations very good.



- (a) Correlation coefficient considering all measured data points averaged on 0.5 hour intervals for each observed elevation angle. All data sets show distinct linear correlation better than 0.89.



- (b) Correlation coefficient considering only those hours, where the cloud cover was 0 okta. For each observed elevation angle the correlation coefficient is better than 0.93.

Figure 7.4: Correlation coefficients of NO₂ SCDs measured with the new and the Bremen MAX-DOAS system. The data sets show excellent linear correlation for all measured elevation angles.

Linear least-square fits

After the correlation analysis has been performed and the linear correlation is approved, a linear fit of the scatter plots can be used to gain more information about the agreement of the measured SCDs. If both systems provide the same value for the SCD of NO₂, a slope of 1 would be expected for a linear fit in the scatter plot. To perform linear fits, the least-square method has been used. The linear fits were of type

$$y = s \cdot x \quad (7.2)$$

where s is the slope of the linear relationship, y the NO₂ SCD measured with the new MAX-DOAS system and x the SCD measured with the Bremen system. To check whether an offset between the instruments exists, in addition linear fits allowing an intercept of i have been performed:

$$y = s \cdot x + i. \quad (7.3)$$

Linear fits with and without intercept have been performed. As a measure for the quality of the fit the coefficient of determination R^2 , given in equation 6.1 has been used.

Figure 7.5 shows the scatter plots for the UV and the visible spectrometer for all measurements (a) and for golden hours (b) using all elevation angles in one plot.

Figure 7.5 (a) shows the scatter plots for all measurements in the intercomparison period:

- The correlation coefficient is 0.989 in the UV and 0.993 in the visible.
- The linear fits with and without intercept show no significant differences:
 - In the UV the fit without intercept delivered a slope of 0.95. The fit that included an intercept fitted a slope of 0.94 and an intercept of $1.97 \cdot 10^{14}$.
 - In the visible the fit without intercept resulted with a slope of 0.92. The fit including an intercept fitted a slope of 0.91 and an intercept of $6.77 \cdot 10^{14}$.

For the scatter plots corresponding to the 'golden-hours' measurements shown in figure 7.5 (b) the situation looks similar:

- The correlation coefficient is 0.998 for the measurements in the UV and the visible.
- The linear fits with and without intercept are very similar:
 - In the UV the fit without intercept delivers a slope of 0.987. The fit including an intercept fits a slope of 0.97 and an intercept of $1.04 \cdot 10^{15}$.
 - In the visible the fitted slope without intercept is 0.924. The slope fitted with an intercept of $2.86 \cdot 10^{14}$ is 0.921.

These results indicate that there is no significant offset between the MAX-DOAS systems. Therefore in the following linear fitting is performed without an intercept. The fact that the correlation coefficient is higher for the 'golden hour' average than for all measurements shows that the data spread in the scatter plot is linked to cloud cover. The fitted slopes indicate a very good agreement of both systems:

- In the UV the fitted slope without intercept indicates that both system agree within 5% for all measurements. For the golden hours they even agree within 1.3%.
- In the visible the fitted slope without intercept for all measurements indicates an agreement of the systems within 8%. For the golden hours they agree within 7.6%.

The agreement in the UV is excellent. The disagreement between the visible instruments is higher, but still an acceptable result.

For further analysis, scatter plots and linear fits have been performed for each elevation separately. All half-hour averaged NO₂ SCDs and the golden hour averaged SCDs have been analysed by a linear fit without intercept. The resulting slopes as function of the elevation angle are shown in figure 7.6. The errorbars show the spread resulting from the coefficient of determination R^2 by $\sigma_s = s \cdot (1 - R^2)$. The interval of 5% deviation between the systems is indicated by the black dashed lines. The slopes resulting from all half-hour averaged NO₂ SCD measurements are shown in figure 7.6 (a):

- In the UV most of the fitted slopes are within the 5% deviation interval. Only for small elevation angles of 1° and 2° the fitted slopes are slightly beneath 0.95.

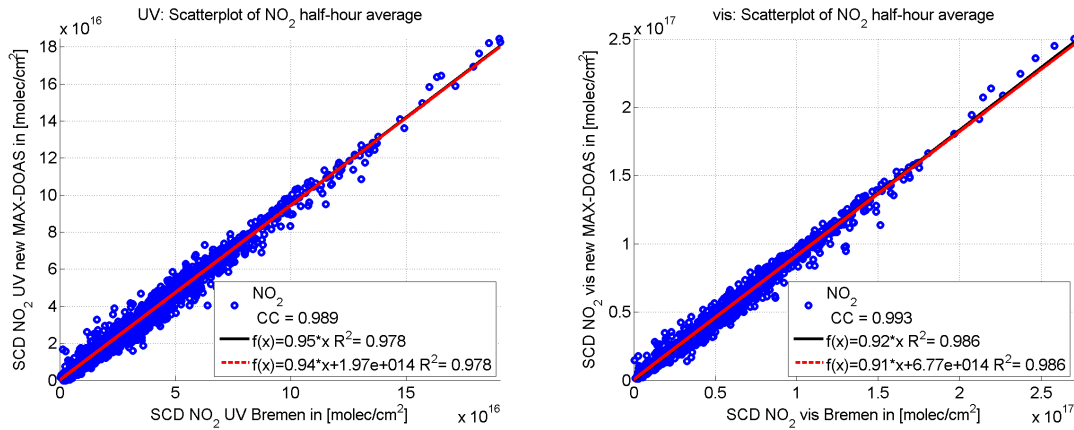
- In the visible the curve progression of slope as function of elevation angle is similar to the one in the UV, but the slope in the visible is always lower than the slope in the UV. Only slopes corresponding to elevation angles ≤ 8 are within the 5% interval.

The slope resulting from the golden hours linear fit is shown in figure 7.6 (b):

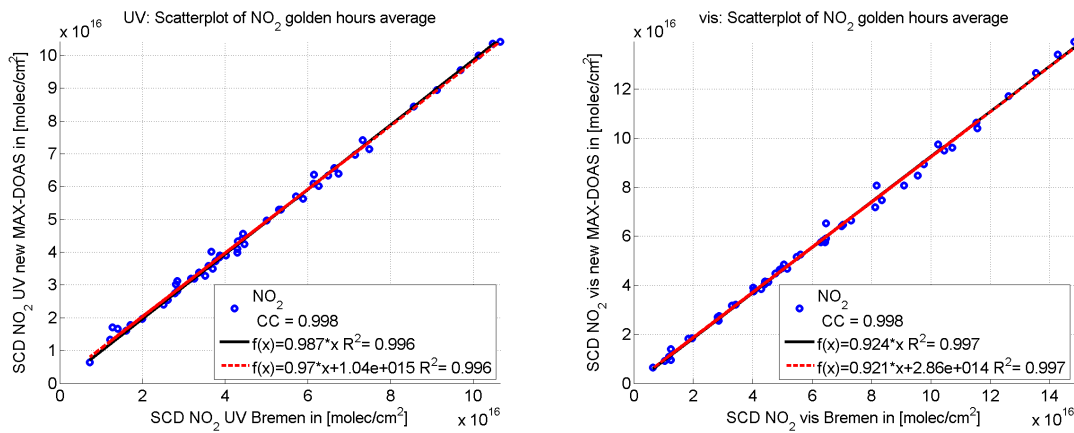
- In the UV all fitted slopes are within the 5% interval with exception from the 30° elevation.
- The slopes fitted in the visible stay slightly beneath the 5% interval for most elevations except for the 5° and 8° elevation. Nevertheless, the deviation of the systems is never larger than 9%.

The fact that the highest deviations between the systems are obtained at small elevation angles of 1° and 2° is a strong indication for a misalignment of the systems. Since measurements were performed close to an emission source smallest deviations of the field of view of the instruments can already lead to the observed disagreement of measured SCDs. An exact alignment of the instrument is very difficult because this has to be done manually. The video cameras integrated in the telescope boxes can only help for an approximate alignment because the field of view of the system is not equal to the field of view of the video camera.

Large intercomparison campaigns, (e.g. Roscoe et al. (2010)) show that even the best instruments of each institute taking part in the campaign show deviations in the order observed between the Bremen and the new MAX-DOAS instrument. The study performed by Roscoe et al. (2010) states that for visible MAX-DOAS instruments, the means of the fitted slopes for NO₂ of all except one instrument were within 10% of unity at almost all non-zenith elevations, and most were within 5%. For the UV the values were 12% and 7% respectively.

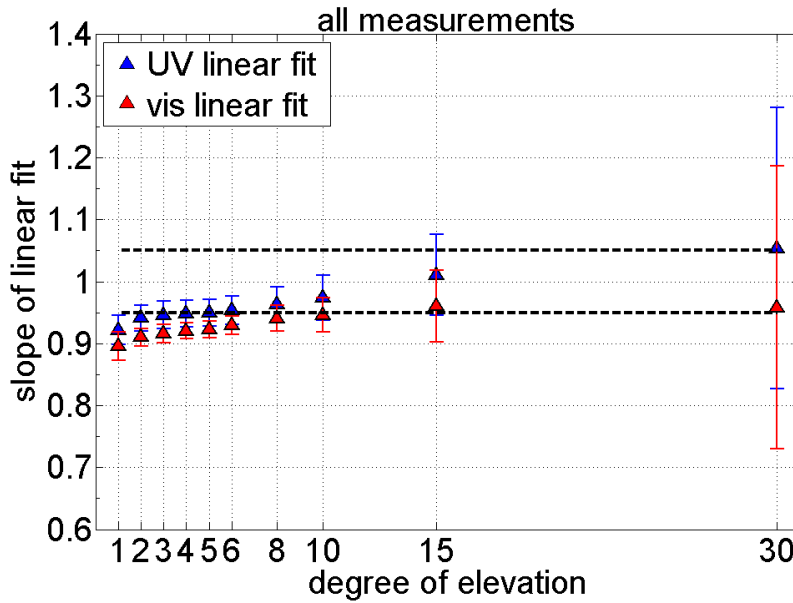


- (a) Scatterplot of measured SCDs of NO₂ in the UV and visible for the new MAX-DOAS system and the Bremen system. Between 09-15 UTC all half hour averaged data points are plotted from 03.04.-15.04.2015. The correlation coefficients for the UV and the visible data set are very good and show a maximum deviation of 0.011 from the ideal correlation 1. The difference between linear fit with and without intercept is very small.

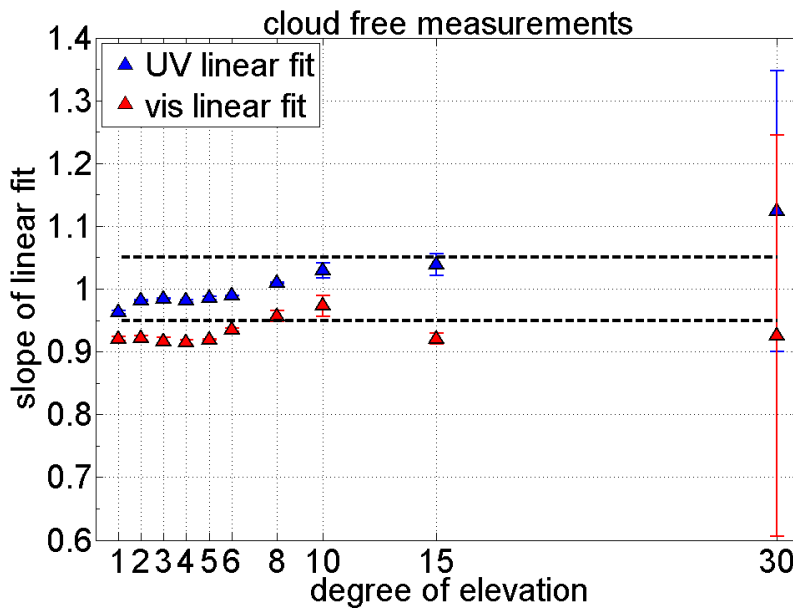


- (b) Scatterplot of measured SCDs of NO₂ in the UV and visible for the new MAX-DOAS system and the Bremen system. Between 09-15 UTC 03.04.-15.04.2015 all averaged golden hours are plotted. The data sets in UV and visible show excellent correlation with a deviation of only 0.002 from the ideal 1. The two applied linear fitting methods only differ minimal. The R^2 values are very close to 1 which means only very view scattering of the measured data points.

Figure 7.5: Scatter plots of NO₂ for UV and visible. For all plots only small variations between the two applied linear fits one with and one without intercept occur. All fits show excellent values for correlation coefficient CC and R^2 . For the golden hours plot CC and R^2 are closest to one.



(a) Slope of linear fit considering all measured data points averaged on 0.5 hour intervals.



(b) Slope of linear fit considering only those hours, where the cloud cover was 0 okta.

Figure 7.6: Slopes of linear fit (without intercept) of NO₂ SCDs scatter plots measured with the new and the Bremen MAX-DOAS system performed for each elevation separately. The errorbars show the error interval based on the coefficient of determination R^2 . The dashed lines indicate the interval of 5% deviation.

8 Mobile MAX-DOAS Measurements of NO₂

In the following chapter the results of mobile MAX-DOAS measurements around Bremen are presented. They provide information about NO₂ concentrations around Bremen at different height. Figure 8.1 shows a photograph of the measurement car during MAX-DOAS measurements close to highway, industrial harbour and steel plants.



Figure 8.1: IUP-Bremen measurement car in the field performing MAX-DOAS measurements close to highway, industrial harbour and steel plants.

8.1 Set-up and Measurement Conditions

At 5 August 2015 mobile MAX-DOAS measurements around the highway ring of Bremen have been performed. Beside the zenith direction (90°) two off-axis elevations have been used, 3° and 30°¹. In addition to the spectra that were averaged over an integration time of 5 s, all individual spectra were recorded. In Table 8.1 the conditions under that mobile measurements were performed are listed. 05 August 2015 was a clear sky day with only very little cloud cover and wind from south west. Figure 8.2 shows photographs recorded by the video camera integrated in the telescope box at 3° and at 30° elevation.

Date	Elevation angles [°]	Time UT	SZA [°]	cloud cover [Okta]	T [°C]	p [hPa]	wind speed [m/s]	wind direction [°]
05.08.2015	3,30,90	08:30-10:04	40-50	clear 0-1	22.7	1018.60	4.7	240

Table 8.1: Measurement conditions for mobile measurements. Temperature, pressure and wind data for the relevant time span have been taken from the DWD data of the Bremen weather station 690 (data accessible via: http://www.dwd.de/DE/klimaumwelt/cdc/cdc_node.html).

¹The the measurement sequence was 3°, 30°, 3°, 30°, 3°, 30°, 3°, 30°, 30°, 90°



(a) 3° elevation



(b) 30° elevation

Figure 8.2: Azimuthal viewing direction during mobile measurements at 05 August 2015 at off-axis elevations recorded by the video camera integrated in the telescope box. As mentioned, viewing conditions were excellent at this day.

8.1.1 Settings for Spectrometer's Gratings and the DOAS-Fit

The fitted species, polynomials and cross sections were the same that have been used for the intercomparison study and can be found in table 7.1. During the mobile measurements the grating with 600 g/mm was used for the UV spectrometer and the spectral range for the DOAS-fit was increased in the UV. The settings for grating and spectral range are shown in table 8.2.

Parameter	Settings UV	Remarks	Settings vis	Remarks
Spectral Range	338-370 nm	grating 2 (600 g/mm)	425-497 nm	grating 1 (1200 g/mm)

Table 8.2: Settings for mobile measurements: Gratings for the UV and visible spectrometer and spectral range for the DOAS-Fit.

8.2 Filtering Individual Measurements by Intensity

When performing mobile measurements from ground occasionally single measurements are affected by objects in the light path, e.g. trees, houses, traffic signs or bridges. An object in the light path blocks part of the sunlight and can therefore be identified by a drop of intensity in the recorded spectrum compared to spectra that were not disturbed.

To filter out the measurements that were disturbed before they are averaged over an integration time of 5 s, a DELPHI-Programme has been developed to perform an intensity filter on the individual measurements:

- The recorded individual spectra were fitted using the zenith spectrum with the highest SZA as reference with the settings listed in table 7.1 in section 7.1 and ZS-file fitting mode.
- The average intensity of the individual spectra was compared to the RMS of the DOAS fit.
- Based on the intensity and RMS profile for each elevation (3°, 30°, 90°) an individual intensity limit was chosen to minimise the RMS.

Measurements below the intensity limit were not taken into account for the 5 s averaged spectra. The 5 s averaged filtered and unfiltered spectra were subsequently fitted with ZS-File-Sync and the settings listed in table 7.1 and 8.2. The intensity limits for each elevation and the mean RMS of the DOAS fit of the averaged spectra using ZS-File-Sync before and after the filter was applied are shown in table 8.3.

By applying an intensity filter the mean RMS of the DOAS-Fit was significantly reduced:

- At 3° elevation by 64% in the UV and by 97% in the visible
- At 30° elevation by 43% in the UV and by 89% in the visible

This result confirms that applying an intensity filter is very effective to improve the quality of the DOAS-Fits substantially. This seems to be especially the case in the visible region.

Elevation angle [°]	Intensity limit [counts/s]	$\overline{\text{RMS}}_{\text{unfiltered}}$	$\overline{\text{RMS}}_{\text{filtered}}$	$\frac{\overline{\text{RMS}}_{\text{filtered}}}{\overline{\text{RMS}}_{\text{unfiltered}}}$ [%]
90	1.0·10 ⁴ (UV) 4.0·10 ⁴ (vis)	-	-	-
30	8·10 ³ (UV) 1.47·10 ⁴ (vis)	0.0012 (UV) 0.0100 (vis)	0.000689 (UV) 0.0011 (vis)	57% (UV) 11% (vis)
3	3.8·10 ³ (UV) 1.2·10 ⁴ (vis)	0.0015 (UV) 0.0239 (vis)	0.000540 (UV) 0.000623 (vis)	36% (UV) 3% (vis)

Table 8.3: Limit for the intensity filter for all used elevations, the mean RMS of the DOAS-fit before the intensity filter was applied ($\overline{\text{RMS}}_{\text{unfiltered}}$), the mean RMS of the DOAS-fit after using the intensity filter ($\overline{\text{RMS}}_{\text{filtered}}$) and the resulting fraction of $\overline{\text{RMS}}_{\text{filtered}}$ towards $\overline{\text{RMS}}_{\text{unfiltered}}$ in percent for measurements in the UV and visible.

8.3 Converting Slant Columns to Vertical Columns

Since the differential slant column densities obtained by performing the DOAS-Fit (SCDs) are depending on elevation angle, position of the sun and viewing conditions, a conversion to vertical column densities (VCDs) is necessary to allow comparison of measurements of different days.

To convert SCDs into VCDs two different approaches have been used:

- AMFs simulated by SCIATRAN for a SZA of 40 (for measurements with SZA ≤ 45) and of 50 (for measurements with SZA ≤ 50) were used to convert the fitted SCDs into VCDs.
- The geometric approach described in 4.4 was applied assuming a block profile.

Table 8.4 shows the AMF modelled with SCIATRAN and calculated using the geometric approach $\text{AMF}_{\text{geo}}(\alpha) = \sin \alpha^{-1}$.

The NO₂ VCDs for elevation angle α were calculated by inserting the AMFs and the fitted NO₂ differential slant column densities into the following equation:

$$\text{VCD}_{\text{NO}_2, \alpha} = \frac{\text{SCD}_{\text{NO}_2, \alpha}}{\text{AMF}(\alpha) - \text{AMF}(90^\circ)}. \quad (8.1)$$

The deviation between geometric approach and SCIATRAN modelled data for the vertical column densities is given in table 8.5.

For the 30° elevation the geometric approach seems to be a good approximation for the VCD. The mean relative deviation to the SCIATRAN model in the UV is only 2.3% and in the visible 5%. For the 3° elevation the deviation of the geometric approach towards the modelled data is 39% in the UV and 16% in the visible. This deviation is clearly higher than the one at 30° elevation. Therefore the geometric approach might not be the best choice for the 3° elevation. This result suggests that the scattering point for the 3° elevation is inside the NO₂ layer.

The VCDs of the SCIATRAN AMFs are shown for the 3° elevation in figure 8.3 and for the 30° elevation in figure 8.4 for both channels of the system, the one operating in the visible and the one operating in the UV. The NO₂ vertical columns are

plotted at a *google earth* map. To reference the different areas at the plot, a grid of numbers and letters was overlaid (e.g. the box at the upper left corner of the figure is referred to as A1).

The NO₂ VCDs at 3° elevation are in its maximum values lower ($\approx 10 \cdot 10^{15}$ molec/cm²), than the ones at 30° elevation ($\approx 3 \cdot 10^{16}$ molec/cm²).

The measurement started at E2 at the NW1 of the University of Bremen. After a short drive through Bremen Horn-Lehe the measurement car entered the highway A 27. At G4 the measurement car passed the *Bremer Kreuz*. The motorway interchange forms the crossing between the A 27 and the A 1 and lays on the municipal border between Achim and Oyten. Nearby city districts of Bremen are Osterholz and Mahndorf. At this region (F3,G3 and G4) slightly increased NO₂ VCD were measured at 30°elevation. This is explainable by the high traffic volume. At the 3°elevation the magnitude of the measured NO₂ VCDs is also slightly increased and comparable to the ones measured at E2 and F3.

The measurements continued at the highway ring around Bremen. At the following section of the measurement route (G5, F4, E5), comparable low NO₂ VCDs were measured at 3°and 30°elevation. At D5, C5, B5 and A5, NO₂ VCDs at 3°elevation again slightly increase which indicates higher traffic related pollution. At B4 the measurement car was passing an avenue that was framed by trees. Therefore a lot of the measurements were filtered out.

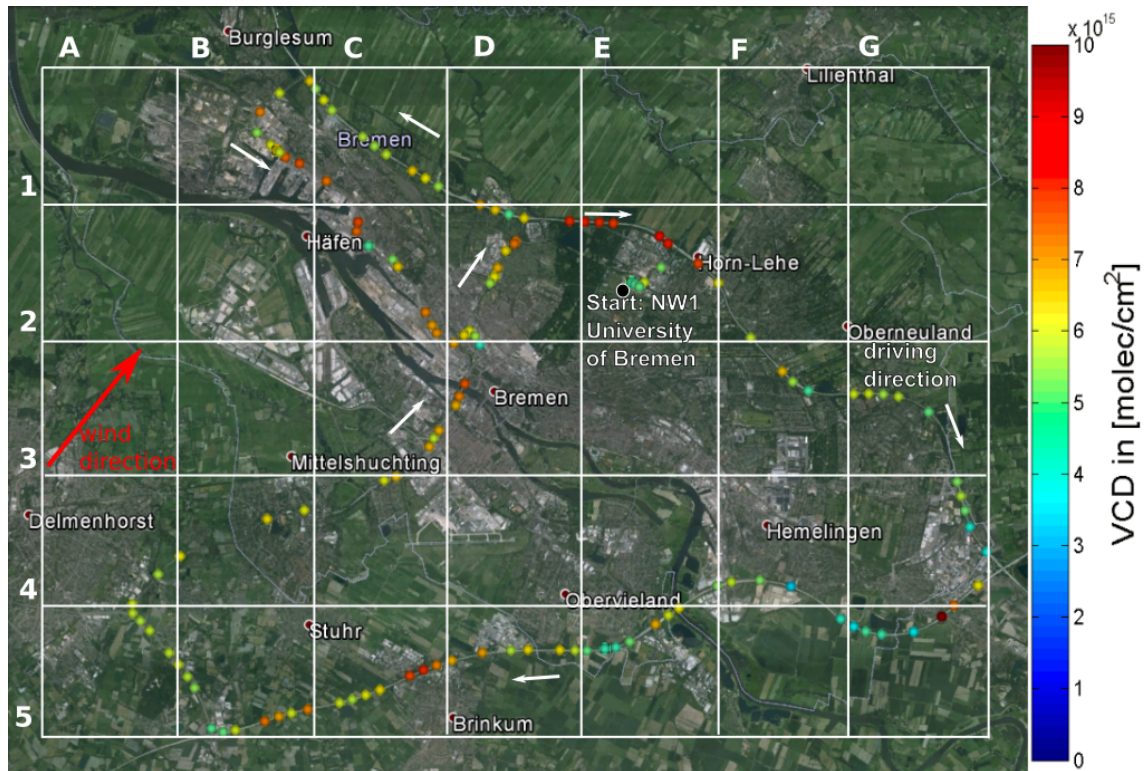
For the 30°elevation the measured NO₂ VCDs show a peak at B1. This peak is most probably linked to the industrial harbour of Bremen and the steel plants which are located at this spot. Higher NO₂ VCDs at 30°elevation can also be found at the C1 box. This peak is most probably also coming from the industrial harbour and the steel plants. The plumes were blown into this area by the south west wind. At 3°elevation no peak of NO₂ VCDs can be observed. This suggests that at 3°elevation, pointing is underneath the plume emitted by the industrial chimneys, so that only the traffic background pollution is measured.

AMF SCIATRAN					AMF geometric approach
λ α	UV: 350 nm		visible: 475 nm		UV/visible
	SZA=40	SZA=50	SZA=40	SZA=50	
3	12.4088	12.4880	16.5827	16.5992	19.1073
30	2.3813	2.3723	2.3139	2.3051	2
90	1.4045	1.4199	1.3638	1.3925	1

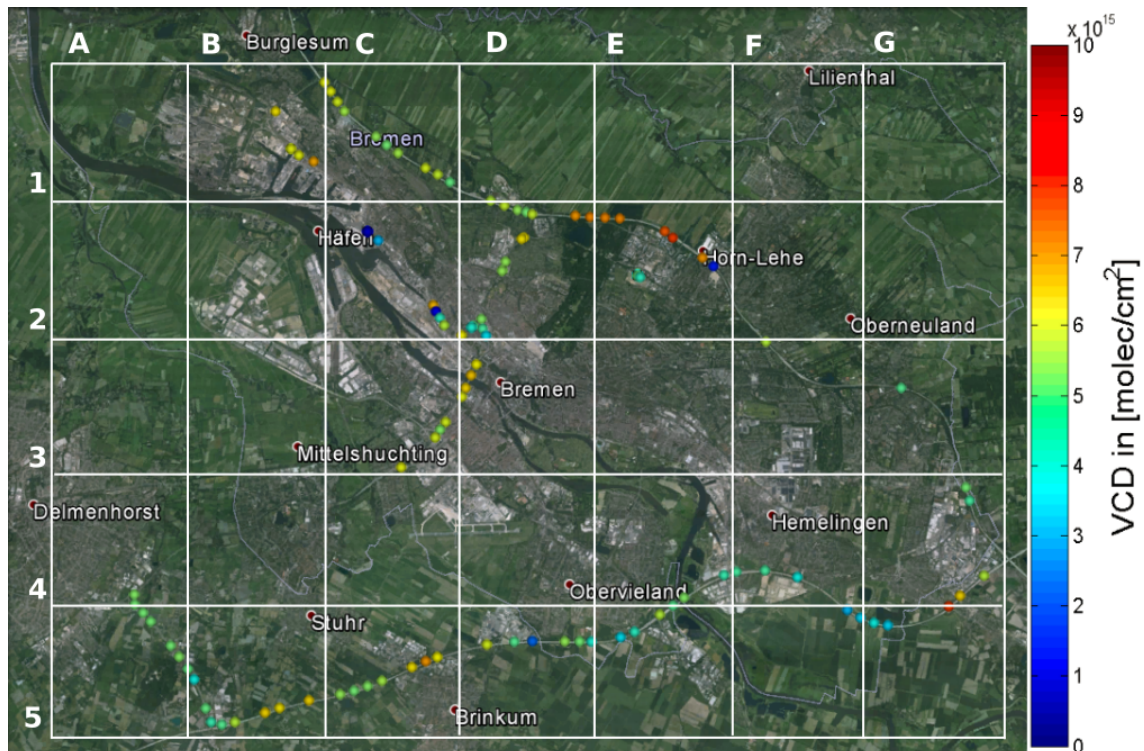
Table 8.4: AMF for all applied elevation angles α modelled by SCIATRAN and calculated using the geometric approach $\text{AMF}_{\text{geo}} = \frac{1}{\sin \alpha}$

Spectral range	Elevation α [°]	Mean absolute [molec/cm ²] (and relative) deviation of VCD_{geo} to $\text{VCD}_{\text{SCIATRAN}}$
UV	3	$(2.3 \pm 0.4) \cdot 10^{15}$ (39%)
vis	3	$(0.7 \pm 0.2) \cdot 10^{15}$ (16%)
UV	30	$(0.2 \pm 0.1) \cdot 10^{15}$ (2.3%)
vis	30	$(0.4 \pm 0.2) \cdot 10^{15}$ (5%)

Table 8.5: Mean absolute and relative deviation of VCD_{geo} to $\text{VCD}_{\text{SCIATRAN}}$.

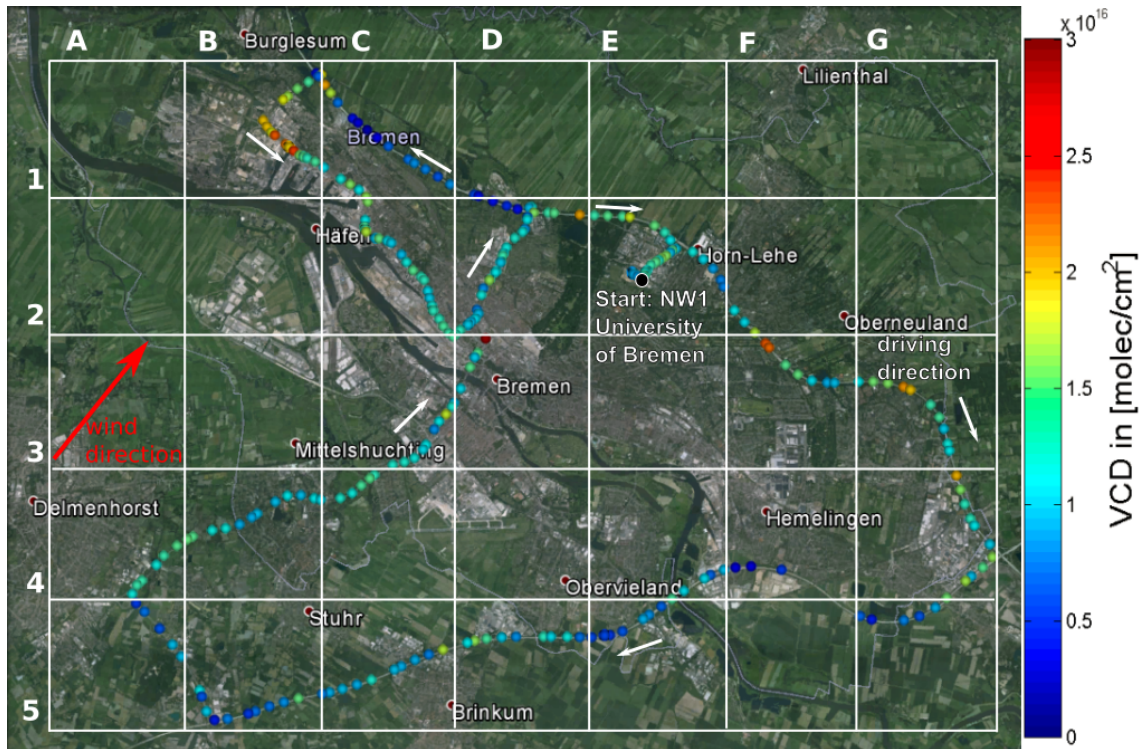


(a) NO_2 vertical column density measured in the UV at 3° elevation.

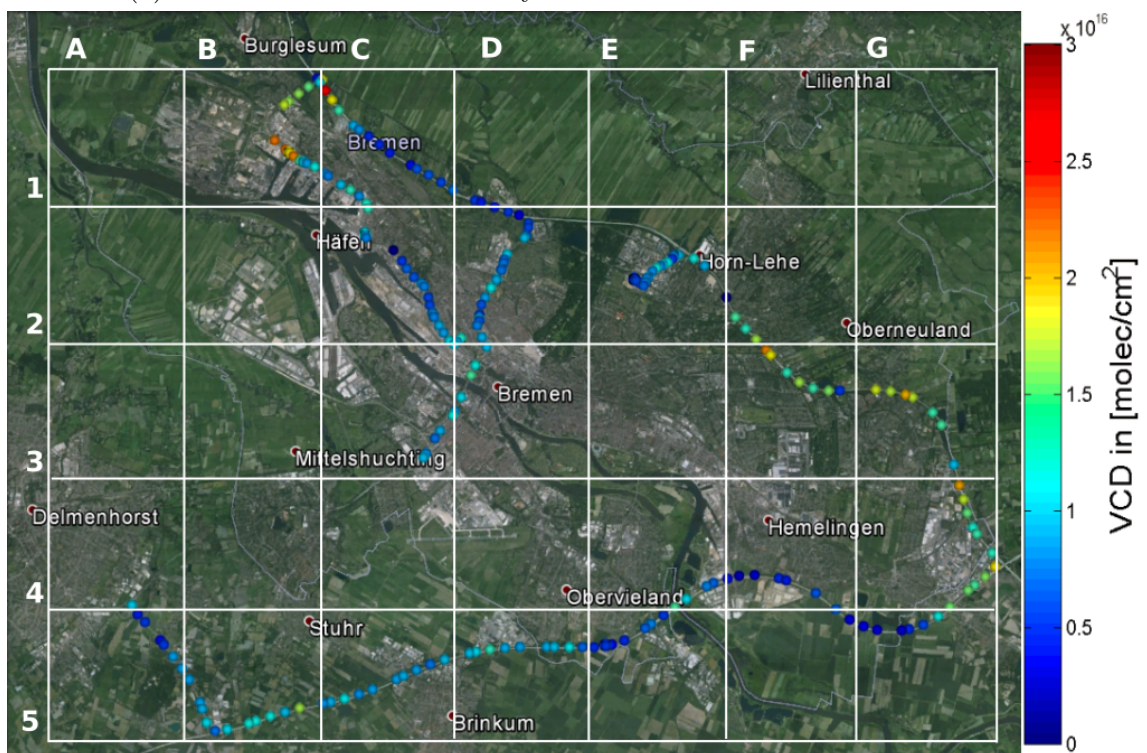


(b) NO_2 vertical column density measured in the visible at 3° elevation.

Figure 8.3: NO_2 VCD measured at 3° elevation using SCIATRAN AMFs in the UV and the visible range. The measurements started at the NW1 of the University of Bremen. The driving direction is indicated by white arrows. The wind direction is shown via a red arrow.



(a) NO₂ vertical column density measured in the UV at 30° elevation.



(b) NO₂ vertical column density measured in the visible at 30° elevation.

Figure 8.4: NO₂ VCD measured at 30° elevation using SCIATRAN AMFs in the UV and the visible range. The measurements started at the NW1 of the University of Bremen. The driving direction is indicated by white arrows. The wind direction is shown via a red arrow.

8.4 Converting Slant Columns to Volume Mixing Ratios

In section 4.4 two different approaches have been presented to convert differential slant column densities (SCDs) into volume mixing ratios (VMRs). In the following the geometric approach is used to convert the NO₂ SCDs at 30° elevation and the NO₂ SCDs at 3° elevation are converted by using O₄ as tracer.

Converting the SCDs at 3° elevation into VMRs

For the conversion of NO₂ SCDs measured at 3° elevation into VMRs, the measured differential slant column density of O₄, was used as tracer for the effective path length L_{O_4} (see equation 4.16). The NO₂ volume mixing ratio was calculated using the differential slant column density of NO₂ by:

$$\text{VMR}_{\text{tracer}} = \frac{\text{SCD}_{\text{NO}_2}(3^\circ)}{L_{O_4}} \cdot \frac{R \cdot T_{\text{air}}}{p_{\text{air}} \cdot N_A} \quad (8.2)$$

For T_{air} and p_{air} the values given in table 8.1 were used. The resulting volume mixing ratios of NO₂ are shown in figure 8.5.

Converting SCDs at 30° elevation into VMRs

As discussed in section 8.3 the geometric approach is a good approximation to convert NO₂ SCDs at 30° into VCDs. To obtain volume mixing ratios one has to use equation 4.15 and assume a typical value for the mixing layer height. For Bremen in summer, under clear sky conditions a mixing layer height of MLH=1500 m seems reasonable. The NO₂ VMRs at 30° elevation were calculated using:

$$\text{VMR}_{\text{geo}} = \frac{\text{VCD}_{\text{NO}_2}(30^\circ)}{\text{MLH}} \cdot \frac{R \cdot T_{\text{air}}}{p_{\text{air}} \cdot N_A} \quad (8.3)$$

For T_{air} and p_{air} the values given in table 8.1 were used.

The resulting NO₂ volume mixing ratios are shown in figure 8.6.

Discussion of the NO₂ VMRs

The magnitude of the calculated VMRs using two different methods for the two different elevations, is in the same order and has a maximum of approximately 8

ppb. The 30° elevation shows on average slightly lower NO₂ concentration than the 3° concentration. The qualitative distribution of NO₂ concentration around Bremen looks similar to the one observed for the NO₂ VCDs. At 30° elevation the VMR distribution is obviously the same than the VCD distribution. At 3° elevation the NO₂ VMRs show peak values at G4,F4 that were not observed for the NO₂ VCDs. At C1 the VMRs show higher NO₂ values than the VCDs at 3° elevation. The higher NO₂ concentrations at C1 compared to B1 and C2 could be explained with the wind coming from south west. It blows the NO_x emissions close to the surface from C2, B1 towards C1.

The in-situ measurement stations of Bremen's air quality measurement network *BUI SY*² close to the measurement route were DEHB002 *Bremen-Ost* at F3 which measured 10 ppb NO₂, DEHB012 *Bremen-Oslebshausen* at B1 which measured 9 ppb NO₂ and DEHB013 *Bremen-Hasenbüren* at B2 which measured 5 ppb NO₂ (all values are one-hour averaged).

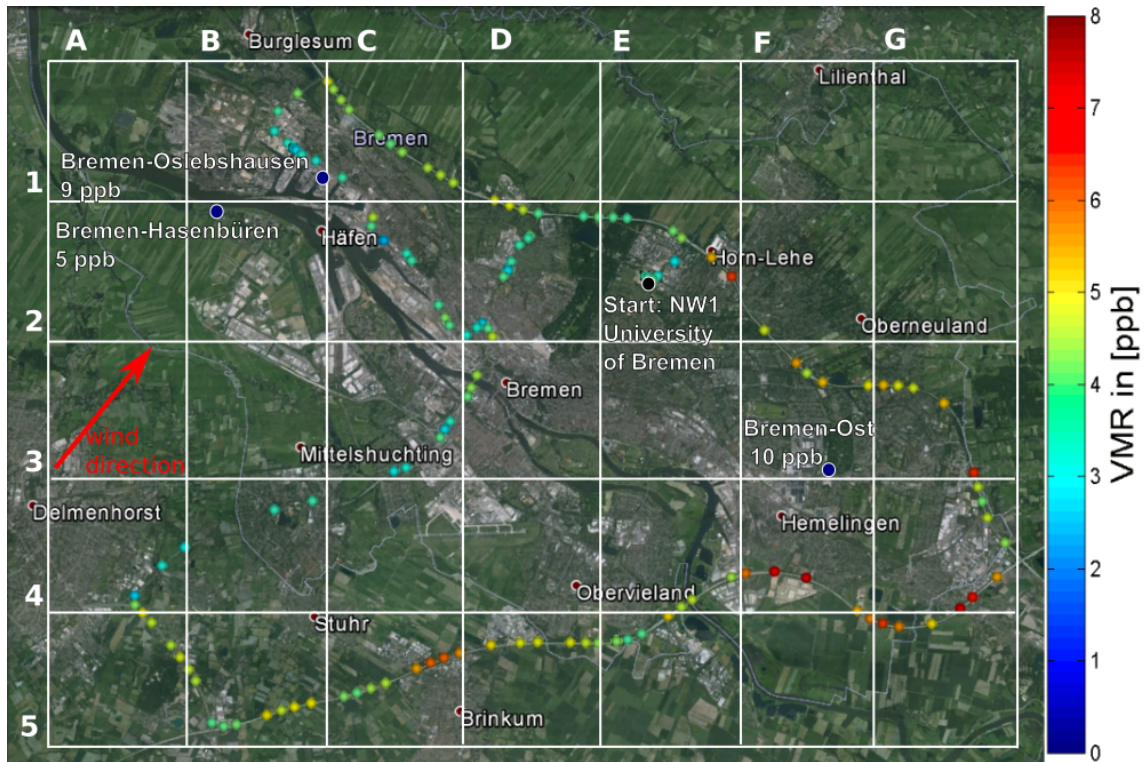
At G3, G4 and F4, the area closest to the *Bremen-Ost* measurement station, the NO₂ VMRs at 3° elevation show the highest values at the route with up to 8 ppb. This is in good accordance with the measured 10 ppb at the *Bremen-Ost* station. The NO₂ VMRs calculated for the 30° elevation showed much lower values of 1 to 5 ppb.

At the area close to the industrial harbour (B1, C1) the NO₂ VMRs calculated for the 3° elevation are with 4 to 5 ppb lower than the measurements of the nearby *Bremen-Oslebshausen* station but are in good accordance with the values for the *Bremen-Hasenbüren* station, which is located off-street. This indicates that at 3° elevation the background pollution is measured. The NO₂ VMRs at 30° elevation show here the highest values at the route. With concentrations up to 8 ppb they reproduce the measured 9 ppb at the *Bremen-Oslebshausen* station very well.

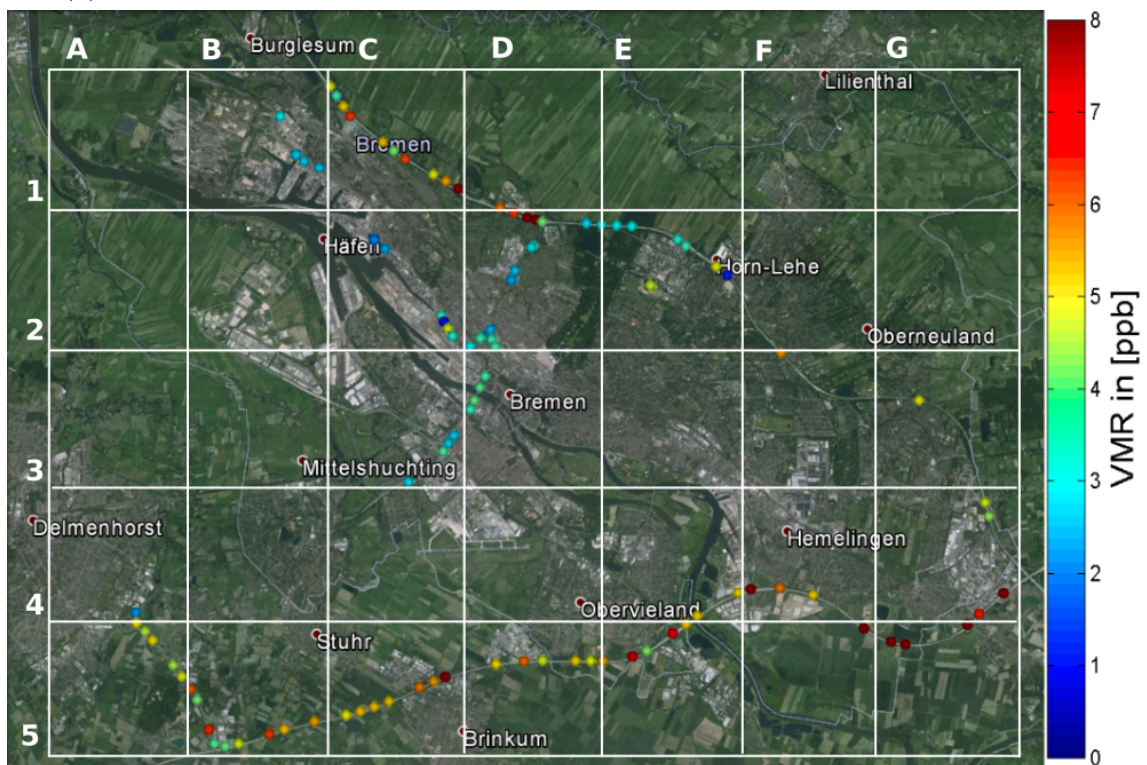
The calculated VMRs are generally in very good accordance with the measurements of the in-situ stations of the *BUI SY* network, considering that two completely different measurement techniques are compared. While the measurements at 3° elevation are very effective in tracking traffic related NO_x emissions, e.g. at the *Bremer*

²Data accessible via: <http://www.umweltbundesamt.de/daten/luftbelastung/aktuelle-luftdaten>

Kreuz, the 30° elevation measurements better reproduce industrial NO_x emissions at the industrial harbour.

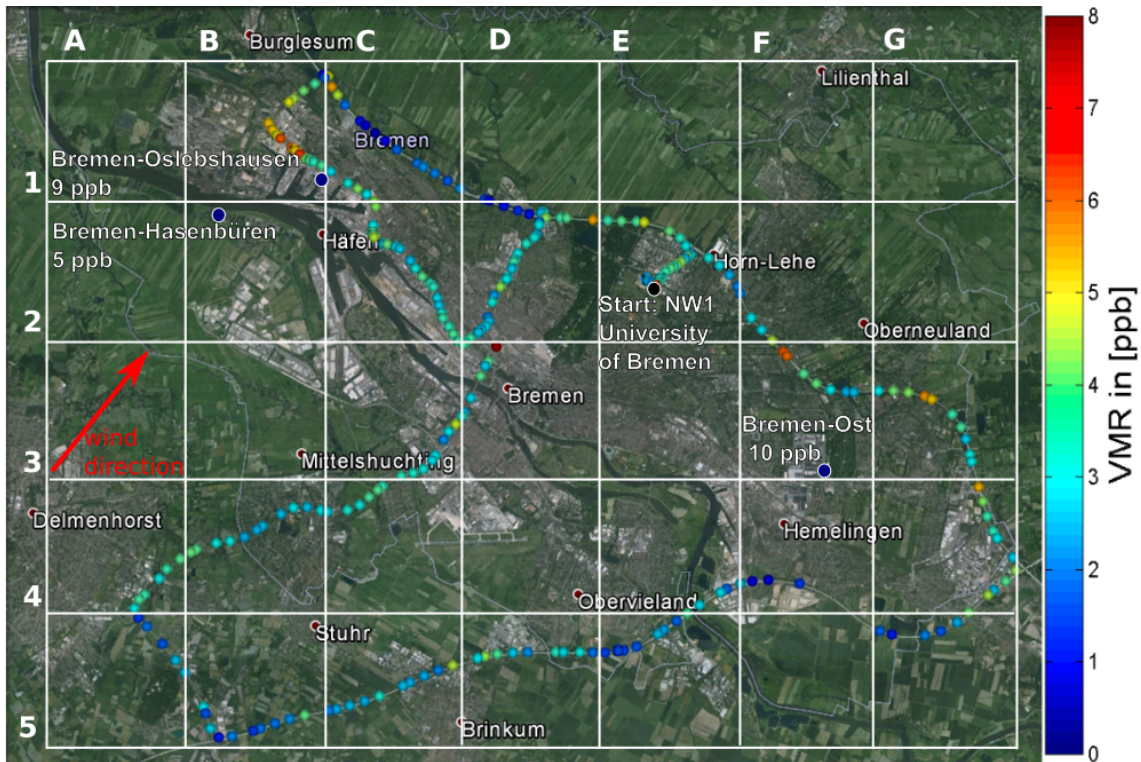


(a) VMR of NO₂ at 3° elevation using measurements of NO₂ and O₄ in the UV.

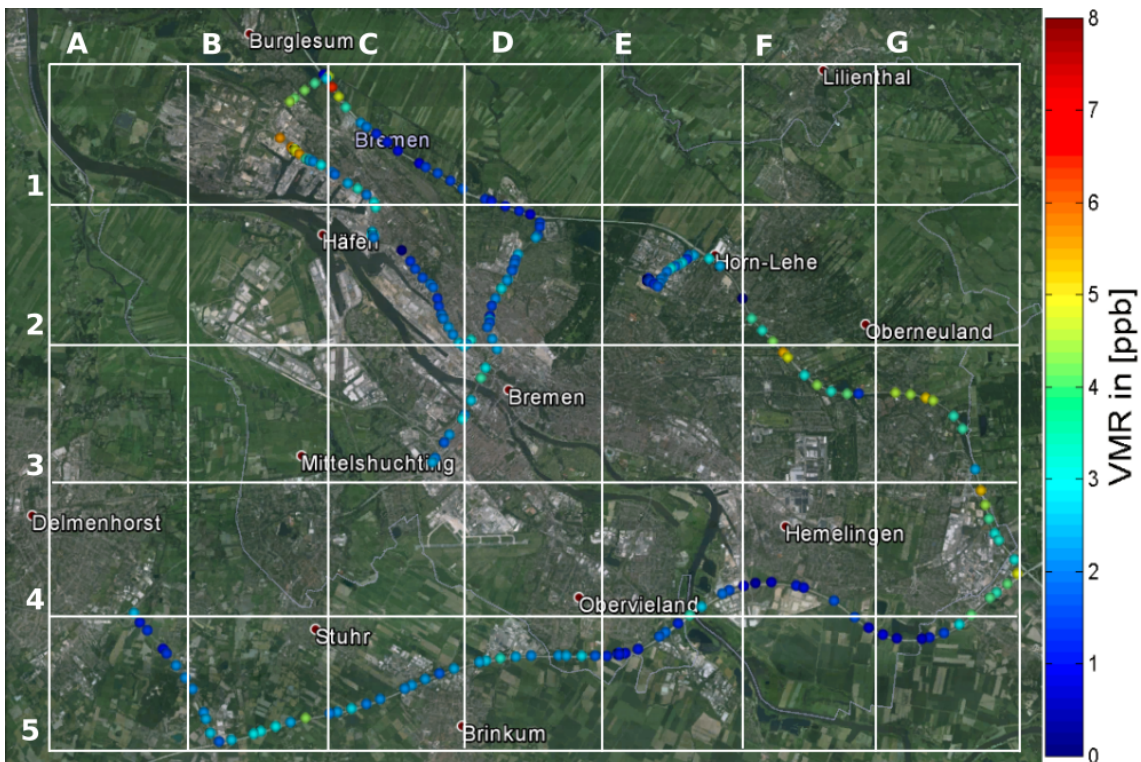


(b) VMR of NO₂ at 3° elevation using measurements of NO₂ and O₄ in the visible.

Figure 8.5: VMR at 3° elevation using O₄ as tracer for the effective path length and the stations of the *BUI*SY network close to the route with the corresponding 1-hour averaged VMRs.



(a) VMR of NO_2 at 30° elevation using measurements of NO_2 and O_4 in the UV.



(b) VMR of NO_2 at 3° elevation using measurements of NO_2 and O_4 in the visible.

Figure 8.6: Volume mixing ratio of NO_2 at 30° elevation using the geometric approach to obtain the air mass factor and assuming a typical mixing layer height of 1500 m.

8.4.1 Estimation of the Error of NO₂ Number Density

Error of NO₂ number density at 30° elevation

For the geometric approach a typical mixing layer height has to be estimated. This introduces a high uncertainty of approximately 30%. In addition the geometric approach assumes a block profile, which can lead to further uncertainties. Therefore the error of the NO₂ number density obtained using the geometric approach can be > 30%.

Error of NO₂ number density at 3° elevation

The approach to estimate the effective light path length using the measured O₄ SCDs by Gomez et al. (2013) has only been used for horizontal viewing directions at an elevation angle of 0°. Using it for the 3° elevation will lead to errors, since the concentration of O₄ is changing along the light path with decreasing air density. In the following the estimation of the induced error will be presented.

- The O₄ number density n_{O_4} will change along the light path. It is proportional to the number density of air n_{air} :

$$n_{O_4} = (0.20942 \cdot n_{\text{air}})^2 \quad (8.4)$$

- The change of n_{air} with pressure p_{air} and temperature T_{air} is known from the ideal gas law:

$$n_{\text{air}} = \frac{p_{\text{air}}}{k_B \cdot T_{\text{air}}} \quad (8.5)$$

- The effective light path L_{O_4} at elevation $\alpha = 3^\circ$ is calculated using the O₄ tracer approach and the fitted O₄ differential slant column densities:

$$L_{O_4} = \frac{\text{SCD}_{O_4}(\alpha)}{n_{O_4}} \quad (8.6)$$

- The height of the scatter point H_{scatter} at elevation $\alpha=3^\circ$ has been estimated using a simple geometric approach:

$$H_{\text{scatter}} = L_{O_4} \cdot \sin \alpha \quad (8.7)$$

- The change of pressure with height is given by the barometric equation (equation 2.1 in chapter 2). Assuming a typical scale height H of 8 km the ratio of pressure at the height of the scatter point $p(H_{\text{scatter}})$ towards the surface pressure p_0 has been calculated.

Table 8.6 shows the results of the calculations explained above. The effective light path was calculated using the pressure at sea level height given in table 8.1. The percentage deviation in pressure at height of the scatter point towards sea level pressure is also given in table 8.6.

With this percentage deviation in pressure it is possible to estimate the percentage

Spectral range	$L_{\text{O}_4, \text{mean}} \pm L_{\text{O}_4, \text{std}}$ [m]	H_{scatter} [m]	$\frac{p(H_{\text{scatter}})}{p_0}$	Percentage deviation in pressure
UV	6000±2000	314±104	max: 0.949 av: 0.961 min: 0.974	max: 5.1% av: 3.9% min: 2.6%
vis	7000±4000	366±209	max: 0.930 av: 0.955 min: 0.980	max: 7% av: 4.5% min: 2%

Table 8.6: Preliminary results for the error estimation of n_{NO_2} : Mean effective light path length L_{O_4} , estimated height of the scatter point H_{scatter} and the associated change of pressure along the light path for UV and vis at 05 August 2015.

deviation of the calculated NO_2 number density in several steps using the laws of propagation of uncertainty:

- A percentage deviation in pressure $\frac{\Delta p}{p}$ of $\leq 5.1\%$ in the UV and $\leq 7\%$ in the visible leads to a percentage deviation of n_{O_4} :

$$\frac{\Delta n_{\text{O}_4}}{n_{\text{O}_4}} = 2 \cdot \frac{\Delta p}{p} \quad (8.8)$$

- The light path length was calculated with a relative error of:

$$\frac{\Delta L_{O_4}}{L_{O_4}} = -2 \frac{\Delta p}{p} \quad (8.9)$$

- The resulting relative error of the number density of NO₂ is:

$$\frac{\Delta n_{NO_2}}{n_{NO_2}} = -\frac{\Delta L_{O_4}}{L_{O_4}} = 2 \cdot \frac{\Delta p}{p} \quad (8.10)$$

Hence the overestimation of pressure about $\leq 7\%$ leads to an underestimation of the effective light path length of 14% and an overestimation of the resulting number density of NO₂ of 14%.

This result can only be a first approximation of the relative error of n_{NO_2} , since it was ignored that the calculation leading to the assumed $H_{scatter}$ was already underlying the overestimation of pressure. To take this point into account an iterative method has been used. At each iteration the relative deviation of L_{O_4} calculated in the previous run is added onto the effective light path length of O₄ and the calculation of all parameters presented in table 8.6 is repeated:

$$L_{O_4}(i) = L_{O_4,0} \cdot \left(1 + 2 \cdot \frac{\Delta p}{p_0} (i - 1) \right) \quad (8.11)$$

$$H_{scatter}(i) = \sin \alpha \cdot L_{O_4}(i) \quad (8.12)$$

$$\frac{\Delta p}{p_0}(i) = \exp \left(-\frac{H_{scatter}(i)}{H} \right) \quad (8.13)$$

This iterative method converges after 7 steps in the UV and after 10 in the visible. The resulting maximum relative error of n_{NO_2} in the UV is 12%, in the visible 16%.

9 Summary, Conclusions and Outlook

Summary and Conclusions

Within the scope of this thesis a new MAX-DOAS system was set up. The calibration measurements of the CCD detector delivered the optimum operational temperature of the CCD and the best detector gain mode. The optimal operation temperature for the CCD detector is -45°C . Both detectors show excellent linearity, even lower than the manufacturer's guarantee. The best gain for the UV detector is the Low Noise mode, the best gain for the visible detector is the High Capacity mode.

In the calibration measurements for the spectrometers the resolution was determined by measuring the slit function (FWHM). The measured resolutions show that both spectrometers are perfectly suited for the retrieval of NO_2 . The best grating for this purpose in the UV is the 600 g/mm grating with a resolution of approximately 0.5 nm. In the visible the grating of choice is the 1200 g/mm grating with a resolution of approximately 0.6 nm. The 1200 g/mm grating of the UV imaging spectrometer shows an excellent resolution of approximately 0.26 nm and is therefore suited for the retrieval of very narrow-band structured trace gases like SO_2 . For the UV spectrometer the measured slit function shows only minimal variations for different detector and grating positions. This excellent spacial agreement of the slit function makes the UV spectrometer also an outstanding choice for imaging applications. The spacial agreement of the visible spectrometer is not as good as the one observed for the UV spectrometer. Therefore it should only be used with full vertical binning.

The intercomparison between the MAX-DOAS system set up in the scope of this thesis and the instrument operating continuously at the roof at the IUP Bremen generally showed very good agreement of the measured NO_2 differential slant column densities. The means of the fitted slopes for NO_2 were within 5% of unity for

most elevation angles in the UV and 8% in the visible. When only cloud free hours were taken into account for the intercomparison, the deviations were even smaller (1.3% in the UV and 7.6% in the visible). Similar intercomparison campaigns, e.g. Roscoe et al. (2010), show comparable results for the agreement of NO₂ slant column densities of two channel MAX-DOAS systems.

The mobile MAX-DOAS measurements performed around Bremen included off-axis measurements at 30° and at 3° elevation. For the first time, mobile MAX-DOAS measurements with elevation angles smaller than 30° were evaluated in this thesis. For mobile measurements it can happen that the sight of the instrument is affected by objects in the light path, e.g. trees, signs, bridges or buildings. This is especially the case for the 3° elevation. To filter out individual spectra which were influenced by objects in the light path, an automatic routine was developed. By using this filtering routine, the RMS of the NO₂ fits could be reduced by up to 97% at 3° elevation and up to 89% at 30° elevation.

By applying two different off-axis elevations NO₂ concentrations were estimated at different heights. To convert the measured differential slant column densities into vertical column densities, two different approaches have been applied: SCIATRAN modelled air mass factors and a simple geometric approach. For the 30° elevation both approaches agree very well (5% deviation in the visible and 2.3% deviation in the UV). For the 3° elevation the geometric approach should not be used. The deviations between both methods in the visible are 16%, in the UV 39%. This result was expected since at 3° elevation the scatter point most likely is inside the NO₂ layer.

To convert the differential slant column densities into volume mixing ratios (VMRs), different approaches have been applied for the 3° and the 30° elevation. For the 3° elevation the effective light path length was determined by using the differential slant column density of the oxygen collision complex O₄. This approach genuinely assumes that the scattering point is close to the station level. Therefore it has so far only been used for the 0° elevation. The maximum relative error for the NO₂ number density induced by using the 3° elevation was estimated to be 12% in the UV and 16% in the visible. For the 30° elevation the geometric approach was used, assuming a block profile of NO₂ and a mixing layer height of 1500 m.

The obtained NO₂ VMR profiles show different concentration distributions for the measurements using 3° elevation and those that were measured at 30° elevation: The 3° elevation VMRs show particularly high concentrations in areas with high traffic volume. The 30° elevation VMRs show high concentrations in the area of the industrial harbour and the adjacent steel plants. The 3° elevation VMRs show rather low values in this area. Obviously, traffic connected NO_x emissions can best be retrieved by using the 3° elevation. In contrast, the 30° elevation is better to detect industrial NO_x emissions because the 3° elevation is pointing beneath the plume emitted from high chimneys. Furthermore, the NO₂ profiles show the influence of wind direction on the measured NO₂ concentrations. The measured NO₂ VMRs show in general very good agreement with the measurements of in situ stations of the Bremen air quality measurement network *BUISTY*. The maximum VMR of 8 ppb is far below the WHO limit of 21 ppb for the annual mean.

Outlook

When performing mobile measurements, the actual elevation can deviate from the one adjusted by the pan-tilt head, for example when the measuring car is driving a slope. To know the actual elevation, an inclinometer in the telescope box would be helpful. Previous studies by Seyler (2011) showed that a life adjustment of the pan-tilt head is not applicable. Therefore the inclinometer should only be used for real time control of the elevation and a correction should happen subsequently.

For further studies with the mobile MAX-DOAS system, imaging applications are an interesting option. By using a sufficient number of azimuthal viewing directions and elevation angles, trace gas profiles can be observed at variable places.

The excellent resolution of the UV spectrometer makes it ideally suited for SO₂ retrievals, e.g. for the measurement of shipping emissions in the scope of the *mesmart* project.¹

¹Measurement of shipping emissions in the marine troposphere (<http://www.mesmart.de>)

10 Bibliography

- A Beer. Bestimmung der Absorption des rothen Lichts in farbigen Flüssigkeiten. *Ann. Phys.*, 1852. URL https://scholar.google.de/scholar?q=August+Beer+in+1852&btnG=&hl=de&as_sdt=0%2C5#0.
- K Bogumil, J Orphal, T Homann, S Voigt, P Spietz, O.C Fleischmann, A Vogel, M Hartmann, H Kromminga, H Bovensmann, J Frerick, and J.P Burrows. Measurements of molecular absorption spectra with the SCIAMACHY pre-flight model: instrument characterization and reference data for atmospheric remote-sensing in the 230–2380 nm region. *J. Photochem. Photobiol. A Chem.*, 157(2-3): 167–184, may 2003. ISSN 10106030. doi: 10.1016/S1010-6030(03)00062-5. URL <http://www.sciencedirect.com/science/article/pii/S1010603003000625>.
- Pierre Bouguer. *Essai D’Optique, Sur La Gradation De La Lumiere*. 1729. URL <https://books.google.com/books?hl=de&lr=&id=UxJaAAAAcAAJ&pgis=1>.
- Claude Camy-Peyret and Andrei A. Vigasin. *Weakly Interacting Molecular Pairs: Unconventional Absorbers of Radiation in the Atmosphere*. 2003. ISBN 1402015968. URL <https://books.google.com/books?hl=de&lr=&id=8Bbdxnjj-dgC&pgis=1>.
- Wolfgang Demtröder. *Laser Spectroscopy: Vol. 1: Basic Principles*, volume 9. Springer Science + Business Media, 2008. ISBN 354073418X. URL <https://books.google.com/books?id=5vuqvvb9YxkC&pgis=1>.
- Wolfgang Demtröder. *Molekülphysik: Theoretische Grundlagen und experimentelle Methoden*. Oldenbourg Verlag, 2013. ISBN 3486706780. URL <https://books.google.com/books?id=WVgZBJHBI3MC&pgis=1>.
- G. M. B. Dobson and D. N. Harrison. Measurements of the Amount of Ozone in the Earth’s Atmosphere and Its Relation to Other Geophysical Conditions. *Proc. R. Soc. A Math. Phys. Eng. Sci.*, 110(756):660–693, apr 1926. ISSN 1364-5021.

- doi: 10.1098/rspa.1926.0040. URL <http://rspa.royalsocietypublishing.org/content/110/756/660>.
- L. Gomez, M. Navarro-Comas, O. Puentedura, Y. Gonzalez, E. Cuevas, and M. Gil-Ojeda. Long-path averaged mixing ratios of O₃ and NO₂ in the free troposphere from mountain MAX-DOAS. *Atmos. Meas. Tech. Discuss.*, 6(5):8235–8267, sep 2013. ISSN 1867-8610. doi: 10.5194/amtd-6-8235-2013. URL <http://www.atmos-meas-tech-discuss.net/6/8235/2013/amtd-6-8235-2013.html>.
- V. Gorshelev, A. Serdyuchenko, M. Weber, W. Chehade, and J. P. Burrows. High spectral resolution ozone absorption cross-sections – Part 1: Measurements, data analysis and comparison with previous measurements around 293 K. *Atmos. Meas. Tech.*, 7(2):609–624, feb 2014. ISSN 1867-8548. doi: 10.5194/amt-7-609-2014. URL <http://www.atmos-meas-tech.net/7/609/2014/amt-7-609-2014.html>.
- J. F. Grainger and J. Ring. Anomalous Fraunhofer Line Profiles. *Nature*, 193 (4817):762–762, feb 1962. ISSN 0028-0836. doi: 10.1038/193762a0. URL <http://adsabs.harvard.edu/abs/1962Natur.193..762G>.
- Hermann Haken and Hans C. Wolf. *Molekülphysik und Quantenchemie: Einführung in die experimentellen und theoretischen Grundlagen*. Springer-Verlag, 2013. ISBN 3662088304. URL <https://books.google.com/books?id=qde2BgAAQBAJ&pgis=1>.
- G Hönninger. Multi axis differential optical absorption spectroscopy (MAX-DOAS). *Atmos. Chem. Phys.*, 4. Jg.(Nr. 1):S. 231–254., 2004. URL <http://www.atmos-chem-phys.net/4/231/2004/acp-4-231-2004.pdf>.
- IPCC: Working Group I. 7.4.2 Nitrogen Compounds - AR4 WGI Chapter 7: Couplings Between Changes in the Climate System and Biogeochemistry, 2007. URL https://www.ipcc.ch/publications_and_data/ar4/wg1/en/ch7s7-4-2.html.
- Daniel Jacob. *Introduction to Atmospheric Chemistry*. Princeton University Press, 1999. ISBN 0691001855. URL <https://books.google.com/books?id=14whM9fE0zsC&pgis=1>.
- Johann Heinrich Lambert. *Photometria*. 1760. URL <https://books.google.com/books?hl=de&lr=&id=tbM6AAAAcAAJ&pgis=1>.

- Richard Meller and Geert K. Moortgat. Temperature dependence of the absorption cross sections of formaldehyde between 223 and 323 K in the wavelength range 225–375 nm. *J. Geophys. Res.*, 105(D6):7089, mar 2000. ISSN 0148-0227. doi: 10.1029/1999JD901074. URL <http://doi.wiley.com/10.1029/1999JD901074>.
- NPR. 'It Was Installed For This Purpose,' VW's U.S. CEO Tells Congress About Defeat Device : The Two-Way : NPR, 2015. URL <http://www.npr.org/sections/thetwo-way/2015/10/08/446861855/volkswagen-u-s-ceo-faces-questions-on-capitol-hill>.
- Enno Peters. Improved MAX-DOAS measurements and retrievals focused on the marine boundary layer. *Ph.D. thesis, Univ. Bremen*, 2013.
- G Pinardi and F Hendrick. On the use of the MAX-DOAS technique for the validation of tropospheric NO₂ column measurements from satellite. *Proc. EUMETSAT Meteorol. Satell. Conf. Darmstadt*, 2008. URL http://uv-vis.bira-iasb.be/publications/proceedings/2008_pinardi.pdf.
- Ulrich Platt and Jochen Stutz. Differential Optical Absorption Spectroscopy - Principle and Applications. 2008. doi: 10.1007/978-3-540-75776-4. URL <http://www.springerlink.com/index/10.1007/978-3-540-75776-4>.
- Andreas Richter. *Absorptionsspektroskopische Messungen stratosphärischer Spurengase über Bremen*, 53 N. Ph.d., University of Bremen, 1997.
- H. K. Roscoe, M. Van Roozendael, C. Fayt, A. du Piesanie, N. Abuhassan, C. Adams, M. Akrami, A. Cede, J. Chong, K. Clémer, U. Friess, M. Gil Ojeda, F. Goutail, R. Graves, A. Griesfeller, K. Grossmann, G. Hemerijckx, F. Hendrick, J. Herman, C. Hermans, H. Irie, P. V. Johnston, Y. Kanaya, K. Kreher, R. Leigh, A. Merlaud, G. H. Mount, M. Navarro, H. Oetjen, A. Pazmino, M. Perez-Camacho, E. Peters, G. Pinardi, O. Puentedura, A. Richter, A. Schönhardt, R. Shaiganfar, E. Spinei, K. Strong, H. Takashima, T. Vlemmix, M. Vrekoussis, T. Wagner, F. Wittrock, M. Yela, S. Yilmaz, F. Boersma, J. Hains, M. Kroon, A. Piters, and Y. J. Kim. Intercomparison of slant column measurements of NO₂ and O₄ by MAX-DOAS and zenith-sky UV and visible spectrometers. *Atmos. Meas. Tech.*, 3(6):1629–1646, nov 2010. ISSN 1867-8548. doi: 10.5194/amt-3-1629-2010. URL <http://www.researchgate.net/publication/>

49608343_Intercomparison_of_slant_column_measurements_of_NO2_and_04_by_MAX-DOAS_and_zenith-sky_UV_and_visible_spectrometers.

L.S. Rothman, I.E. Gordon, A. Barbe, D.Chris Benner, P.F. Bernath, M. Birk, V. Boudon, L.R. Brown, A. Campargue, J.-P. Champion, K. Chance, L.H. Coudert, V. Dana, V.M. Devi, S. Fally, J.-M. Flaud, R.R. Gamache, A. Goldman, D. Jacquemart, I. Kleiner, N. Lacome, W.J. Lafferty, J.-Y. Mandin, S.T. Massie, S.N. Mikhailenko, C.E. Miller, N. Moazzen-Ahmadi, O.V. Naumenko, A.V. Nikitin, J. Orphal, V.I. Perevalov, A. Perrin, A. Predoi-Cross, C.P. Rinsland, M. Rotger, M. Šimečková, M.A.H. Smith, K. Sung, S.A. Tashkun, J. Tennyson, R.A. Toth, A.C. Vandaele, and J. Vander Auwera. The HITRAN 2008 molecular spectroscopic database. *J. Quant. Spectrosc. Radiat. Transf.*, 110(9-10):533–572, jun 2009. ISSN 00224073. doi: 10.1016/j.jqsrt.2009.02.013. URL <http://www.sciencedirect.com/science/article/pii/S0022407309000727>.

Wolfgang Schöpp, Markus Amann, Imrich Bertok, Janusz Cofala, Frantisek Gyarfas, Chris Heyes, Zbigniew Klimont, and Wilfried Winiwarter. Baseline scenarios for the clean air for Europe (CAFE) programme. *Final Rep.*, 79, 2005. URL [http://www.researchgate.net/profile/Wilfried_Winiwarter/publication/230709470_Baseline_Scenarios_for_the_Clean_Air_for_Europe_\(CAFE\)_Programme._CAFE_Report_1/links/0912f50d3918f5a5ff000000.pdf](http://www.researchgate.net/profile/Wilfried_Winiwarter/publication/230709470_Baseline_Scenarios_for_the_Clean_Air_for_Europe_(CAFE)_Programme._CAFE_Report_1/links/0912f50d3918f5a5ff000000.pdf).

John H. Seinfeld and Spyros N. Pandis. *Atmospheric Chemistry and Physics: From Air Pollution to Climate Change*. 2012. ISBN 1118591364. URL <https://books.google.com/books?hl=de&lr=&id=YH2K9eWsZ0cC&pgis=1>.

André Seyler. *Implementierung und Charakterisierung eines Inklinometers in einem MAX-DOAS*. B.sc., University of Bremen, 2011.

Warren Smith. *Modern Optical Engineering, 4th Ed.* 2007. ISBN 0071593756. URL https://books.google.de/books/about/Modern_Optical_Engineering_4th_Ed.html?id=DrTM_bAnf_YC&pgis=1.

S Solomon and RW Portmann. On the role of nitrogen dioxide in the absorption of solar radiation. *J. Geophys. Res.*, VOL. 104(NO. D10):12,047–12,058M, 1999. URL <http://onlinelibrary.wiley.com/doi/10.1029/1999JD900035/full>.

E. Spinei, A. Cede, J. Herman, G. H. Mount, E. Eloranta, B. Morley, S. Baidar, B. Dix, I. Ortega, T. Koenig, and R. Volkamer. Ground-based direct-sun

- DOAS and airborne MAX-DOAS measurements of the collision-induced oxygen complex, O₂O₂, absorption with significant pressure and temperature differences. *Atmos. Meas. Tech.*, 8(2):793–809, feb 2015. ISSN 1867-8548. doi: 10.5194/amt-8-793-2015. URL <http://www.atmos-meas-tech.net/8/793/2015/amt-8-793-2015.html>.
- Ryan Thalman and Rainer Volkamer. Temperature dependent absorption cross-sections of O₂–O₂ collision pairs between 340 and 630 nm and at atmospherically relevant pressure. *Phys. Chem. Chem. Phys.*, 15(37):15371, aug 2013. ISSN 1463-9076. doi: 10.1039/c3cp50968k. URL <http://pubs.rsc.org/en/content/articlehtml/2013/cp/c3cp50968k>.
- Umweltbundesamt. Stickstoffdioxid (NO₂) im Jahr 2014, 2015. URL http://www.umweltbundesamt.de/sites/default/files/medien/358/dokumente/no2_2014_2.pdf.
- AC Vandaele and C Hermans. Fourier transform measurement of NO₂ absorption cross-section in the visible range at room temperature. *J. Atmos. Chem.*, 1996. URL <http://link.springer.com/article/10.1007/BF00053797>.
- V.V.Rozanov and A.V.Rozanov. User’s Guide for the Software Package SCIATRAN, 2013. URL http://www.iup.uni-bremen.de/sciatran/free_downloads/users_guide_sciatran.pdf.
- T Wagner and C Von Friedeburg. UV-visible observations of atmospheric O₄ absorptions using direct moonlight and zenith-scattered sunlight for clear-sky and cloudy sky conditions. *J. Geophys. Res. Atmos.*, 107:AAC—3, 2002. URL <http://onlinelibrary.wiley.com/doi/10.1029/2001JD001026/full>.
- T. Wagner, O. Ibrahim, R. Shaiganfar, and U. Platt. Mobile MAX-DOAS observations of tropospheric trace gases. *Atmos. Meas. Tech.*, 3(1):129–140, feb 2010. ISSN 1867-8548. doi: 10.5194/amt-3-129-2010. URL <http://www.atmos-meas-tech.net/3/129/2010/amt-3-129-2010.html>.
- John M. Wallace and Peter V. Hobbs. *Atmospheric Science: An Introductory Survey*. Academic Press, 2006. ISBN 0080499538. URL <https://books.google.com/books?id=HZ2wNtDOU0oC&pgis=1>.

- F Wittrock and H Oetjen. MAX-DOAS measurements of atmospheric trace gases in Ny-Ålesund-Radiative transfer studies and their application. *Atmos. Chem. Phys.*, 4:955–966, 2004. URL <http://www.atmos-chem-phys.net/4/955/2004/acp-4-955-2004.pdf>.
- Folkard Wittrock. *The retrieval of oxygenated volatile organic compounds by remote sensing techniques*. Ph.d., University of Bremen, 2006.
- World Health Organization. Health aspects of air pollution with particulate matter, ozone and nitrogen dioxide: report on a WHO working group, Bonn, Germany 13-15 January 2003. 2003. URL <http://apps.who.int/iris/handle/10665/107478>.
- World Health Organization. Burden of disease from household air pollution for 2012. *WHO, Geneva*, 2014. URL http://www.who.int/phe/health_topics/outdoorair/databases/FINAL_HAP_AAP_BoD_24March2014.pdf.
- World Health Organization. Air pollution costs European economies US\$ 1.6 trillion a year in diseases and deaths, new WHO study says. apr 2015. URL [http://www.euro.who.int/en/media-centre/sections/press-releases/2015/04/air-pollution-costs-european-economies-us\\$-1.6-trillion-a-year-in-diseases-and-deaths,-new-who-study-says](http://www.euro.who.int/en/media-centre/sections/press-releases/2015/04/air-pollution-costs-european-economies-us$-1.6-trillion-a-year-in-diseases-and-deaths,-new-who-study-says).

Acknowledgements / Danksagung

An dieser Stelle möchte ich mich bei allen bedanken, die zum Gelingen dieser Arbeit beigetragen haben.

Bei Prof. John P. Burrows möchte ich mich dafür bedanken, dass er mir die Möglichkeit gegeben hat an seinem Institut diese Masterarbeit zu verfassen. Obwohl Sie ein sehr großes Institut leiten, haben Sie sich auch persönlich Zeit für mich genommen.

Mein Dank gilt auch Dr. Anette Ladstätter-Weißmayer dafür, dass sie sich trotz eines immer vollen Terminkalenders die Zeit genommen hat die Zweitkorrektur dieser Arbeit zu übernehmen.

Folkard Wittrock und Andreas Richter möchte ich besonders für die Betreuung meiner Arbeit danken. Ich habe im letzten Jahr in der DOAS-AG sehr viel gelernt.

Vielen herzlichen Dank an Enno Peters und Andre Seyler, die bei allen Fragen und Problemen meine erste Anlaufstelle waren und immer ein offenes Ohr und viele gute Ratschläge für mich hatten. Ihr wart mir eine große Hilfe und Unterstützung.

Many thanks to the whole DOAS-Group, for your support at the DOAS-meetings and the very warm atmosphere. I felt comfortable from the very beginning.

Zum Schluss möchte ich ganz besonders meinen Eltern danken, die mich während meiner gesamten Studienzzeit uneingeschränkt unterstützt haben, sowie vielen Dank an Martin, Jakob, Christian, Christina und Leonie.